Additive Manufacturing of Graphene-based Devices

by

Amir Azhari

A thesis
presented to the University of Waterloo
in fulfillment of the
thesis requirement for the degree of
Doctor of Philosophy
in
Mechanical and Mechatronics Engineering (Nanotechnology)

Waterloo, Ontario, Canada, 2017

Examining Committee Membership

The following served on the Examining Committee for this thesis. The decision of the Examining Committee is by majority vote.

External Examiner	NAME: Hani Naguib Title: Professor
Supervisor(s)	NAME: Ehsan Toyserkani Title: Professor
Internal Member	NAME: Adrian Gerlich Title: Associate Professor
Internal Member	NAME: Hamid Jahed Title: Professor
Internal-external Member	NAME: Frank Gu Title: Professor

Author's Declaration

This thesis consists of material all of which I authored or co-authored: see Statement of Contributions included in the thesis. This is a true copy of the thesis, including any required final revisions, as accepted by my examiners.

I understand that my thesis may be made electronically available to the public.

STATEMENT OF CONTRIBUTIONS

I would like to acknowledge the names of my co-authors who contributed to the research described in this dissertation, these include:

- Prof. Ehsan Toyserkani: supervision of the research, providing original idea for the current thesis, editing papers, providing lab facilities
- Prof. Michael Pope: brainstorming, providing lab facilities, analysis and substantiating the data
- Ehsan Marzbanrad: brainstorming, running the experiments, editing papers
- Dilara Yilman: running the experiments
- Farzad Liravi: running the experiments

Abstract

Additive manufacturing (AM) introduces a new era for the fabrication of 3D structures. AM, as an emerging and disruptive manufacturing technology, has the potential to be employed for fabrication of polymeric, metallic, and ceramic structures. Although AM is now being used for commercial applications, there are still many challenges in incorporating high-performance materials into these techniques and employing them to fabricate practical devices.

For instance, reduced graphene oxide (RGO) has interesting properties such as high specific surface area and lattice defects with tunable functional groups which make it ideal for different applications. However, there is still a substantial need to introduce reliable manufacturing techniques for RGO-based devices while attaining the utmost performance of graphene-based materials. In this study, a binder-jetting powder-bed AM technique has been employed to fabricate graphene-based structures and devices for energy storage and sensing applications.

First, 3D structures of graphene/hydroxyapatite (Hap) based composite with potential applications in bone-implantation were fabricated using AM technique. Hap suffers from lack of sufficient mechanical strength which has limited its application for practical use. The compressive strength of the 3D printed structures were tested and the printing parameters were optimized to improve the mechanical behavior of the specimens. It was shown that at a layer thickness of 125 μm and core binder saturation level of 400%, the mechanical strength of HG4 structures with only 0.4 wt.% of graphene oxide were 70 times more than that of HG0 structures.

Our next goal was to print pure graphene-based structures for energy and sensing applications. Hence, graphene oxide was first synthesized through Hummer's method and then reduced it through thermal and chemical methods to compare their performance for energy applications. The as-obtained thermally and chemically reduced graphene-oxide based powder were both 3D printed and studied accordingly. It was revealed that the gravimetric capacitance of thermally reduced graphene oxide (TRGO) 3D printed electrodes were 3-4 times higher than that of chemically reduced powder. Therefore, TRGO powder was selected for further studies and optimization. In order to improve the performance of 3D printed TRGO based electrodes, a nano palladium dispersion was synthesized and injected into the electrodes after printing. TRGO based decorated with nano palladium particles showed an impressive capacitance of 265 F/g and 700 mF/cm^2 at 5 mV/s. This study can introduce a new potential application of AM for the fabrication of graphene-based supercapacitor devices.

In addition, a graphene-based humidity sensing devices was also fabricated using powder-bed AM technique. The results obtained from this device were promising and demonstrated a great potential for the use of AM for manufacturing of graphene-based sensor devices.

Acknowledgements

Foremost, I would like to express my sincere gratitude to my advisor Prof. Ehsan Toyserkani for the continuous support of my Ph.D study and research, for his patience, motivation, enthusiasm, and immense knowledge. I would also like to thank Prof. Michael Pope who was a great support to fulfill my project. In addition, I would like to thank the rest of my thesis committee: Prof. Shahrzad Esmaeili, Prof. Adrian Gerlich, and Prof. Frank Gu, and Prof. Hamid Jahed for their encouragement, insightful comments, and hard questions. And I would like to thank my wife, Nazanin, for her understanding and love during the past few years. Her understanding, support, and encouragement made this dissertation possible.

Dedication

I am dedicating this thesis first to my father, RIP, whose spiritual support has always been with me. I am also dedicating this thesis to four beloved people who have meant and continue to mean so much to me. My mother, Tahereh, brother and sister, Bahman and Nooshin, and my lovely wife, Nazanin.

Table of Contents

List of Figures

List of Tables

Chapter 1

Introduction

1.1 Overview

Carbon has different allotropes like fullerene, carbon nanotube, and graphite with outstanding properties. Graphene sheets, as the main building block of graphite, are sp^2-bonded carbon atoms positioned in a honeycomb structure. Graphene has been studied theoretically since 1940s until it was physically discovered in 2004 [1]. There have been numerous studies on the applications of graphene due to its exceptional electronic, thermal, optical, and mechanical properties. Among these studies, many were directed toward development of graphene and graphene-based nanocomposites [2]–[20]. However, to the best knowledge of the author, so far there has been no report on porous graphene-based 3D structures fabricated using binder-jet powder-bed additive manufacturing technique.

Additive manufacturing is a novel process which can be employed for the fabrication of 3D complex porous structures. The aim of this research is to study a novel 3D fabrication technique for the synthesis of graphene-based complex shapes for actual device applications.

1.2 Motivation

There is a plethora of applications for graphene and graphene-based nanocomposite macro-3D structures in biological engineering (bioimplantation) [21], optics [22]–[27], water purification [8-9] , photocatalytic applications [6], supercapacitors [29], and batteries [12-13]. Graphene has been reported to improve the mechanical strength of polymeric, metallic, and ceramic nanocomposites [4], [7], [11], [18], [20], [32]–[41]. However, to the best knowledge of the author, in all the proposed fabrication techniques, there is no report on the powder-based additive manufacturing of graphene-based macro 3D structures.

Additive manufacturing (AM) is a novel and simple method for the fabrication of porous complex 3D structures. Among different known techniques for AM, powder-bed additive manufacturing, so called 3D printing, is a manufacturing technique which can be employed for the fabrication of metallic and ceramic porous structures. In principle, the powder with proper flowability is placed into the feed bed of the printer and the roller spreads the powder layers onto a build bed where an aqueous-based binder is injected on the top layer of build bed based on a sliced CAD model. This process is iterated until the 3D object is manufactured with pre-determined shape and possibly, porosity for desired applications. Incorporation of 3D printing for the fabrication of graphene and graphene-based nanocomposite structures can open a new horizon for the novel applications of graphene. Towards this goal, first, a graphene-based nanocomposite is developed for 3D printing to fulfill a comprehensive study on physical and mechanical properties of the 3D structure. Second, a more detailed study is conducted to 3D print graphene-based structures for full-size devices such as supercapacitors and sensors.

As the first step, graphene/hydroxyapatite (Hap) nanocomposite is chosen to be studied owing to its application as bone implants. Hap chemical composition is very similar to that of bone. Nevertheless, most Hap structures suffer from lack of sufficient mechanical strength to replace the bone parts. In addition, bone shape and structure differ from person to person which complicates the fabrication process of bone implants. Graphene is reported to improve the mechanical properties of Hap composites [15], [42]–[45]. However, development of an efficient fabrication technique for Hap/graphene bone implants with a interconnected pore structure for migration of cells is still challenging. In order to investigate the 3D printed structure of Hap/graphene composites, graphene oxide (GO) was first functionalized for better distribution inside the Hap matrix. Hap particles were added to the GO dispersion during vigorous stirring on a hot plate. The dispersion was dried to obtain the agglomerated powder. Thereafter, the powder was grinded and sieved respectively to be used for the AM process. Raman spectroscopy, XRD, and SEM analyses were employed to characterize the activated GO and also the nanocomposite. Two different compositions, 0.2 wt.% and 0.4 wt.% graphene to Hap, were synthesized and printed to be compared with Hap structure with no graphene content (HG0). Furthermore, the effect of layer thickness and binder concentration on the mechanical strength of the structures was also explored. Ultimately, the samples were sintered and toxicity of the green and sintered samples was measured.

Graphene-based supercapacitors have recently been widely studied due to their superior performance compared to other materials and allotropes of carbon. Supercapacitors outperform batteries in certain application areas such as such as memory backup systems, engine starters, and regenerative breaking in trains and electric cars where high power densities are required. However, the downside of supercapacitors is their lower energy density than batteries (10-20 Wh.kg-1 vs 150-300 Wh.kg-1) [46]–[48]. There are still ongoing investigations to improve the energy density of graphene-based supercapacitors and broaden their use in different applications. In supercapacitors, electrical double layer is formed on the surface of the electrodes which contribute to the energy storage in the device. Therefore, one of the main goals in this research area is to develop electrodes with a high surface area which can potentially increase the formation of electrical double layer capacitance in the electrodes [49], [50]. Activated carbons (ACs) and carbon nanotubes (CNTs) have a high specific surface area with micropores. However, these pores are very small and mostly inaccessible for the electrolyte ions which limits their capacitance to less than 20% of the expected values [29], [51], [52]. Nevertheless, graphene based materials with a high specific surface area up to 2675 m^2/g show promising performance at high densities of electric current [53], and more importantly, a high theoretical specific capacitance of 450 F/g, due to residual functional groups and lattice defects, are known as excellent candidates for energy storage applications [48].

Fabrication of thick porous graphene-based electrodes with maximized double-layer capacitance (C_{DL}) is still under investigation. In-situ self-assembly [54], chemical vapor deposition [55], and hydrothermal methods [56] are common methods for the fabrication graphene-based electrodes. Mechanical compaction of graphene-based powder is also proposed for manufacturing of thick electrodes which requires binder, mostly PTFE, and additives for consistent results [57]. Also, mechanical compaction reduces the accessible pore volume for the electrolyte ions. Meanwhile, we believe that powder-bed additive manufacturing technique can open a new horizon towards fabrication of thick graphene-based electrodes.

In this research, a novel approach for the manufacturing of pure graphene electrodes using a binder-jet powder-bed additive manufacturing (AM) technique is introduced [58].

Three-dimensional structures can be fabricated in a layer by layer fashion using AM, particularly when a complex shape is to be made in a short period of time. In addition, as reported elsewhere [59]–[62], 3D structures manufactured by powder-bed AM technique may have a porosity in the range of 35-50% which can provide a significant effective surface area as the interface between the electrolyte and the electrode for the formation of EDL. To study this hypothesis, chemically reduced graphene oxide (CRGO) was synthesized and employed as the electrode materials. In order to avoid the restacking of CRGO sheets after reduction, PVA was added at different concentrations to the GO dispersion before addition of HI acid. The samples were drop-cast and tested for their capacitance in a supercapacitor cell. The sample with the higher capacitance and better performance was chosen to be used for AM. Additionally, GO was reduced through thermal exfoliation and used it for 3D-printing of supercapacitor electrodes. We finally compared the effect of the reduction process on the performance of supercapacitor electrodes fabricated through the powder-based AM technique.

After comparing CRGO and TRGO, TRGO powder was selected for further study and optimization. In order to improve the performance of TRGO 3D-printed disks, different concentration of nano palladium dispersion (up to 9wt.% of graphene) were added to the disks. It was shown that the impregnation of disks with nano palladium will increase the capacitance of the TRGO disks, particularly at higher scan rates. The SEM images revealed that the graphene layers were well-decorated with nano palladium particles which should have eventually reduced the contact resistance between the graphene sheets. The results verified the potential application of AM technique for fabrication of thick graphene-based electrodes to be used in actual supercapacitor device.

Graphene-based materials have also recently addressed as promising candidates for sensing different chemicals and gases including humidity [63]–[66]. However, these studies are still at early stages and need further investigation to confirm their performance as an actual device. These reports were mainly on the study of graphene-based thin films which can limit their application as an actual device. Considering the capabilities of AM, we also used the binder-jet powder-bed AM technique for the fabrication of a graphene-based humidity sensor device. In addition, a nozzle dispensing additive manufacturing machine was incorporated to fabricate a housing from polysiloxane for the graphene-based 3D structure. The 3D-printed graphene-based 3D-structure displayed a high specific area which can optimize the gas sensing properties of the device and verify AM as a unique tool for the fabrication of full size sensor devices.

In summary, binder-jet powder-bed additive manufacturing technique is introduced as a facile technique for additive manufacturing of thick 3D structure of advanced materials, in particular graphene for practical applications including in composite structures, supercapacitor electrodes, and sensing electrodes. This research provides a comprehensive study for simple and timely-efficient fabrication of thick and porous graphene-based 3D structures with high effective surface area with enhanced performance in energy and sensing application areas. There are numerous researches on fabrication of thick graphene-based 3D structures [49], [132], [180], [210]–[214], mostly through hydrothermal and self-assembly methods. However, these processes are commonly complicated and time-consuming and require use of toxic reagents with vacuum or freeze drying [215]–[218] which may lead to cracking [207]. In addition, the structures obtained through these chemical methods suffer from low dimensional accuracy. In the current proposed powder-bed additive manufacturing, the as-received TRGO powder can be simply dispersed in an alcohol or acetone and then dried and used for additive manufacturing. Through this study, the manufacturing parameters required for successful fabrication of the graphene-based 3D structures are defined and shown in detail. By using the identified parameters, the fabrication process can be completed in a few minutes and the structures can be directly used in a device for further characterization and final use. Contrary to other additive manufacturing techniques such as inkjet printing or fused deposition modeling (please see chapter 2 for more details) , binder-jet powder-bed additive manufacturing method does not require any specific material treatment or development for the fabrication process. After studying and identifying the required manufacturing parameters, thick porous graphene-based 3D structures were fabricated and used in different devices to investigate their performance in multiple application areas. In the first study, graphene oxide powder was added to hydroxyapatite and the 3D structures of the as-obtained composite was fabricated by powder-bed additive manufacturing technique. The mechanical properties of the AM-made structures are studied and reported in chapter three. In the following chapters, reduced oxide graphene based 3D structures were printed and used as thick electrodes for supercapacitors and humidity sensing. The flowchart of this research is shown in Figure 1.1.

1.3 Thesis objectives

The objective statement of the current proposal is: “Additive Manufacturing of Graphene-based Devices”. To this end, the following objectives are pursued:

- Synthesis and development of graphene-based nanocomposites
- Fabrication of graphene-based 3D structures for actual devices using binder-jet powder-bed AM technique
- Synthesis and characterization of Hap/ graphene-based materials
- Characterization of the printed structures for practical applications such as supercapacitors and sensors

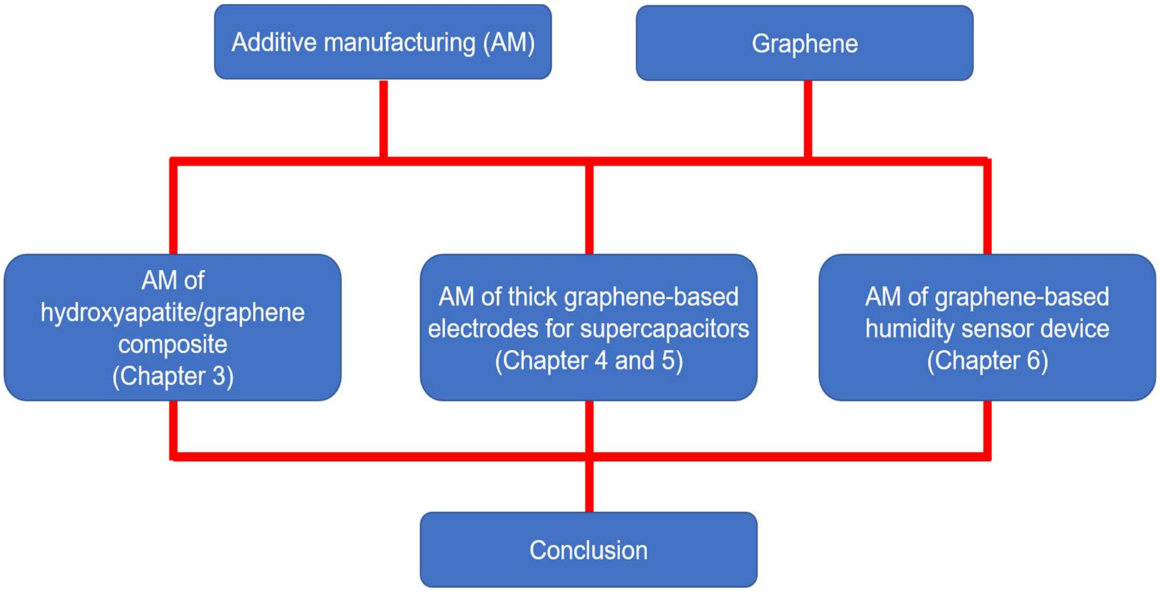

Figure 1.1. Flowchart of the research conducted in the current thesis.

1.4 Thesis Outline

The current dissertation includes seven chapters where the importance of the research, the details of the experiments, and the obtained results are discussed accordingly.

Chapter two outlines a thorough introduction to additive manufacturing techniques with the emphasis on powder-bed 3D prinitng and its requirements. Also, the properties of graphene-based materials and their application in different areas are discussed. Chapter three outlines the synthesis and characterization of 3D-printed Hap/graphene-based composites. In Chapter four, graphene-based electrodes obtained through two different reduction mechanisms were characterized and used in AM for the fabrication of thick electrodes. Their capacitance performances were compared and optimized for practical applications. Chapter five explains the further investigations carried out towards improving the performance of 3D-printed TRGO-based electrodes by decorating graphene sheets with nano palladium particles. Chapter six is focused on the fabrication of a graphene-based sensor device for humidity sensing applications. In chapter seven, the conclusion and the recommendation for future work are outlined.

- The third chapter is a journal article published in the International Journal of Applied Ceramic Technology:

❖ **Amir Azhari, Ehsan Toyserkani, Carole Villain, "Additive Manufacturing of Graphene–Hydroxyapatite Nanocomposite Structures", International Journal of Applied Ceramic Technology, Volume 12, Issue 1, 2015, Pages 8-17**

- The fourth chapter consists of a manuscript to be submitted to the Journal of Nanotechnology:

- **A. Azhari, D. Yilman, E. Marzbanrad, M. Pope, E. Toyserkani, “The impact of reduction method on the supercapacitor performance of additive manufactured graphene electrodes”, Nanotechnology, October 2016 (to be submitted)**

- The fifth chapter consists of a manuscript which is submitted to Carbon:

- **A. Azhari, E. Marzbanrad, D. Yilman, M. Pope, E. Toyserkani, “Binder-jet powder-based additive manufacturing (3D printing) of thick graphene-based electrodes”, Carbon, CARBON-D-16-04028**

Chapter 2

Background and literature review

2.1 Introduction

In this chapter, first, additive manufacturing and its classifications are discussed. Since 3D printing is the adopted approach for this study, more details on 3D printing including applied raw materials are also given. Next, the importance of graphene and the synthesis methods are reviewed. Also, the fundamentals of supercapacitors and application of graphene-based electrodes in this area is discussed accordingly. Finally, a brief description of obstacles to additive manufacturing of graphene and the proposed solutions are explained in detail.

2.2 Additive manufacturing

2.2.1 Classifications of additive manufacturing

Additive manufacturing (AM) techniques are based on layer-by-layer manufacturing of objects. They enable manufacturing of complex shapes with different materials. Basically, a virtual model is designed through a Computer-Aided Design (CAD), converted to STL (stereolithography) format, and uploaded to the machine to build the physical object. AM provides a variety of techniques for the fabrication of different materials with disparate shapes and level of porosity. A committee (F42) was founded by American Society for Testing and Materials (ASTM) in 2009 to define international standards for the whole process. According to F42, AM includes all the approaches towards layer-by-layer manufacturing of an object from polymers, ceramics, and metals [67]–[70].

So far, thirty different additive manufacturing methods have been introduced or commercialized. F42 has classified them into seven main categories based on the process including [67]–[70];

- Material extrusion
- Material jetting
- Binder jetting
- Sheet lamination
- Vat photopolymerization
- Powder bed fusion
- Directed energy deposition

Several techniques for each one of the above classifications have been introduced so far. However, most of them have not been commercialized and numerous modifications must be implemented to adopt them to industrial applications. In the next section, the most common additive manufacturing techniques currently used in research and industry will be discussed.

2.2.2 AM techniques

There are five particular techniques which are used conventionally in industry. A brief explanation of each technique is given in the following. It is noteworthy that there could be other classifications for AM techniques according to the process technologies or type of raw materials. However, herein, the most common techniques with an emphasis on the adopted technique for the current research will be introduced.

2.2.2.1 Stereolithography (SLA)

Invented by Chuck Hull in 1987, SLA has been one of the most commonly used techniques in additive manufacturing. There is a variety of photopolymeric resins which harden when exposed to ultraviolet laser. Based on the CAD model, the laser probes the resin to make consecutive layers of the object by photopolymerization. According to ASTM, this layer-by-layer manufacturing process is categorized into Vat photopolymerization [67]–[70].

2.2.2.2 Fused Deposition Modelling (FDM)

Stratasys founder Scott Crump patented this technique in 1992. Many different thermoplastic polymers can be used in FDM to build any complex object. The polymer is softened in a heating chamber forming a filament. ABS, and particularly ABSplus, is the most common polymer used in FDM machines. The filament along with a support material is deposited layer by layer through an extrusion pressure. ASTM classifies FDM into Material extrusion process [67]–[70].

2.2.2.3 Selective Laser Sintering (SLS)

SLS is a powder-based technique. A roller pushes the powder forward from the feeding bed to the building bed in a preheated chamber. A laser beam scans the powder on the building bed according to the CAD model. The particles sinter and fuse into each other to make the first layer of the object. The process is iterated layer by layer until the object is completed. ASTM has considered this process into Powder bed fusion category [67]–[70].

2.2.2.4 Multi Jet Modelling (MJM)

Introduced by 3D systems and Object Geometries, Polyjet or Projet technique employ a print head with hundreds of individual nozzles to deposit a photopolymeric material and a gel-like material (as a support). Immediately after the deposition of the first layer, an ultraviolet light is emitted to polymerize the materials. The building platform is lowered afterwards and then the next layer of the materials is deposited while cured by the incidence of the ultraviolet light. The process lies in the category of Material jetting.

2.2.2.5 Binder jetting (powder-bed 3DP)

Developed in MIT in 1993, binder-jetting powder-bed additive manufacturing technique is among the most common AM processes due to a lower cost of operation and a simple operation. Conventionally, there are two beds, feeding and manufacturing bed, filled by the powder. The feeding bed moves upward with an accuracy of less than 100μm. A rotating roller spreads a smooth layer of powder from the feeding bed onto the building bed. Next, a print head injects a binder to the powder bed according to CAD model to form the object. The binder penetrates between the particles and reacts with the powder. The first layer of the object is formed through the adherence of particles. Subsequently, the feeding bed is moved upward based on the pre-determined layer thickness. Having been placed in the initial position, the roller advances again to spread the next layer of the powder onto the building bed. The print head injects the binder on the second layer. The process is iterated until the object is built. Finally, the green part is removed from the bed and the excessive powder is removed cautiously. Figure 2.1 illustrates the different parts of the process schematically. Highly porous structures (more than at least 50%) can be fabricated via this technique. By manipulating the particle size distribution and also using several feeding beds at the same time, a functionally graded porous structure can be built with numerous applications. Mostly, the green ceramic or metallic structures need post heat-treatment (sintering) to increase the mechanical strength due to high initial percentage of porosity. This technique is classified into Binder jetting process according to ASTM.

The powder-bed 3D printing technique is the adopted approach for the current study. Almost all the materials existing in the form of flowable powder can be shaped by this technique.

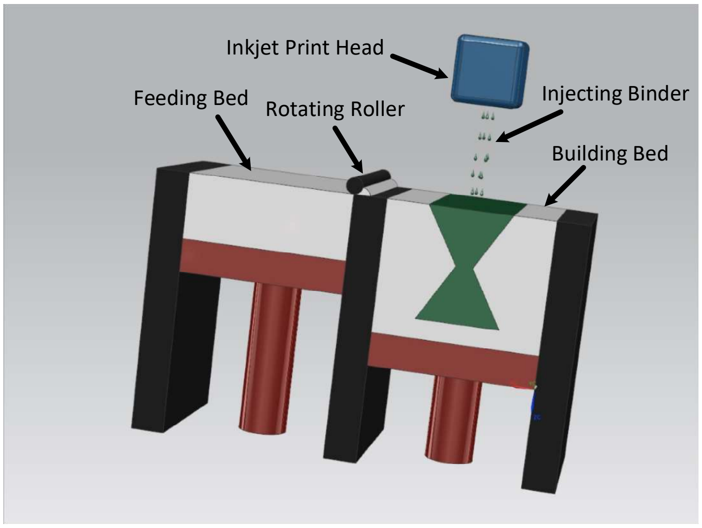

Figure 2.1. Schematic of three-dimensional printing technique.

This is an outstanding property which is not provided by other techniques. Since there is a unique geometrical flexibility in the synthesized structures, powder-bed 3D printing is also known as solid free-form fabrication (SFF) technique. The size of the porosities (in the range of 50-1000 μm) could also be controlled by this technique. All these features perfectly match the requirements for scaffold engineering. However, the resolution and accuracy of 3D printed structures are still challenging. There are several parameters like layer thickness, print head resolution, binder saturation level, type of injecting binder, the interaction between powder and injected binder, physical and chemical properties of the dry binder mixed with the powder, particle size distribution, trapped powder in conformal channels with less than 1 mm size, and the properties of the powder which can be set properly to achieve the desired structures. In the following, the essential demands of AM will be discussed accordingly.

2.2.3 Requirements of binder-jetting AM

The basic requirements for binder-jetting AM must be well-recognized to make sure that the intended object can be constructed properly through this method. The main concept of binder-jetting AM relies on spreading iterative layers of powder on the building bed. One of the most important prerequisites for binder-jetting AM is the appropriate flowability of the powder. Bulk density, particle density, surface structure, particle size, particle shape, and moisture content all have crucial effects on the flowability of the powder [71]. It has been reported that flowability and spreadability of the powder layer on the building bed can be improved by adjusting the speed and the spinning motion of roller [72].

Lowering the layer thickness improves the resolution of the parts. In particular, the layer thickness needs to be larger than the maximum particle size of the powder. Smaller particle size is also desirable for higher resolution of the parts. Nevertheless, there must be balance between the resolution and flowability of the powder [73].

The aqueous binder should present a proper interaction with the particles when injected on the powder layer. The injected binder should be able to wet the particles properly in order to provide a suitable green mechanical strength. Wettability depends on different factors such as the contact angle between the binder and the particles, shape and size of the particles, the chemical reactions, surface chemistry and the surface tension of the particles and also the binder viscosity. The interaction between the aqueous binder and the particles, for instance, determines the spreadability of binder in the powder. Higher reactivity hinders the essential spreadability of the binder in order to wet all the particles. On the contrary, excessive wetting of the particles by the binder due to lower reactivity ends up with the penetration of the binder to the outer shell of the part and lowering accuracy and resolution [74].

It is noteworthy that different reaction mechanisms might occur between the binder and the particles based on the binder type and the particle. Disparate types of binder including water, chloroform, oxalic and tartaric acid, phosphoric acid, citric acid, disodium succinate, and sodium chondroitin sulphate have been used for AM according to the powder properties. The binder (commonly acidic binder), for example, can dissolve the particles, so recrystallization will be responsible for bonding between the particles.

Polymeric binders harden the powder through formation of Van der Waals or hydrogen bonding. As discussed earlier, AM is designed to build objects from powder. Thus, almost all the materials including metals, ceramics, and polymers in powder form can be printed through this method. Natural polymers react with water whereas synthetic polymers need organic solvents. Both polymeric and acidic binders, for example, can be used for ceramic powders. Consequently, a good understanding of the material properties is highly needed to select the appropriate binder for AM [74].

To sum up, AM is a unique technique for the synthesis of complex and porous structures. The size and the pattern of the pores can be almost controlled. Also, this technique provides an excellent flexibility in terms of applicable materials. Almost all the materials in a powder shape with a proper flowability can be printed through this technique.

2.3 Graphene

Graphene is the building block of most of the allotropes of carbon. It can be wrapped into a shape of a ball to make the 0-dimensional buckyball (fullerene). It can be rolled to form the 1-dimensional nanotube. It can also be stacked to make the 3-dimensional graphite. Graphene is a single sheet of sp^2-bonded carbon atoms in a honeycomb structure. One single graphene sheet is called a monolayer or single layer graphene with the thickness of about ~ 0.3 nm [1], [53], [75]. Obviously, two or three layer graphene layers are well known as bilayer or trilayer graphene. 5-10 and 20-30 layer graphene sheets are called few-layer and multilayer graphene, respectively. There have been many theoretical studies on graphene since more than 60 years ago. Graphene was consistently considered as an unstable material until the first discovery of a single layer of graphene in 2004. Andre Geim and Kostya Novoselov deployed mechanical exfoliation of graphite to synthesize graphene [1], [53], [75], [12], [76]–[79]. Since then, there have been many studies on different synthesis techniques and properties of graphene.

2.3.1 Synthesis and characterization of graphene

So far, numerous techniques have been proposed to synthesize graphene. Mechanical exfoliation, chemical exfoliation, chemical synthesis, precursor-based synthesis, chemical vapor deposition, and epitaxial growth are the most well-known methods for the synthesis of graphene. In the following, the most common techniques i.e. mechanical and chemical exfoliation will be discussed briefly.

Mechanical exfoliation was the first known method employed to obtain few-layer down to monolayer graphene in 1999 using Atomic Force Microscopy (AFM) tips. AFM technique is commonly capable of producing few-layer graphene with the thickness of ~ 10nm. However, synthesis of a monolayer graphene was first reported in 2004 using adhesive tape [12], [78], [79]. Geim and Novoselov used a 1 mm thick layer of highly oriented pyrolytic graphite (HOPG) firmly pressed onto the scotch tape. Afterward, they gently folded and unfolded the tape several times until an optically transparent layer is left on one side of the tape. The tape was then washed in acetone. A Si wafer was dipped in the dispersion to collect the flakes. A plethora of water and propanol was used to wash the wafer in a sonicator. Ultimately, few-layer graphene flakes with the thickness of even less than ~ 3 nm and the lateral size of 10-20 μm was obtained [12], [78], [79]. Although the above techniques are known as a facile route to produce graphene, the yield is very low. Other techniques like ball milling and liquid phase sonication can produce graphene at larger scales, however, controlling the thickness and the defects of the as-received graphene are still challenging.

Chemical exfoliation is based on the graphene layers in crystalline graphite using chemical solvents. After separation, it is also required to prevent them from restacking. Alkali metals are the most suitable intercalating compounds since their ionic radii are smaller than the interlayer spacing of graphite. K, Cs, and NaK_2 alloy have shown promising results in exfoliating graphite. Nevertheless, single layer and bilayer graphene sheets cannot easily be produced. Using polar solvents like N-methyl-2-pyrrolidone (NMP) along with sonication is reported to be highly effective in synthesizing pristine single layer graphene. Several other chemical solvents such as dimethylformamide (DMF), 1,2-dichloroethane (DCE) and poly(m-phyenylenevinylene-co-2,5-dioctoxy-pphenylenvinylene (PmPV), N-Dimethylacetamide (DMA), g-butyrolactone (GBL), tetrabutylammonium hydroxide (TBA), and 1,3-dimethyl-2-imidazolidinone (DMEU) were investigated for chemical exfoliation of graphite [12], [76]–[79]. A large scale of micron sized graphene can be synthesized by chemical exfoliation.

Reducing graphene oxide is another common technique for the synthesis of graphene. Graphene oxide is a name given to any graphene sheet containing different types of oxygen functionalities like hydroxyl, carboxyl, phenol, epoxide, and ketone groups. Graphene oxide is used very commonly as a starting material to produce graphene. In order to achieve graphene oxide, first, graphite must be oxidized. There have been many studies since 1860 on the oxidization of graphite. However, the method proposed by Hummers and Offeman is the most well-known method commonly used for the oxidization of graphite. An appropriate proportion of sodium nitrate, graphite, sulphuric acid, potassium permanganate, water, and hydrogen peroxide were mixed at different stages and different temperatures to obtain graphite oxide powder. A mild mechanical force like sonicating or prolonged stirring is needed to exfoliate graphite oxide into separate graphene oxide sheets. Thanks to the functional groups, graphene oxide is hydrophilic and can be dispersed easily in water [12], [76]–[79].

Reduction of graphene oxide to graphene can be achieved through chemical, heat treatment, and electrochemical approaches. Agglomeration of graphene sheets after reduction in water is one of the main concerns while applying the chemical route. Sodium borohydride (NaBH4), hydrazine, 1,1-dimethylhydrazine, hydroquinone, and dimethylhydrazine as reducing agents can almost prevent the intense agglomeration of graphene sheets. Among them, hydrazine is widely used in a method known as Modified Hummers method to reduce graphene oxide [12], [76]–[79]. Graphene oxide can also be converted to graphene via heat treatment at different temperatures. The decomposition of functional groups generates a significant amount of pressure that breaks the van der Waals forces between the graphene oxide sheets. Hence, a reduced few-layer graphene could be obtained accordingly.

Characterization methods of graphene are generally classified into microscopy and spectroscopy techniques. Microscopy techniques help to explore the crystal lattice, morphology, and atomic structure of graphene. Optical Microscopy (OM), AFM, Scanning

Tunneling Microscopy (STM), Scanning Electron Microscopy (SEM), and Transmission Electron Microscopy (TEM) are the most common microscopy techniques used for the characterization of graphene. Spectroscopy techniques investigate the energy distribution in the atomic scale and the interaction of phonons with different sources of energy like laser and X-ray. Raman Spectroscopy, Auger Spectroscopy, X-Ray Photoemission Spectroscopy (XPS), and X-Ray Diffraction (XRD) are frequently deployed to characterize graphene.

2.3.2 Graphene properties

As discussed earlier, graphene has excellent mechanical, electrical, thermal, and optical properties. Some of the main properties of graphene are listed in Table 2.1. These remarkable properties have opened a new horizon in the synthesis of countless graphene-based composites to be used in many different applications. Addition of graphene to polymer, metal, and ceramic matrices is shown to have significant effect in improving the mechanical, chemical, electrical, and thermal properties.

2.3.3 Graphene-based nanocomposites

So far, there have been numerous studies on polymer/graphene nanocomposites. The reported studies on epoxies [34], [35], Polyethylene [80], PMMA [81], Polypyrrole [82], [83], PVA [84], [85], elastomers [33], and polyimide [86] composites with different contents of graphene, to name a few, have all shown considerable improvements in the mechanical, electrical, and chemical properties. In contrast to polymer-based composites,

Table 2.1. Main properties of graphene [87]

Property	Unit	Graphene
Electron mobility	$cm^2V^{-1}s^{-1}$	15000
Resistivity	$\Omega - cm$	10^{-6}
Thermal conductivity	$Wm^{-1}K^{-1}$	$4.84\text{-}5.3 \times 10^3$
Coefficient of Thermal Expansion	$mm^{-1}K^{-1}$	-6×10^{-6}
Elastic modulus	TPa	0.5-1
Tensile strength	GPa	130
Transmittance	%	>95 for 2 nm thick film >70 for 10 nm thick film

ceramic and metal-based composites can be used for applications requiring high strength or high temperature resistivity. SnO_2 [19], [88], TiO_2 [2], [39], [89], MnO_2 [14], [90], ZnO [91], and Fe_2O_3 [92] are some of the ceramic materials used in the graphene-based composites. Mostly, graphene oxide is used as the starting material while the other ceramic components are formed in-situ from metallic salts during the mixing process.

Graphene oxide is easily dispersed in water so it can be mixed properly with oxide particles. There are other proposed methods for the fabrication such as mechanical mixing and CVD [87]. Similar methods have also been employed for the synthesis metal-based composites of graphene. It has mainly been targeted so far to use the ceramic-based composites of graphene as supercapacitors, field emitters, and photocatalyst. Bio-applications of graphene composites with calcium phosphate materials like hydroxyapatite [15], [42], [44], [45], [93], [94] and chitosan [7], [9], [41], [43], [95]–[98] have also been investigated thoroughly. There have been some studies on 3D printing of hydroxyapatite (Hap) [13],

[99]–[102]. Owing to similar chemical analysis to bone, Hap has been recommended as bone implantation [103], [104]. Hence, it has been selected as the main component of the composite. The synthesis process, characterization of the composite, 3D printing process, and the physical and mechanical properties of the printed samples will be elaborated in the later sections of the current report.

2.3.4 Graphene-based materials for energy applications

Electrochemical supercapacitors offer high power densities superior to that of batteries and can be used an engine starters in electric vehicles, memory backups, and portable electronics. In a typical capacitor, two conducting electrodes are separated by a permeable insulating layer immersed in a conducting electrolyte. Once the potential is applied, an electric field is formed and the charge is stored on the electrodes. Cyclic Voltammetry (CV), Electrochemical Impedance Spectroscopy (EIS), and charge/discharge cyclic test are the major characterization techniques for the electrochemical behavior of a supercapacitor. Electric double layer (EDL) capacitance and pseudocapacitance are the two major mechanisms for energy storage in the supercapacitors [29], [105]. Conducting polymers and metal oxides are the main electrode components in the case of pseudocapacitance while EDL capacitance is based on carbonaceous materials. Although high capacitance and energy density values are reported for pseudocapacitors, they show instability at high charge/discharge cycles with slow response time due to faradic reactions. On the other hand, notwithstanding the limited capacitance, EDL capacitors (EDLCs) have good stability at high lifecycles [105]–[107]. It commonly takes few seconds for EDLCs to charge/discharge at low frequencies. However, at higher frequencies, their behavior is similar to resistors; because the electrode in EDLCs is commonly made of porous carbonaceous materials (to increase the double layer capacitance) with high contact resistance. Pores and also contact resistance both contribute to resistor behavior of EDLCs at high frequencies. It is important to extend the range of operating frequency of EDLCs which results in fast charge/discharge rate [108].

In EDLCs, electrostatic charge is stored at the interface of electrode and the electrolyte and therefore, the electrode material should have a high specific surface area to accommodate abundant amount of charge. The idea of EDL which was first raised in the 19th century describes of two layers with opposite charges are accumulated at the interface of electrode/electrolyte (Figure 2.2a). This so-called Helmholtz layer model was later revised by Gouy and Chapman in which they considered a distribution of both anion and cation ions in a region near the interface called diffuse layer (Figure 2.2b). The capacitance values obtained using Gouy-Chapman model were overestimated and hence, Stern developed another model by merging previous two models and considering two layers called compact (Stern) layer and diffuse layer. In the compact layer, he described two regions, inner Helmholtz plane (IHP) and outer Helmholtz plane (OHP) where adsorbed and non-specifically adsorbed ions exist, respectively. The diffuse layer was very similar to that of Gouy-Chapman model. The capacitance of the compact layer (C_H) and the diffuse layer (C_{diff}) both contribute to the double layer capacitance (C_{dl}) by

$$\frac{1}{C_{dl}} = \frac{1}{C_H} + \frac{1}{C_{diff}}$$

The capacitance in EDLCs is generally calculated according to

$$C = \frac{\varepsilon_r \, \varepsilon_0}{d} A$$

where ε_r and ε_0 are the electrolyte dielectric constant and permittivity of a vacuum, respectively and A and d are the effective surface area of the electrode accessible to the electrolyte and the distance between two electrodes, respectively. Supercapacitor cells are commonly considered as equivalent RC circuits as seen in Figure 2.3. Due to series nature of the cell, the total capacitance of the cell is obtained through $\frac{1}{C_T} = \frac{1}{C_a} + \frac{1}{C_c}$ where C_a and C_c designate the capacitance of anode and cathode, respectively [46], [105], [107], [109], [110].

Obviously, the performance of EDLCs is very much dependent on the properties of the material used for the electrode. As reported previously [110], an ideal electrode material should have high specific area, high electrical conductivity even in a porous structure, and more importantly, high accessible surface area to the electrolyte ions. Carbonaceous materials such as activated carbons (ACs) and carbon nano tubes (CNTs) are widely used in EDLCs due to several factors including their high specific surface area.

However, the existence of micropores in their microstructure limits the effective surface area which lowers their capacitance. Surface functionalization is also known as an effective technique to improve the electrochemical performance of carbonaceous materials. It is generally accepted that functional groups facilitate adsorption of electrolyte ions and increase the wettability of the surface of electrode material. Additionally, the functional groups may promote faradaic redox reactions which can increase capacitance by 5-10% [110].

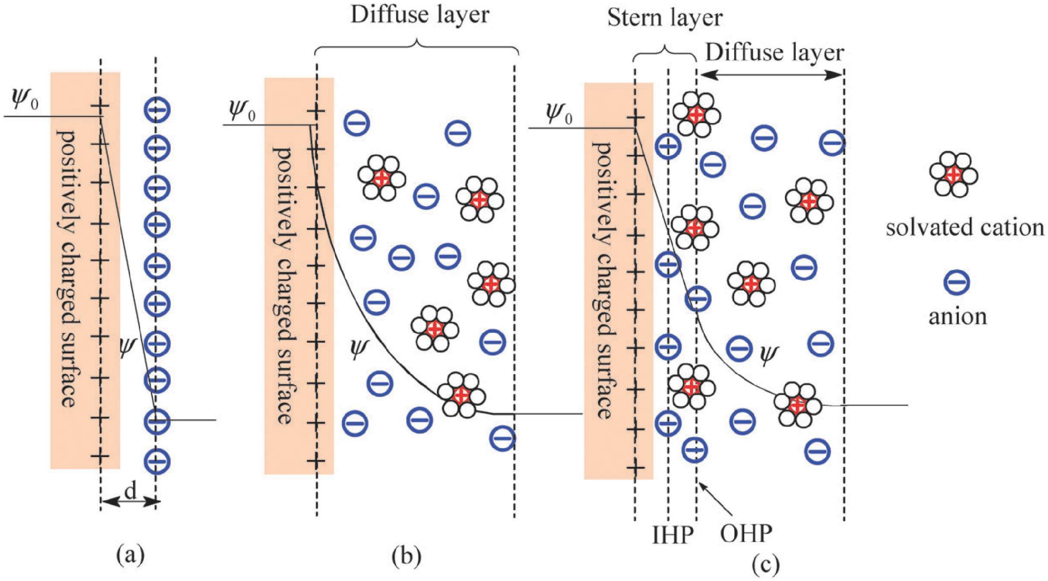

Figure 2.2. Schematic illustration of a) Helmholtz model, b) Gouy-Chapman model, and c) Stern model. The inner Helmholtz plane (IHP) and the outer Helmholtz plane (OHP) specify the region of adsorbed anions and non-specifically adsorbed ions next to electrode interface, respectively. Diffuse layer starts at the OHP. Potentials at the electrode surface and the interface are represented by Ψ0 and Ψ, respectively. This Figure is reproduced with permission –See Letters of Copyright Permission (Courtesy of Journal of Materials Chemistry) [106].

Notwithstanding promising results, one of the challenges with carbonaceous electrodes is high contact resistance between carbon particles/agglomerates/sheets which adversely affects the total performance of the supercapacitor.

With the emergence of graphene in the last decade, the performance of EDL capacitors has improved significantly when using graphene-based electrodes beyond activated carbon (AC) and carbon nano tubes (CNTs). Graphene has remarkable properties that make it an excellent candidate for energy storage applications, particularly in EDL capacitors.

However, recent studies have shown that pristine graphene has a low double layer capacitance (C_{DL}) due to its low quantum capacitance (C_Q).

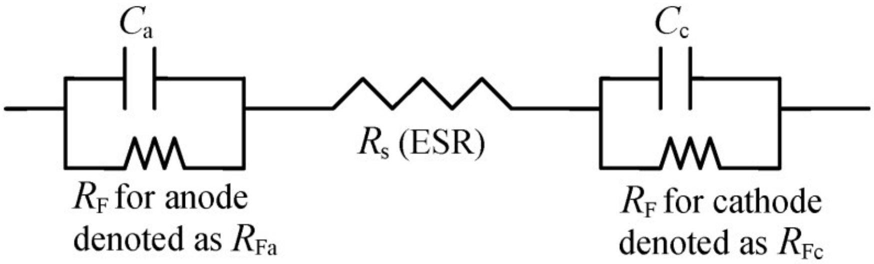

Figure 2.3. Schematic illustration of simple RC equivalent circuit representing a supercapacitor cell. RF and RS denote internal resistance of one electrode and equivalent series resistance (ESR) of the cell [106].

Quantum capacitance represents the electronic contribution of graphene. C_{DL} of graphene is calculated through

$$\frac{1}{C_{DL}} = \frac{1}{C_H} + \frac{1}{C_Q}$$

where CH describes the capacitance created by Helmholtz layer. Since, for pristine graphene, CQ is 3-4 μF cm-2 whereas CH ranges between 16 to 25 μF cm-2, CDL is governed by CQ. CDL of pristine graphene will be less when used in the porous electrode and exposed to the electrolyte and EDL on both sides of the sheet since it has to share the available density of states (DOS, N0) between each interface with the electrolyte as CQ = $\varepsilon\varepsilon_0 \sqrt{N_0}$. In this case, CQ and subsequently CDL will be divided by $\sqrt{2}$. It has been shown that the presence of dangling bonds and functional groups enhances CQ significantly by increasing DOS [48], [111]–[114].

In addition to functional groups, development of porous graphene materials/structures can help increase the effective surface area of the electrodes and enhance of EDL capacitance. There have been two approaches to increase the effective surface area. In one approach, the focus is on developing porous graphene materials used in the electrode. There are three classifications for porous graphene materials as microporous (pore diameter < 2 nm), mesoporous (2 nm< pore dimeter < 50 nm), and macroporous (pore diameter > 50 nm) as characterized in graphene nano mesh (GNM), crumpled graphene, and graphene foam, respectively.

GNM can be produced using polymeric building blocks and lithography techniques through which the pore structure and chemical nature of graphene sheet can be controlled [115]. However, it involves use of toxic materials for etching and is complicated and expensive for large scale production. UV-assisted photodegradation of graphene oxide [116], electron-beam irradiation [117], and template methods using CVD are the other techniques proposed for the fabrication of GNM. The GNMs developed by CVD have mostly shown very promising as energy storage materials in supercapacitor cells as reported in different reports [118]–[120]. Chemical activation methods are also employed for the preparation of GNM. Microwave exfoliation of graphite oxide [121] and hydrothermal polymerization of GO and precursors [122] activated by KOH, HNO_3 oxidation of GO [123], [124], and also catalytic oxidation have been studied extensively to synthesize GNM [125]–[128].

One of the common approaches to avoid agglomeration of graphene sheets and maintain the primary surface area is to prepare crumpled graphene (CG) (Figure 2.4) which can be used in most fabrication processes including molding and pelleting with minimum loss of surface area [49]. It has been suggested that thermal exfoliation of GO can yield crumpled graphene sheets, particularly when the decomposition rate of functional groups is higher than the diffusion rate of vaporized gases, leading to elevated internal pressure which can overcome the van der Waals forces between graphene layers [129]. It was also shown that immediate cooling of thermally exfoliated reduced graphene oxide in liquid nitrogen can yield highly crumpled graphene sheets with exceptional performance in supercapacitors. The use of aerosol based processes such as aerosol spray pyrolysis of GO suspension have also been reported as promising techniques for the fabrication of crumpled graphene sheets [49]. However, the due to high surface area, the gravimetric capacitance values obtained from CG is high; however, the volumetric capacitance is low due to a significant pore volume. Therefore, when using CG, it is important that the pore volume of the electrodes be minimized to enhance the volumetric capacitance of the electrodes.

Graphene foams (GF) have also exhibited interesting properties with potential applications in different areas such as environmental clean-up and electronic devices. GFs with interconnected pore structure facilitate ion/electron transport in the supercapacitor and are commonly manufactured through self-assembly and CVD. Self-assembly of flexible GO sheets via a hydrothermal method at 180 °C for 12 h with subsequent reduction using hydrazine vapor yielded GF with specific capacitance of 220 F g^{-1} [130]. Hydrothermal method has turned into a common practice for fabrication of macroporous graphene-based 3D structures. It has also been suggested to use ammonia during hydrothermal reduction of GO suspension can produce GF with proper mechanical strength [131]. Doping graphene sheets with nitrogen using different chemicals such as ammonia boron trifluoride (NH_3BF_3) and ammonia during hydrothermal reactions can also enhance the electrochemical performance [132]. Use of ammonia boron trifluoride added to GO suspension has been reported to yield boron co-doped graphene aerogels (BN-GAs) with interconnected macroporous structure through hydrothermal and freeze-drying process. The foam used as an electrode indicated a gravimetric capacitance of 62 F g^{-1} [56]. Figure 2.5 illustrates the process for the manufacturing of BN-Gas and assembly for a supercapacitor cell.

It should be noted that hydrothermal process accompanied by freeze-drying usually results in mechanically weak graphene 3D structures which limits their commercial applications. In addition, the hydrothermal temperature is commonly not high enough for efficient reduction of GO and hence, a subsequent reduction treatment is required to optimized the RGO sheets.

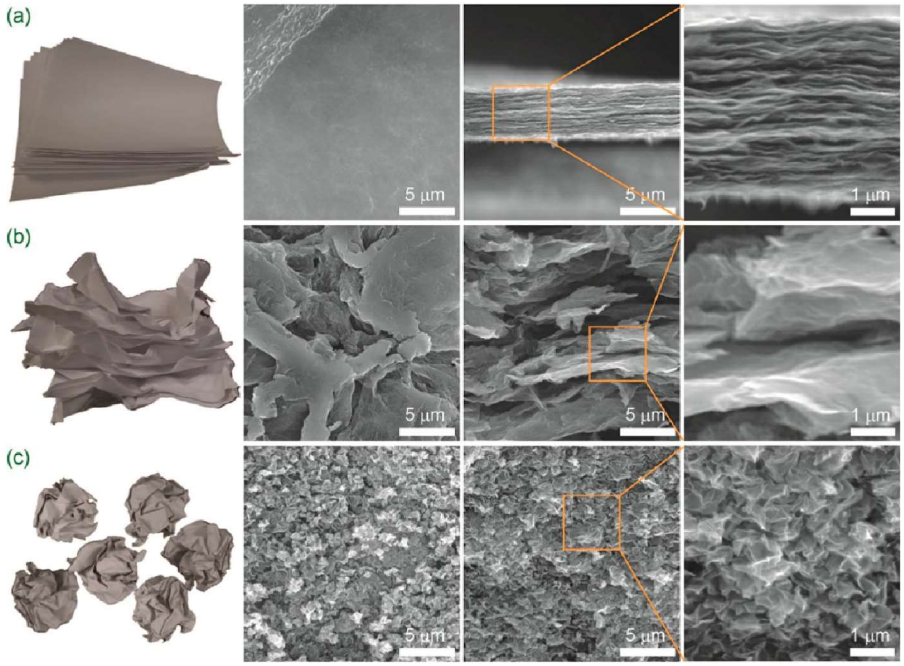

Figure 2.4. SEM images of a) flat, b) wrinkled, and c) crumpled graphene sheets. The schematic represents the paper models of each state. This Figure is reproduced with permission –See Letters of Copyright Permission (Courtesy of ACS Nano)[49].

The other methods introduced for the fabrication macroporous graphene-based 3D structures including chemical methods and CVD involve use of different chemicals and expensive procedure which make use of graphene-based structure limited to research area.

2.4 Summary

In this study, a powder-bed binder jetting additive manufacturing technique for the fabrication of graphene-based 3D structures is introduced which has a high potential for fabrication and commercialization of graphene-based devices.

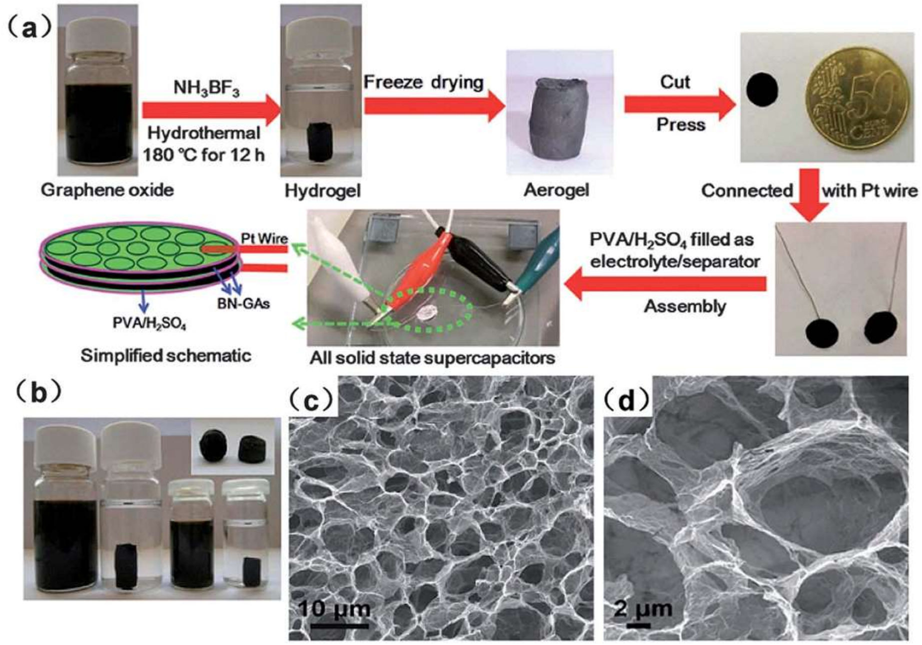

Figure 2.5. a) Fabrication and assembly process of BN-GAs for a supercapacitor cell, b) optical images of the fabricated GFs, and c) and d) SEM images of the BN-GAs microstructure This Figure is reproduced with permission –See Letters of Copyright Permission (Courtesy of Advanced Materials) [56].

Fabrication of graphene-based structures is an ongoing research activity and involves different techniques including use of GNM, CG, and self-assembly methods such as hydrothermal and CVD techniques. However, all these techniques have some drawbacks in fabrication and also final results. We will show that use AM technique can introduce a new path for the fabrication of macroporous 3D structures which can be potentially commercialized and used in different graphene-based devices.

Chapter 3

Additive manufacturing of graphene–hydroxyapatite nanocomposite structures[1]

3.1 Introduction

Graphene layer is the building block of most of the allotropes of carbon. It can be wrapped into the shape of a ball to make the 0-dimensional buckyball (fullerene) or rolled to form a 1-dimensional nanotube. It can also be stacked to make the 3-dimensional graphite. Graphene is a single sheet of sp^2-bonded carbon atoms in a honeycomb structure. Graphene was consistently considered as an unstable material until Geim and Novoselov exfoliated graphite to a single sheet of graphene in 2004 [53], [75], [79], [87]. Since then, there have been numerous studies on the applications of graphene in biological engineering (bioimplantation) [21], optics [22]–[27], water purification [8], [28], photocatalytic applications [6], supercapacitors [29], and batteries [30], [31]. Furthermore, many reports have been published on the synthesis of polymeric, metallic, and ceramic nanocomposites with graphene [4], [7], [11], [18], [20], [37]–[41]. However, to the best of our knowledge, in all the proposed fabrication techniques, there is no report on a proper manufacturing method for complex graphene-based macro-three dimensional (3D) shapes with high dimensional accuracy.

---

[1] This chapter is reproduced with permission –See Letters of Copyright Permission (Courtesy of International Journal of Applied Ceramic Technology)

Additive manufacturing (AM), as a novel manufacturing technology, has the potential to be employed for the fabrication of polymeric, metallic, and ceramic structures. Among different known techniques for AM, powder-bed Additive Manufacturing, so called 3D printing, is a powder based printing technique used for the fabrication of metallic and ceramic porous structures. AM of graphene-based structures can revolutionize its current applications in different fields like optics, supercapacitors, batteries, electronics, water purification, and bioimplantation. This technique enables fabrication of graphene 3D structures in complex shapes with different levels of porosity. However, graphene powder has a poor flowability which is a basic requirement for AM of a powder. There is a strong cohesive van der Waals force (5.9 kJ mol^{-1}) between graphene sheets which leads to a strong tendency for agglomeration [133].

Synthesis of graphene-based nanocomposites could yield a powder with a proper flowability. To this end, the synthesis of GHN powder through a wet mixing process and eventually, manufacturing of 3D structures from as-obtained powder is studied. Hap is a well-known calcium phosphate material (Ca10(PO4)6(OH)2) with a similar mineral phase to hard tissues of the body like bone. Despite a very similar chemical structure to bone, the mechanical strength and particularly, the fracture toughness of Hap structures are lower compared to that of natural bone [134]–[142]. Addition of different ceramic, metal, and polymer-based reinforcements has shown promising results concerning mechanical properties. However, the fabricated composites usually have adverse effects in bioapplications [44].

Among these, graphene seems to be a good candidate as reinforcement due to its exceptional mechanical properties. It was shown that graphene can facilitate the proliferation and adhesion of bone cells (osteoblasts) [44]. Also, it was reported that synthesized graphene/Hap composites show enhanced mechanical strength and elasticity modulus [45]-[15]. However, they all require complex synthesis processes. In addition, in the proposed techniques, there is no established method for the fabrication of porous complex 3D structures which is a necessity for bone implantation.

The aim of this study is to fabricate macro 3D structures of graphene/Hap nanocomposite. To achieve this goal, a facile wet mixing process is employed to synthesize the nanocomposite. Thereafter, the powder is used in the AM process to manufacture graphene-based 3D structures. Mechanical and physical properties of 3D-printed specimens are measured to investigate the effect of graphene on the properties of nanocomposite.

3.2 Experimental

3.2.1 Synthesis of graphene-hydroxyapatite nanocomposite

The nanocomposite was prepared through a dispersion-based/wet mixing process. Due to hydrophilic chemistry of Hap, the dispersion is to be prepared in an aqueous medium. Hence, hydrophilic graphene oxide dispersion (500 mg/L) purchased from Graphene Supermarket was employed instead of hydrophobic graphene. Graphene oxide sheets are decorated with different types of functional groups. Hydroxyl and epoxide groups are commonly placed perpendicular to the graphene layer while carbonyl groups like carboxylic acids are attached to the edges of the plane. These functional groups facilitate the dispersion of graphene in water. In order to prepare a well-dispersed composite of graphene, it is necessary to activate carboxyl groups on the graphene planes. 1-ethyl-3-(3-dimethylaminopropyl) carbodiimide (EDC) and N-hydroxysuccinimide (NHS) are well-known materials for the activation of carboxylic groups on carbon nano tubes (CNTs) and graphene sheets [143]–[151]. To functionalize graphene with EDC and NHS effectively, the hydroxyl (–OH) groups should be converted to carboxylic acid (-COOH) groups. To this end, Na(OH) and chloroacetic acid were added to graphene oxide dispersion and mixed on a magnetic stirrer for 2 hr. The dispersion was then sonicated in a bath ultrasonicator for 300 min. Next, EDC and NHS were added to the dispersion with an additional 30 min sonication.

Hap particles (calcium phosphate tribasic, 34-40% Ca) purchased from Alfa Aesar were dispersed in deionized (DI) water through vigorous stirring. Darvan C (Vanderbilt Minerals) was used as a dispersant to facilitate the dispersing process of Hap in DI water. Thereafter, activated graphene oxide (AGO) dispersion was added to the Hap dispersion drop-wise while stirring. To prepare the raw material for AM, a dry binder like PVA or starch (maltodextrine) must be premixed with the powder. In the current study, maltodextrine purchased from Sigma Aldrich (with the weight ratio of 1:2 to hydroxyapatite) was added to the dispersion and then, the whole dispersion was dried on the hotplate at 90°C. The dried powder is next grinded and sieved. The nanocomposite with three different contents of graphene was synthesized as indicated in

The software prepares the 2D slices of the model which are later incorporated into the 3D printing process. Figure 3.1 illustrates the fabrication process of the nanocomposite in

The particle size distribution of the powder is also given in Table 3.2. The three synthesized powders are used as the starting material for fabrication of 3D structures of graphene/Hap nanocomposite. The synthesized powder was characterized using X-ray diffraction (XRD) using an X-ray diffractometer (Rigaku DLMAX-2550 V) with CueK a radiation (λ = 1.54056 Å) and high-resolution field emission scanning electron microscope (Zeiss LEO 1550). The electron gun was operating at an accelerating voltage of 10 kV with chamber pressure below 1.5 × 10−5 mbar.

3.2.2 Three-dimensional printing (3DP) fabrication technique

Developed in MIT in 1990s, 3DP is among the most common AM processes due to a lower cost and simple operation. In order to fabricate 3D structures of graphene/Hap nanocomposite, the 3D model of the cylindrical structures (Ø: 4 mm, h: 6 mm) was developed by Computer-aided design (CAD) in SolidWorks Ver.2012 (SolidWorks Corp., Concord, MA, USA). The STL (stereolithography) format was uploaded into the 3D printing software (ZPrintTM).

The software prepares the 2D slices of the model which are later incorporated into the 3D printing process. Figure 3.1 illustrates the fabrication process of the nanocomposite in

Table 3.1. Composition of graphene/Hap nanocomposites synthesized to be printed by AM

	HG0	HG2	HG4
Graphene oxide to Hap (wt.%)	0	0.2	0.4

Table 3.2 Particle size distribution of the dried powder

Particle size (μm)	<45	45-75	75-106	>106
Percentage (%)	40-45	25-30	25-30	4-8

the AM machine (Zprinter® 310plus, Z Corporation, Burlington, MA, US). As seen, there are two powder beds whose z-positioning is adjusted with a piston underneath the bed. The powder is placed onto the feeding bed (as the main powder supply). A thin layer of the powder is also spread onto the building bed (Figure 3.1a). Next, the compartment moves forward, as shown in Figure 3.1b, to inject the aqueous binder (Zb$^{\text{TM}}$58) onto the building bed according to the CAD. Once one-layer of the liquid binder is injected on the building

bed, the feeding chamber piston pushes up the bed based on the predefined layer thickness. Then, the compartment moves backward to spread the next layer of the powder onto the building bed with the aid of rotating roller (Figure 3.1c). Subsequently, the as-spread layer of the powder is ready to be injected by the next layer of the aqueous binder. This process is iterated until the 3D structure is built up. When finished, the 3D structures are dried in the machine to set the liquid binder.

Powder layer thickness is one of the important factors in the process of AM. In particular, the resolution of the printed parts can be controlled by manipulating the powder layer thickness. Lowering the layer thickness improves the resolution of the parts. In particular, the layer thickness needs to be larger than the maximum particle size of the powder. However, lower particle size is also desirable for higher resolution of the parts. Three different layer thicknesses of 100, 125, and 175 µm were selected for the fabrication of 3D structures. These layer thicknesses were selected based on the maximum particle size of the powder. In addition to layer thickness, the other notable parameter in AM is the binder saturation level (binder concentration). There are two binder levels i.e. shell binder saturation level (SBS) and core binder saturation level (CBS) that must be specified before printing. For the first set of experiments, SBS and CBS levels were set to 100% and 400%, respectively (see Table 3.3). For the second set of experiments, the nanocomposites were 3D-printed at SBS/CBS level ratio of 100/200% at the layer thickness of 125 µm (as the most promising layer thickness). The compressive strength was measured using a 500 N load-cell (Instron 5548 Micro-Testing, MA, USA) with the loading rate of 0.2 mm/min.

Results and discussion

Figure 3.2 shows the XRD patterns of HG2 and HG4 nanocomposites. The peaks at $2\theta = 10.79°$ are related to (002) planes of graphene oxide. The SEM images of HG4 microstructure are displayed in Figure 3.3. As seen in Figure 3.3a, Hap particles are well-coated by nano particles. The nano particles seen in Figure 3.3 could be attributed to agglomerated graphene sheets forming spherical shape on the Hap particles. It has been shown that introduction of new particles with a smaller size can improve the flowability

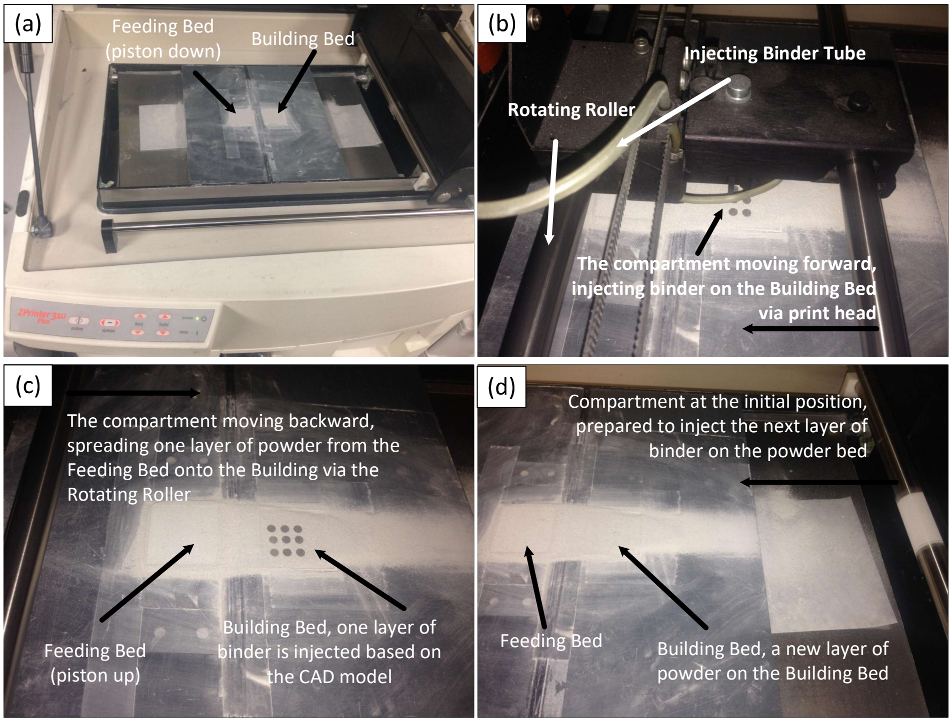

Figure 3.1 Fabrication process of 3D printed structures by 3DP, a) feeding bed and building bed are indicated, b) the compartment moves forward to inject the binder on the building bed, c) one layer of binder in injected on the powder bed, compartment moves backward to spread another layer of powder onto the building bed, and d) a new layer of powder is on the building bed waiting for the next layer of the binder.

Table 3.3 Process parameters for AM of the graphene/Hap nanocomposite. Tick marks show the samples printed at the specified layer thickness and binder saturation levels

Shell binder/Core binder Saturation level (%)	Samples	Layer thickness		
		100 µm	125 µm	175 µm
100/400	HG0	—	✓	—
	HG2	✓	✓	✓
	HG4	✓	✓	✓
100/200	HG0	—	✓	—
	HG2	—	✓	—
	HG4	—	✓	—

significantly through modifying the van der Waals forces between the particles [74]. If the new particles coat the host particles, the van der Waals force between the coated and uncoated particles is given by [74],

$$\frac{P_{coated}}{P_{uncoated}} \cong 2\,\frac{d}{\mathrm{D}}\,\frac{\Delta\gamma}{\Gamma} \cong 2\,\frac{d}{\mathrm{D}} \qquad (1)$$

where A is the Hamaker constant and h_0 is the minimum separation between the two particles. Usually, h_0 is considered to be 0.165 or 0.4 nm. D and d are the diameter of the host and guest particle, respectively.

Based on Figure 3.3, the average agglomerated particle size of graphene sheets is about 50 nm while that of Hap is above 5 µm. Therefore, according to Equation 1, the ratio of van der Waals force between coated and uncoated Hap particles is 0.02. It will be seen that flowability of the nanocomposite powder in contrast to Hap powder is improved remarkably as expected from the SEM images and Equation 1. Nonetheless, it should be noted that although lowering the particle size of both host and guest particles could facilitate the flowability, excess reduction in the host particle size increases the chance of agglomeration which has adverse effects on flowability [152]. As expected, the flowability of graphene/Hap nanocomposite powder (HG2 and HG4) is far better than HG0. Figure 3.4 exhibits the flowability of HG4 and HG0 during AM process. A smooth layer of HG4 powder can be seen on the building bed during the printing process (Figure 3.4a and b) while HG0 powder is poorly spread on the building bed (Figure 3.4c and d).

As seen in Figure 3.1, nine samples from each batch are built during the AM process. Figure 3.5 displays the porous 3D structures of HG0, HG2, and HG4 printed through AM.

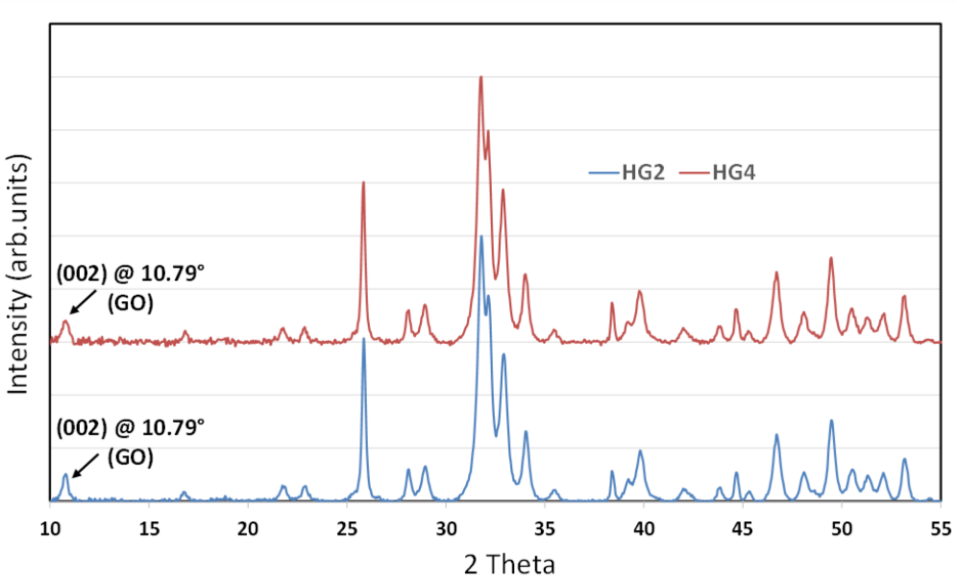

Figure 3.2 XRD patterns of HG2 and HG4. GO peaks at 2θ = 10.79° are shown on the patterns.

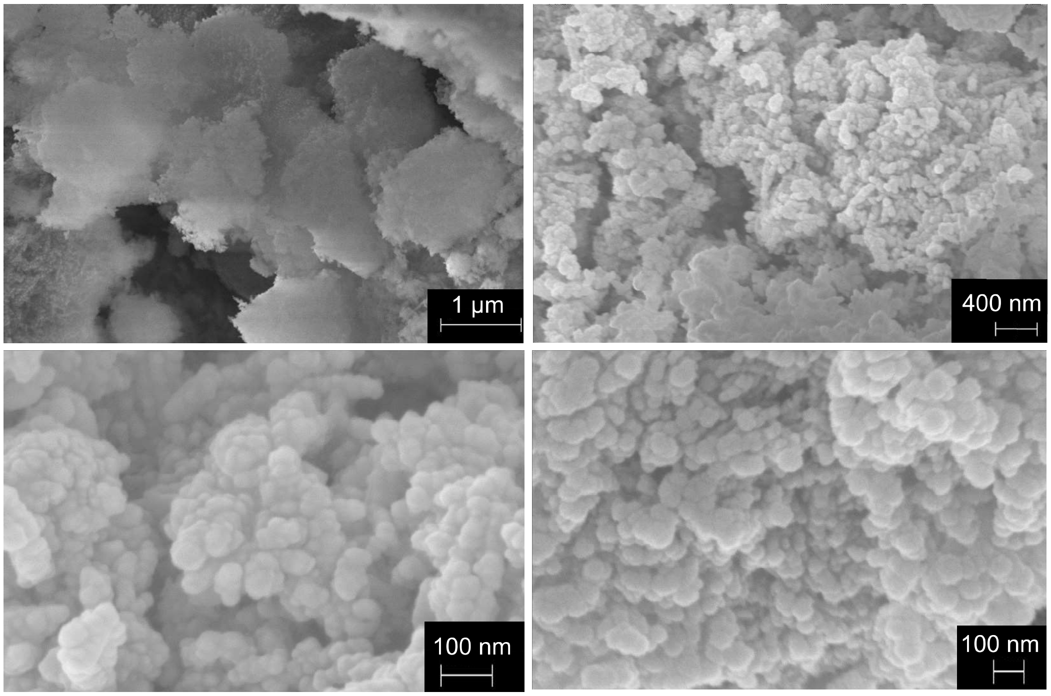

Figure 3.3 SEM images of HG4 nanocomposite, (a) graphene coated Hap particles; (b), (c), and (d) show higher magnifications. The nanoparticles seen in (b), (c), and (d) could be attributed to agglomerated graphene oxide sheets.

The cold crushing strength (CCS) of HG2, HG4, and HG0 at layer thicknesses of 100, 125, and 175 μm with SBS/CBS ratio of 100/400% and 100/200% is shown in Figure 3.6.

The typical stress-strain graphs of the samples are also depicted in Figure 3.7. The samples printed at layer thickness of 100 and 175 μm with the CBS level of 400% exhibited the lowest CCS compared to that of 125 μm. The reason could be attributed to the interaction of injected liquid binder with the powder layer. For the samples 3D-printed at layer thickness of 100 μm, the powder layer is oversaturated with the liquid binder. This phenomenon can cause the particles to drift, thereby disturbing the orientation and positioning of the particles in the powder layer. Also, too much wetting can disintegrate the grains into smaller particles which can result in loosened powder bed and lower the mechanical strength. However, the binder still maintains the structure from collapse. The compressive strength of HG2 and HG4 samples are almost similar and extends between 0.25-0.55 MPa.

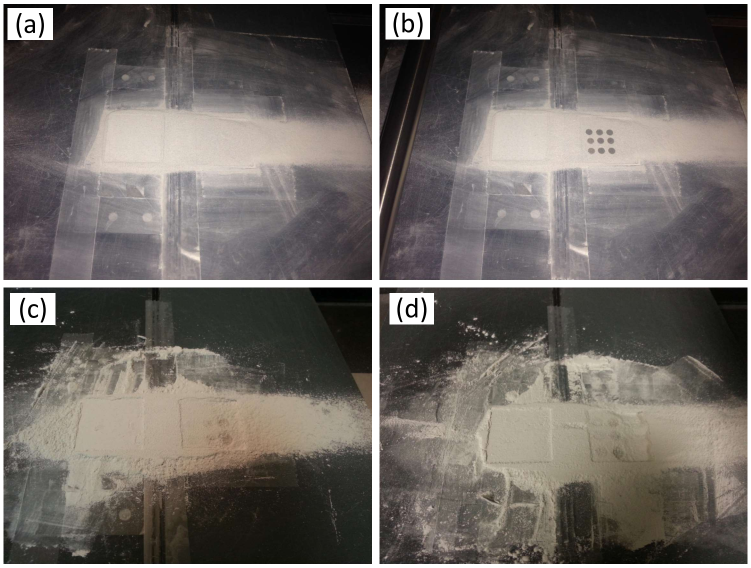

Figure 3.4 Comparison between spreadability of (a) and (b) HG4 with (c) and (d) HG0 during AM process. HG4 powder shows very smooth flowability in contrary to HG0.

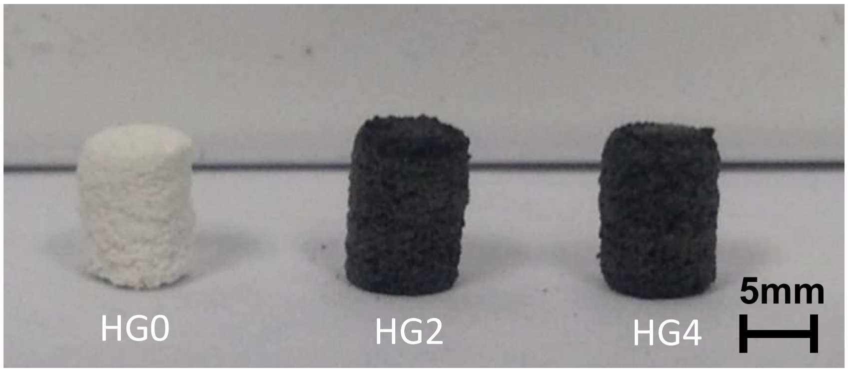

Figure 3.5 Porous structures (cylinders) of HG0, HG2, and HG4 fabricated by 3DP.

On the other hand, at the layer thickness of 175 μm, the liquid binder saturation is inadequate to reach the neighboring powder layers. Therefore, the structures are loose with a very low compressive strength in the range of 0.05-0.1 MPa. Similar to the layer thickness of 100 μm, there is almost no difference between HG2 and HG4 samples since there is no primary adherence between the particles. The HG0 structures were also extremely weak and could not be handled for the compression test.

The layer thickness of 125 μm produced the strongest structures compared to the other selections. As indicated in Figure 3.6 and Figure 3.7c, the compressive strength of HG0 samples with no added graphene is about 0.14 MPa whereas that of HG2 is 10 times more than HG0 structures. Interestingly, the compressive strength of HG4 samples with 0.4 wt.% graphene content is about 70 times more than HG0 samples. This result is a remarkable improvement of the mechanical strength which can bring the hope of using similar structures for load-bearing applications. It has been reported that the compressive strength of cancellous bones is in the range 2-12 MPa [152] and the average strength of HG4 samples were measured to be around 7 MPa. The tangential modulus of HG4 samples is also higher than that of HG2.

There are several reasons to explain the improvement in the mechanical strength via graphene. Graphene is known to bestow superior mechanical properties to the composites. Graphene flakes have a high surface area exposed to the matrix. The wrinkled graphene sheets effect an improved mechanical interlocking with the particles, thereby increasing the resistance of the microstructure to crack propagation. Furthermore, two-dimensional (2D) fillers like graphene can bear both longitudinal and lateral loads whereas other allotropes of carbon like carbon nanotubes can only bear the load along the longitudinal axis which highlights the importance of their orientation inside the matrix. Hence, even random distribution of graphene flakes can be influential in the inhibition of the crack propagation [12], [77], [79].

There are also several mechanisms that can help to increase the fracture toughness and the strength of the composites. Crack deflection is a well-known and effective mechanism for dumping the crack propagation energy. When a crack reaches the second phase in the matrix, it has to spend a higher energy to cut through the particle. The crack can also pass around the second phase which is called crack deflection.

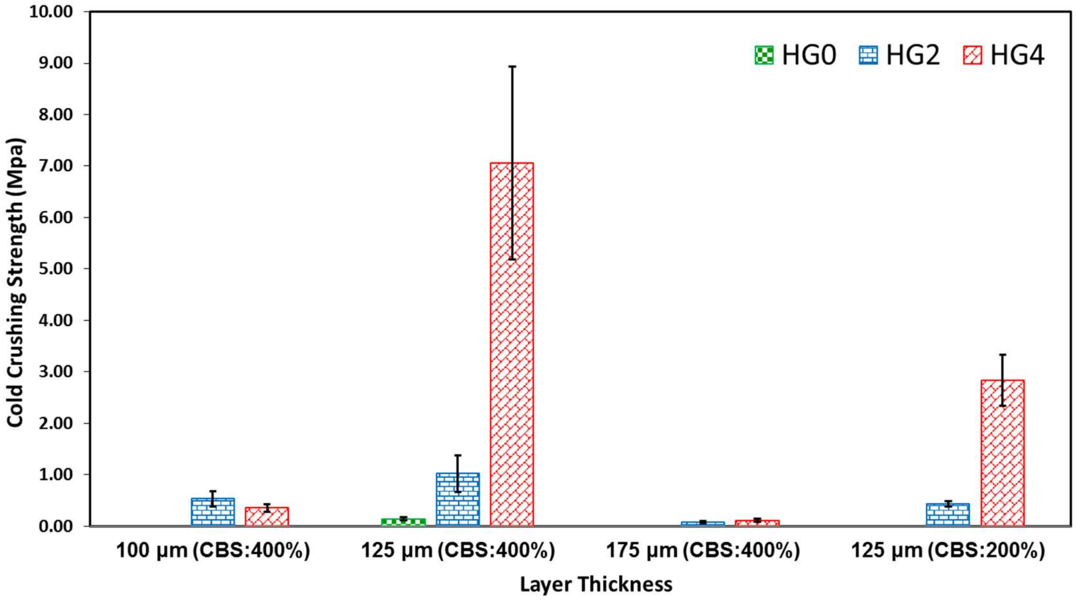

Figure 3.6 Cold Crushing Strength of HG0, HG2, and HG4 specimens 3D-printed at layer thicknesses of 100, 125, and 175 µm with SBS/CBS ratio of 100/400% and 100/200%.

Obviously, the energy of the cracks can barely cut through a graphene flake with the Young's modulus of over 1 TPa and a strong cohesive force of about 5.9 kJ mol^{-1}. Therefore, crack deflection will be the main mechanism in dissipating the energy of the cracks. Figure 3.8 shows the SEM fracture surface images of the HG4 samples. The black arrows point to the crack deflection inside the matrix. The crack propagation through a zigzag path can also been observed in Figure 3.8c. Both phenomena which are unconventional for ceramics lead to considerable energy dissipation of the crack. On the contrary, in brittle ceramics cracks usually follow a straight path which lowers their fracture toughness considerably. This could be the main reason for significant raise in the strength of the HG4 samples compared to HG0 and also HG2 structures. The similar mechanisms have also been reported recently [5], [36], [37], [153].

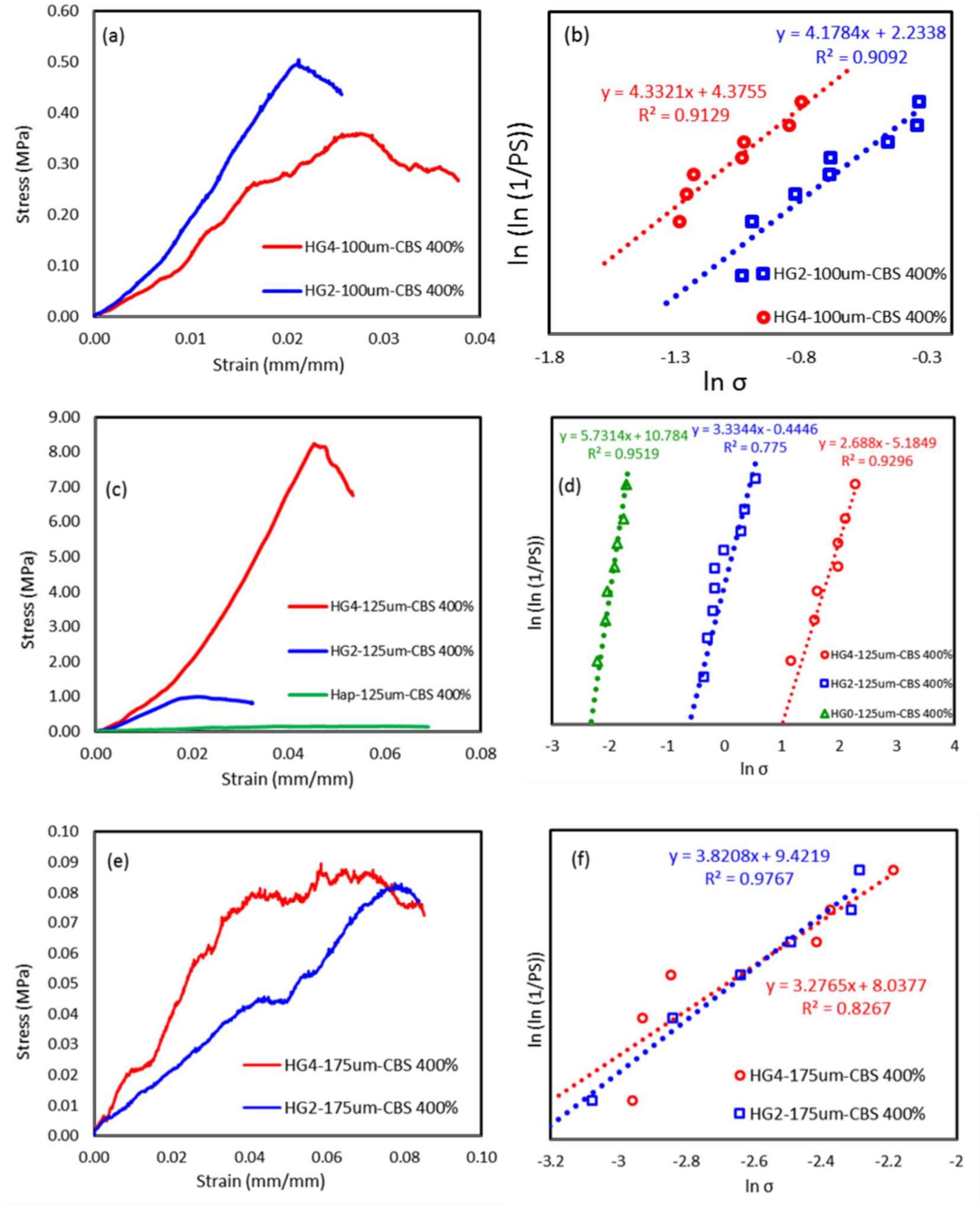

Figure 3.7 Stress-Strain (SS) and Weibull Distribution (WD) curves of the printed samples with the shell to core binder sturation level of 100/400%, a) SS curves of HG2 and HG4 at the layer thickness of 100 µm, b) WD of HG2 and HG4 at the layer thickness of 100 µm, c) SS curves of HG0, HG2 and HG4 at the layer thickness of 125 µm, d) WD of HG0, HG2 and HG4 at the layer thickness of 125 µm, e) SS curves of HG2 and HG4 at the layer thickness of 175 µm, and f) WD of HG2 and HG4 at the layer thickness of 175 µm.

The Weibull distribution plots of HG2 and HG4 specimens printed at the layer thicknesses of 100, 125, and 175 µm are illustrated in Figure 3.7b, d, and f. The Weibull modulus for specimens is also given in Table 3.4.

In order to investigate the effect of binder concentration on the strength of the structures, the samples were also printed with a SBS to CBS ratio of 100/200% at the layer thickness of 125 µm. As observed in Figure 3.9, the average compressive strength of HG4 and HG2 structures is 3.5 and 0.4 MPa, respectively. However, the mechanical strength of HG4 is still 8 times more than that of HG2 which is comparable to the structures printed with the with SBS to CBS ratio of 100/400% at the layer thickness of 125 µm. The tangential modulus of HG4 samples is also significantly higher than HG2 indicating the more active crack deflection mechanism in HG4 structures. The Weibull modulus of HG4 (5.47) is depicted in Figure 3.9b.

Porosity and bulk density of the HG4 and HG2 samples printed at the layer thickness of 125 µm were measured using ethanol displacement according to the Archimedes method. As presented in Table 3.5, the porosity of HG2 and HG4 are both more than 50% while the bulk densities are around 1.2 g/cm3. The mechanical strength of HG0 samples were extremely low so they dissolved in ethanol. Therefore, their porosity and bulk density could not be measured.

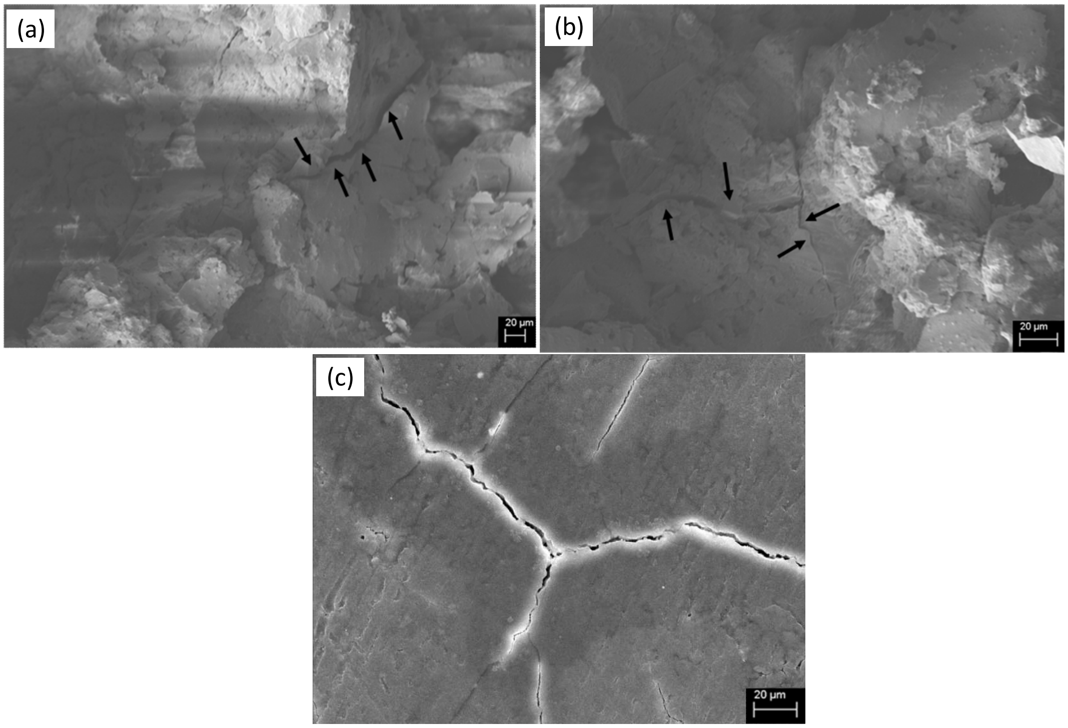

Figure 3.8. SEM images of the fracture surface of HG4 samples. The arrows indicate the crack deflection inside the matrix.

Table 3.4. Weibull modulus of HG4, HG2, and HG0 at three different layer thicknesses with SBS/CBS ratio of 100/400%

Layer thickness	Weibull modulus		
	HG2	HG4	HG0
100 µm	4.178	4.33	N/A
125 µm	3.334	2.688	5.731
175 µm	3.821	3.277	N/A

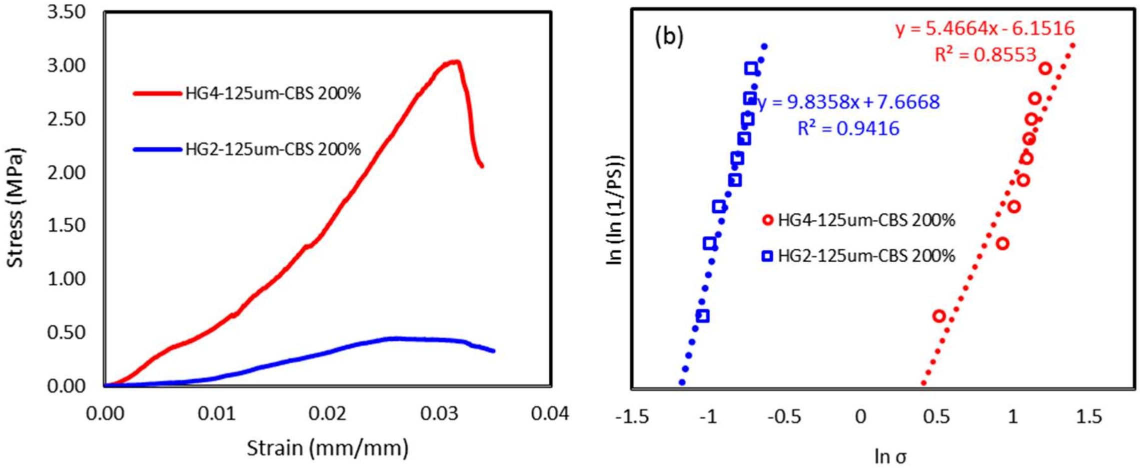

Figure 3.9Stress-Strain (SS) and Weibull Distribution (WD) curves of the printed samples with the shell to core binder sturation level of 100/200%, a) SS curves of HG2 and HG4 at the layer thickness of 120 µm, b) WD of HG2 and HG4 at the layer thickness of 120 µm.

Table 3.5 Average porosity and bulk density of HG2 and HG4.

Sample	Average Porosity (%)	Average Bulk Density (g/cc)
HG.02	51.63	1.266
HG0.4	55.27	1.196

3.3 Conclusion

Graphene/Hap nanocomposite powder was printed into 3D structures successfully via AM process. It was shown that flowability of the nanocomposite was improved significantly in contrast to HG0 powder with no graphene content. The samples were printed at different layer thicknesses and binder saturation levels as process parameters of AM. It was realized that the compressive strength of samples printed at the layer thickness of 125 μm and SBS/CBS ratio of 100/400% was substantially higher than that of 100 and 175 μm. Also, the mechanical strength of HG4 specimens were almost 70 times more than HG0 specimens. In the end, AM was introduced as a novel technique for the fabrication of complex 3D shapes of graphene/Hap nanocomposites with an improved mechanical to be used for load-bearing bioapplications.

Chapter 4

The impact of reduction method on the supercapacitor performance of additive manufactured graphene electrodes

4.1 Introduction

In certain applications such as memory backup systems, engine starters, and regenerative breaking in trains and electric cars, it is vital to use a durable and reliable energy storage system capable of rapidly and efficiently accepting and releasing energy. While batteries are the most frequently used type of rechargeable energy storage, they are inefficient at high power densities and must be significantly over-sized to meet these demands. Supercapacitors are an ideal alternative for batteries in the above-mentioned applications. In supercapacitors, also known as electrical double layer capacitors (EDLCs), rearrangement of charge carriers (electrons or ions) occurs rapidly at the electrode/electrolyte interface to form an electric double layer (EDL) resulting in a very high power density. However, the amount of energy which can be stored in commercial supercapacitors is less than batteries (10-20 Wh kg^{-1} versus 150-300 Wh kg^{-1}) [46]–[48]. Therefore, it is of high importance to develop a supercapacitor device with high energy density to meet the requirements of the industrial applications.

There have been numerous studies to improve the energy density of supercapacitors. Performance of supercapacitors is profoundly dependent on the specific surface area of the electrode material and its compatibility with the electrolyte [49], [50]. Carbon-based materials including activated carbons (ACs) and carbon nanotubes (CNTs) with high surface area are more attractive than conducting polymers and metal oxides due to their high cycle stability, higher electrical conductivity, better compatibly with electrolyte, and lower cost [29], [51], [52]. However, ACs and CNTs commonly reach 10-20% of their expected capacitance [29] due to limited accessibility of the electrolyte to the micropores, insufficient wetting of the electrode material with the electrolyte, and contact resistance with the current collector [154]. In contrast, graphene-based materials with exceptional theoretical properties such as specific surface area up to 2675 m^2/g, promising performance at high densities of electric current [53], and more importantly, theoretical specific capacitance of 450 F/g for functionalized graphene [48] is an excellent candidate to replace other allotropes of carbon in the supercapacitors.

The performance of graphene-based electrodes is however greatly affected by various factors such as the quality of the synthesized graphene, fabrication of electrodes, and the assembly of the cells, which is an ongoing investigation. The aim of these studies is to maximize double-layer capacitance (C_{DL}) and/or pseudocapacitance ($C_{Ø}$) of the electrodes. The proposed synthesis methods mostly involve a complex and time-consuming process for the synthesis of graphene to reach high capacitance values such as 284.5 F/g [51], 265 F/g [155], 255 F/g [156], and 150 F/g [49]. In-situ self-assembly [54], chemical vapor deposition [55], and hydrothermal method [56] are also reported as common fabrication techniques for graphene-based electrodes. Nevertheless, manufacturing of thick graphene-based electrodes for commercial applications is still challenging. The most common method is through mechanical compaction of the powder pre-mixed with a binder to be assembled into a cell [57]. However, these electrodes have limited accessible pore volume which limits their C_{DL}.

In this research, we introduce a novel approach for the manufacturing of pure graphene electrodes using a binder-jet powder-bed additive manufacturing (AM) technique [58]. Three-dimensional structures can be fabricated in a layer by layer fashion using AM, particularly when a complex shape is to be made in a short period of time. In addition, as reported elsewhere [59]–[62], 3D structures manufactured by powder-bed AM technique may have a porosity in the range of 35-50% which can provide a significant effective surface area as the interface between the electrolyte and the electrode for the formation of EDL. To conduct this study, chemically reduced graphene oxide (CRGO) was synthesized and employed as the electrode materials. In order to avoid the restacking of CRGO sheets after reduction, PVA was added at different concentrations to the GO dispersion before addition of HI acid. The samples were drop-cast and tested for their capacitance in a supercapacitor cell. The sample with the higher capacitance and better performance was selected as the material for AM. Additionally, GO was reduced through thermal exfoliation and used it for 3D-printing of supercapacitor electrodes. We finally compared the effect of the reduction process on the performance of supercapacitor electrodes fabricated through the powder-based AM technique.

4.2 Experimental

4.2.1 Synthesis of graphene oxide

Graphene oxide (GO) was synthesized through an improved Hummer's method as reported by Marcano et al. [157]. Briefly, 3.0 g of graphite (Graphite flake, -10 mesh, Alfa Aesar, MA) and 18.0 g of $KMnO_4$ were added slowly to a 9:1 mixture of sulfuric acid and phosphoric acid. The dispersion was heated to 45 °C and stirred for 16 h. Then, it was poured onto 400 mL of ice followed by slow addition of 10 mL H_2O_2. Upon reaction with H_2O_2, the dark greenish color of the dispersion changed to light brown which indicates the conversion of graphite to graphene oxide. The dispersion was centrifuged to remove the supernatant and then washed successively with HCl and ethanol. The mixture was stored in a copious amount of ethanol for further experiments.

4.2.2 Reduction of graphene oxide

HI acid has been reported by various researchers as an effective chemical reagent for the removal of the functional groups [158]–[162]. As proposed by Moon et al. [161], 4.0 g of graphene oxide was dispersed in acetic acid and bath-sonicated for 1 h. In order to minimize the restacking of graphene sheets after reduction, polyvinyl alcohol (PVA) dissolved in distilled water at different concentrations was added to the GO in acetic acid (10-40 wt.% of GO), and further sonicated for an extra hour. Next, 80.0 mL of 55% HI acid (Sigma-Aldrich Corporation) was poured very slowly into the dispersion and stirred at 90 °C for 2 h. Upon cooling to room temperature, it was filter-washed with saturated sodium bicarbonate, distilled water, and acetone, successively. The chemically reduced graphene oxide (CRGO) was vacuum dried at 60 °C overnight.

For thermal reduction, 55.0 mg of dried GO was put in a silica glass tube which was vacuumed and filled with Argon, successively. The tube was then quickly placed into a tube furnace (Lindberg/Blue M™ Mini-Mite™ Tube Furnace) preheated to 1100 °C for 1 min. Once exposed to heat, the light brown GO sheets immediately exfoliated to a dark black fluffy powder with a weight loss of ~ 70% corresponding to previously published reports [163].

4.2.3 Drop-cast of electrodes

A stable dispersion of CRGO at different concentrations of PVA was prepared in 1,2-dichloroethane (DCE) which is reported as an efficient organic solvent for reduced graphene oxide sheets [48], [164]. The dispersion was drop-cast on stainless steel bars and assembled in Swagelok cells to explore the effect of HI reduction and also PVA on the performance of graphene electrodes. The amount of active material in the samples with no PVA (CRGO) was 0.550 mg. The concentration of PVA in the next samples was 10 (CRGO1), 20 (CRGO2), 30 (CRGO3), and 40 wt. % (CRGO4), respectively. CRGO sheets were characterized using SEM (Zeiss, LEO 1530 Gemini) and EDX to inspect the graphene sheets and explore C/O ratio, respectively.

4.2.4 Additive manufacturing of electrode disks

To print the 3D structures, a sliced CAD model (STL file) of the object is uploaded into a retrofitted three dimensional printing (3DP) machine (ZPrint 310 Plus, 3D Systems, Burlington, MA). The structure is built up in a layer-by-layer fashion as reported in [61], [165]–[167]. In summary, a layer of powder is first spread onto a build bed from feed bed through a rotating motion of a roller. Next, an aqueous-based binder (zb®60 binder clear, Z Corporation, Burlington, MA) is injected onto the new layer on the build bed based on the geometry of the first CAD slice of the 3D-structure. This process is iterated until the object is fully built up. The layer thickness adopted for each iteration was 100 μm with the shell binder to core binder ratio of 100:200%. The fabrication process was conducted in a chamber at the temperature of 35 °C. All the electrode disks were manufactured with the diameter and thickness of 12 mm and 300 μm (3 layers of powder), respectively. According to MSDS of zb®60, the binder consists of 85-95 wt.% water. For TRGO disks, no additive was pre-mixed with TRGO powder before the AM process to obtain pure reduced graphene oxide electrodes. The details of the process are illustrated in Scheme 1.

4.2.5 Assembly of the Supercapacitor Cells

After printing, the electrodes were placed onto an aluminum mesh and assembled in the Swagelok cells in a two-electrode configuration. Nitrocellulose filter papers immersed in 1M sulfuric acid overnight were used as the separator. 1M H_2SO_4 electrolyte was also added drop-wise to both electrodes before assembly. The cyclic voltammetry (CV) test was conducted using an electrochemical workstation Potentiostat/Galvanostat at the scan rates of 5 mV/s to 100 mV/s. The specific capacitance is calculated according to equation 1:

$$C = 2\frac{i}{{\Delta V}/{\Delta t}\, m} \qquad (1)$$

where i is the average current, $\Delta v/\Delta t$ scan rate, and m mass of one electrode. To measure areal capacitance, mass is replaced with the surface area of one electrode.

4.3 Results and discussion

The microstructure of the synthesized CRGO powder is shown Figure 4.1. It is well-known that exfoliation and chemical oxidation of graphene layers from graphite is associated with the introduction of functional groups (such as hydroxyl, epoxy, carbonyl, and carboxyl groups) onto the surface of graphene layers. These groups react with some of the sp^2 bonded carbon atoms on the honeycomb structure of graphene and convert them into sp^3 bonded atoms. This reaction limits the concentration and mobility of carriers in the sheet. In addition, conjugated structure of the graphene sheets breaks through

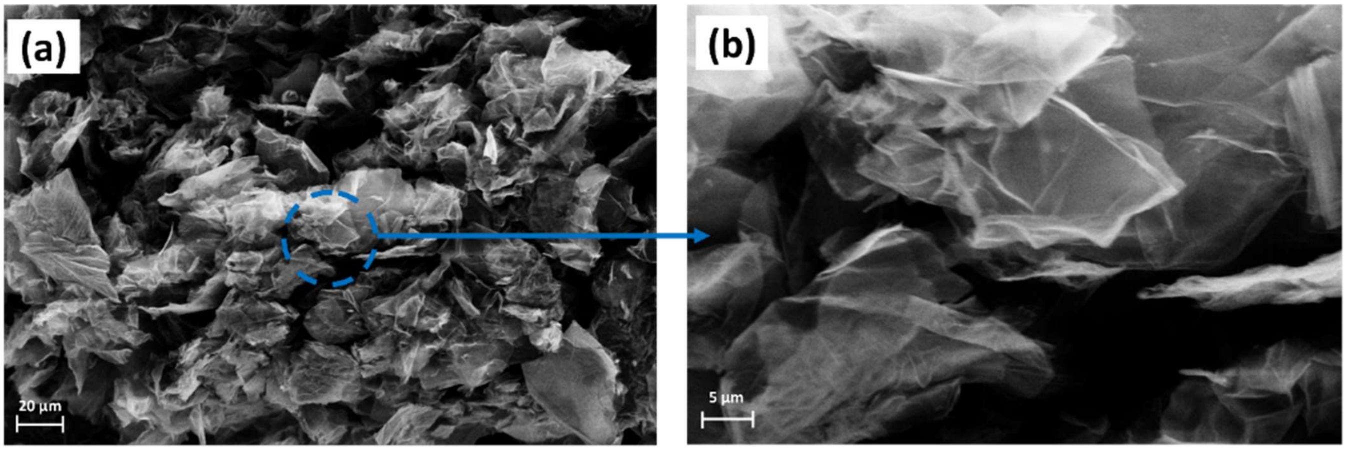

Figure 4.1. SEM images of the CRGO powder indicating wrinkled and crumpled graphene sheets.

functionalization which blocks the pathway for the mobility of carriers. The reduction of graphene oxide is therefore aimed at the removal of functional groups and also reviving the structure of graphene lattice. The crumpled and corrugated layers are a typical indication of exfoliation and reduction of graphene sheets, respectively, as seen in Figure 4.1. The higher magnification micrograph in Figure 4.1b indicates the lateral dimension of more than 30 µm for the reduced graphene sheets. The lateral sizes more than sub-micrometer is a sign of proper restoration of the conjugated structure of the graphene sheets [168].

Figure 4.2 shows the CV test results of the drop-cast samples at scan rates of 10, 20, and 50 mV/s. CRGO1 to CRGO4 samples (Figure 4.2b-e) were preloaded with 10 to 40 wt.% PVA, respectively. Further addition of PVA improves the capacitance of the cells as more charge per unit time (current) can be stored at the interface of the electrode and the electrolyte. Figure 4.2f illustrates the specific capacitance (Cs) of CRGO with PVA preloaded electrodes at three different scan rates.

In Figure 4.3, C/O ratio of CRGO is compared with the other electrodes. It should be noted that EDX is not a quantitative but more a qualitative technique for the study of C/O ratio in reduced graphene oxide sheets unless a very flat surface of the material is used for the test. According to Figure 4.3, it is clear that the addition of PVA distorts the effect of HI acid in the reduction of GO sheets and removal of the oxygenated groups (C/O ratio of CRGO:CRGO4 ; ~12:~2, respectively). As reported by Salavagione et al. [169], PVA can react with GO through hydrogen bonding and covalent linkage which limits the accessibility of iodine atoms from HI to the functional groups for halogenation substitution reaction [162]. As seen in Figure 4.2a, b, and f, Cs of CRGO1 drops significantly compared to CRGO which could be attributed to the reaction of PVA with GO and subsequently, inefficient reduction process. However, a gradual increase in the capacitance is observed when more PVA is added to the samples which could be attributed to the effect of PVA in minimizing the restacking of RGO sheets.

Graphene sheets have shown a high inclination to agglomeration due to the π-π interaction and van der Waals force between the layers [48], [164], [170]. Restacking of graphene sheets reduces the accessible surface area to the electrolyte and limits formation of EDL in the electrode. Polymers have widely been studied as graphene dispersion stabilizers to avoid the restacking of graphene sheets [164], [171]–[173]. Herein, PVA is hypothesized to provide spatial hindrance and increase ion accessible surface area of the graphene electrodes. It can be seen in Figure 4.2c-f that further addition of PVA increases Cs until it reaches near the Cs values of CRGO in CRGO4 (77 F/g). Moreover, at higher scan rates, CRGO4 shows a better performance than CRGO which can be related to higher ion accessible surface area of the graphene sheets in the electrodes and improved ion transport through the EDL. Therefore, at the first round of experiments, CRGO and CRGO4 powder were selected to be employed as the raw material for the manufacturing of electrode disks using AM technique. Figure 4.4a displays the optical image of the 3D-printed disks placed on an aluminum mesh. The disks were assembled in a symmetrical Swagelok cell for further experiments.

The CV test results for CRGO and CRGO4 disks are exhibited in Figure 4.5. Although a fully double-layer capacitance can be observed due to the nearly rectangular shape of the graphs, Cs values for both samples were low in the range of 30 F/g (73 mF cm-2). Owing to the limitations of ZPrint 310 Plus (3D printing machine) in the motion of the feed bed, the minimum thickness obtained was 300 µm. Stoller et al. [174] and Hu et al. [175] have reported that thicker electrodes lead to higher ESR (equivalent series resistance) and lower capacitance of the supercapacitor. In addition, notwithstanding a noticeable contact surface area between the disks and the electrolyte, a high amount of porosity in the disks results in a low packing factor and thus lower conductivity. These two properties of the 3D printed disks highlights the need to use a powder with higher conductivity than the chemically reduced graphene oxide.

There have been numerous studies on reduction strategies to remove functional groups and improve electrical conductivity of graphene sheets. Most of the proposed methods can be categorized into chemical and thermal reduction techniques [176]. In chemical reduction, deoxygenation is selective and depends on the chemical reactions between the reducing agent and the functional groups.

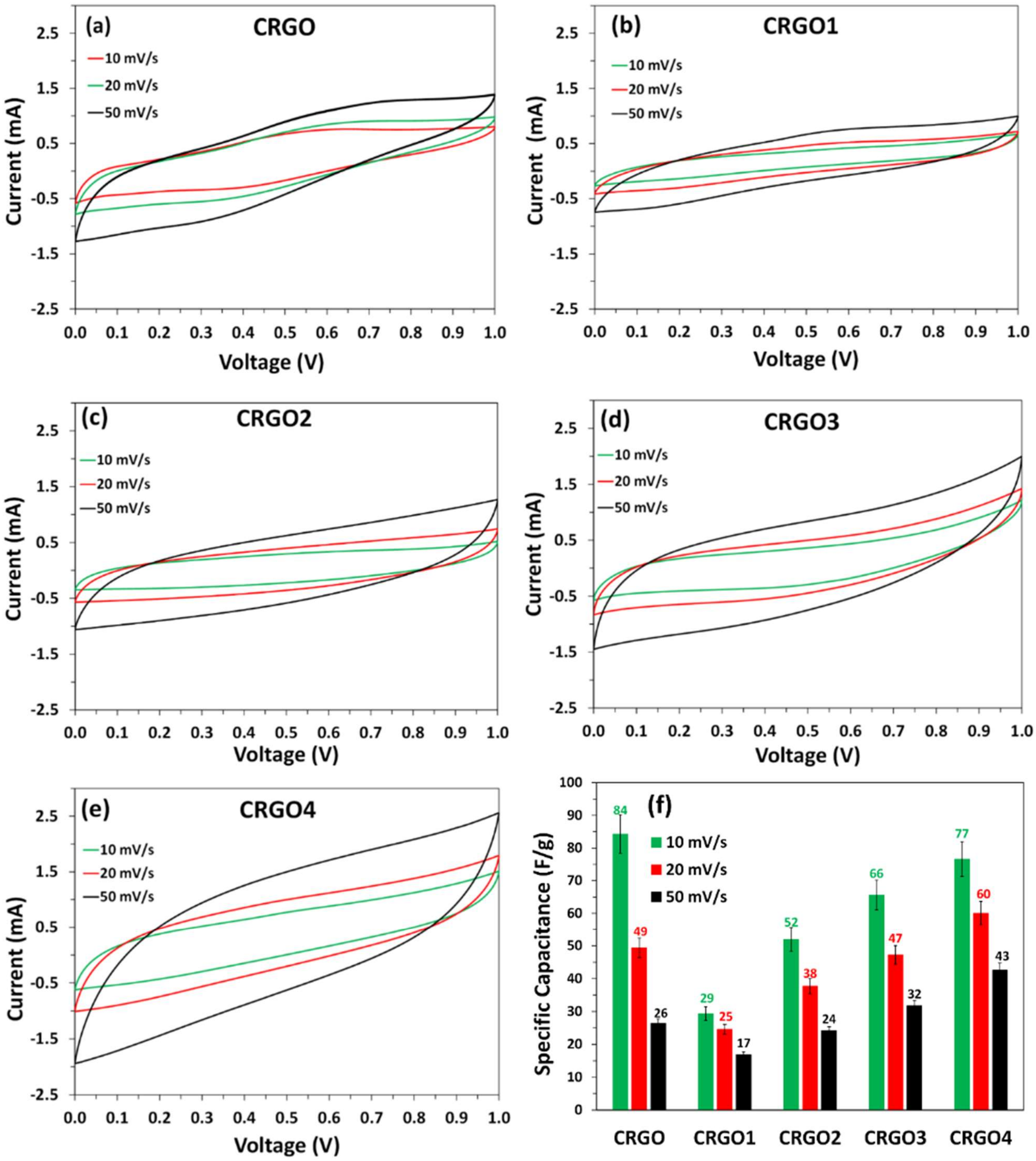

Figure 4.2. CV test results of a) CRGO, b) CRGO1, c) CRGO2, d) CRGO3, e) CRGO4 at the scan rates of 10, 20, and 50 mV/s, f) comparison of the C_s values of the drop-cast samples.

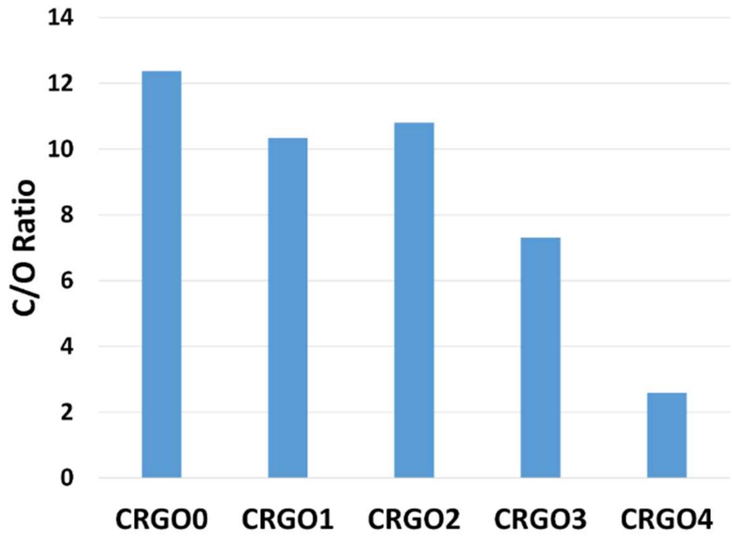

Figure 4.3. C/O atomic ratio of CRGO samples preloaded with PVA after chemical reduction with HI acid.

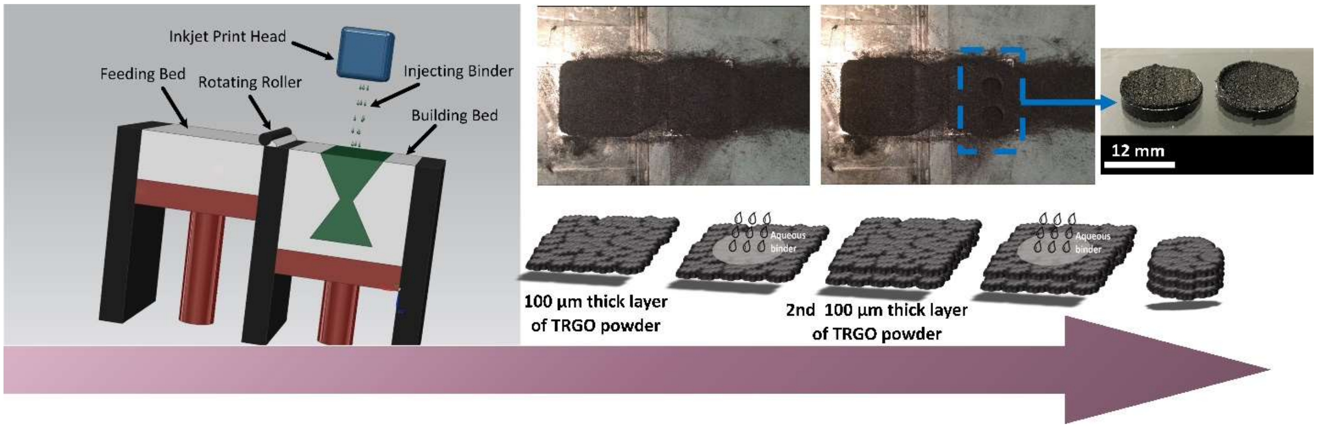

Figure 4.4. Schematic representation of the powder-based AM process illustrating the optical image of the feed bed and the build bed after the printing process (printed disks can be seen in the build bed) and the optical image of the printed disks with the diameter of 12 mm and thickness of 300 µm, respectively, placed on the aluminum mesh.

HI acid is proposed to be a very effective reducing agent through ring-opening of epoxy groups and halogenation substitution of hydroxyl groups. Although chemically reduced graphene oxide sheets using HI acid demonstrate high electrical conductivities (~300 S/cm) compared to the other chemical reagents [161], [162], thermally reduced graphene sheets have shown higher conductivity values due to higher C/O ratios. It has been demonstrated that chemical reduction yields less conductive material (100-300 S/cm) than the thermal reduction of graphene oxide (700-1000 S/cm) [114], [163], [176], [177]. The elimination of the functional groups in thermal reduction relies on their binding energy to the graphene sheet. It has been reported that most of oxygenated groups such as hydroxyl and carboxyl groups will be removed through annealing in vacuum at temperatures of 700-1200 °C yielding C/O ratio of 14 [168]. Higher annealing temperatures can produce reduced graphene oxide sheets with a C/O ratio of 300 [177].

To compare with CRGO and CRGO4 electrodes, the as-prepared thermally reduced graphene oxide (TRGO) powder was also 3D-printed using binder-jet powder-bed AM technique. The printed TRGO electrodes were assembled with a similar process as CRGO electrodes in a Swagelok cell. Figure 4.6 depicts the results of the CV test and the capacitance of the TRGO electrodes at different scan rates. It is expected that the printed TRGO disks outperform their CRGO counterparts due to anticipated higher conductivity values. In addition, it is generally accepted that the powder obtained from thermal reduction of graphene oxide should have higher specific surface area compared to that of chemical reduction [178]. The Cs of TRGO disks at the scan rate of 5 and 10 mV/s is 160 and 110 F/g, respectively which is 3-4 times higher than that of CRGO electrodes. In spite of high Cs values at low scan rates, there is a pronounced drop in capacitance at higher scan rates (50% from 5 mV/s to 20 mV/s) which can be attributed to the insufficient conductivity of the TRGO powder for 300 μm thick electrodes. As illustrated in Figure 4.6c, the areal capacitance of the TRGO disks at the scan rate of 5 mV/s is more than 200 mF/cm2 which

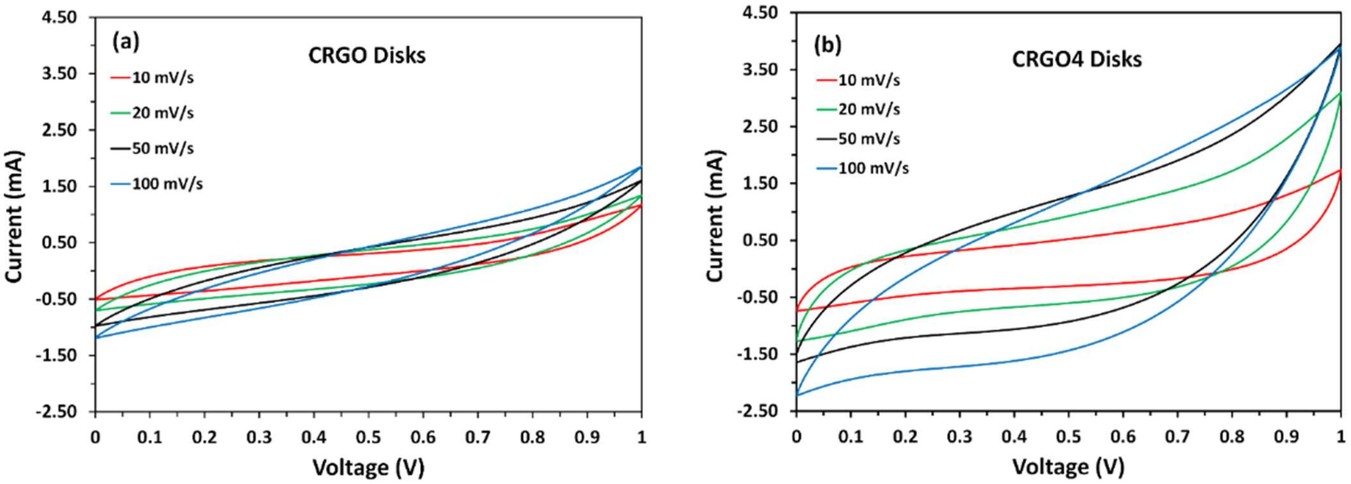

Figure 4.5. CV test results of the 3D-printed CRGO (a) and CRGO4 (b) disks at the scan rates of 10, 20, 50, and 100 mV/s.

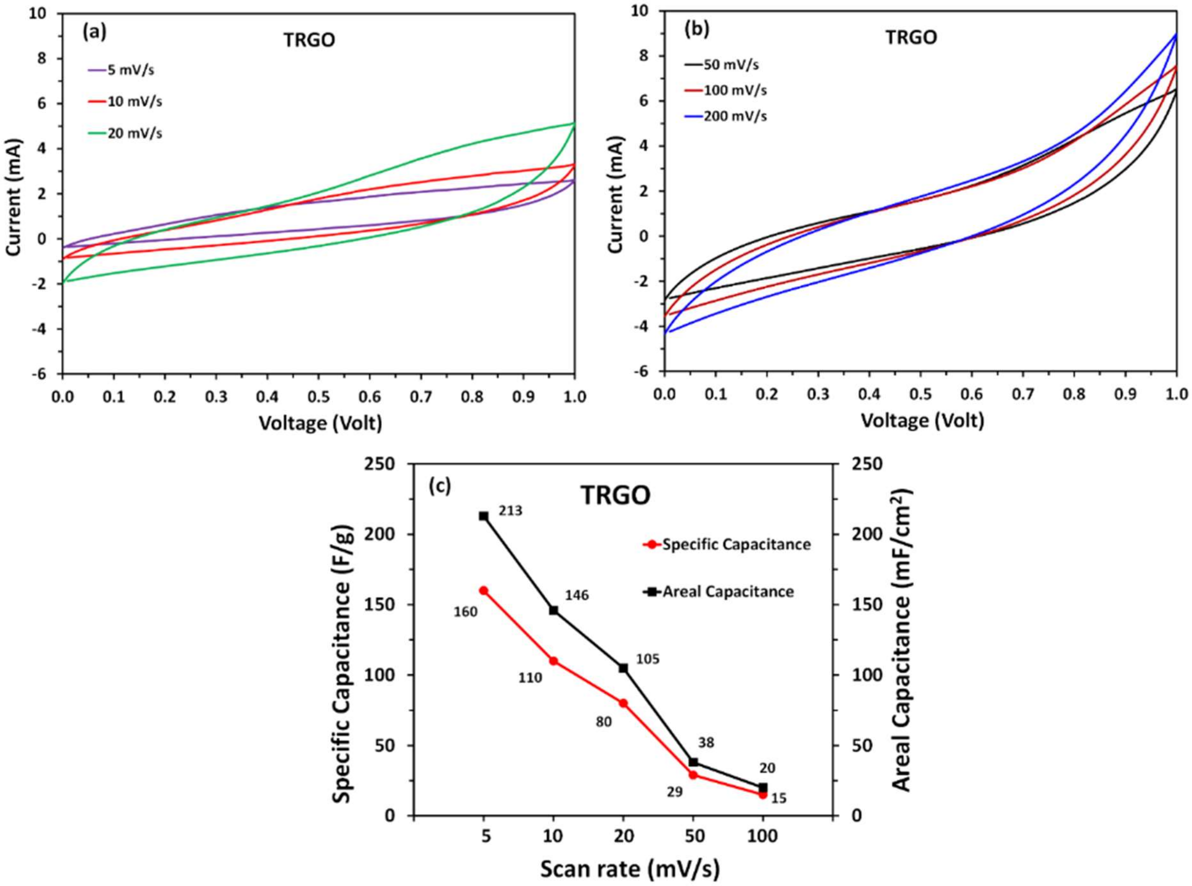

Figure 4.6. CV test results of the 3D-printed printed TRGO disks at a) low and b) high scan rates, c) specific and areal casacitance values of TRGO disks at different scan rates.

is among the high values reported so far [155], [179], [180]. Certainly, further investigation is required to improve the properties of the disks at high scan rates. It is noteworthy that the TRGO disks fabricated through powder-based AM technique were made of pure graphene material which can introduce a novel approach towards commercialization of additive manufacturing of graphene-based supercapacitor electrodes.

4.4 Conclusion

Herein, a facile binder jetting AM technique was introduced for the fabrication of graphene-based supercapacitor electrodes. As-obtained graphene oxide powder was reduced using chemical and thermal methods. Owing to intense restacking of graphene sheets after chemical reduction, graphene oxide dispersion was preloaded with PVA to provide spatial hindrance between the layers. Chemically reduced graphene oxide samples were first drop-cast to explore the capacitive performance of the electrodes. CRGO and CRGO4 samples showed higher Cs values and were used for the fabrication of electrode disks. TRGO powder was also printed to study the effect of reduction method on the performance of supercapacitor cells. Although the CRGO and CRGO4 had a promising performance as drop-cast electrodes, the printed disks using these samples exhibited inferior properties which could be attributed to their insufficient electrical conductivity. However, the Cs values of TRGO disks were considerably higher than the CRGO samples due to their anticipated higher electrical conductivity.

Chapter 5

Binder-jet powder-bed additive manufacturing (3D printing) of thick graphene-based electrodes

5.1 Introduction

Additive manufacturing (AM) has revolutionized the way in which we fabricate 3D structures[181]–[184]. To date, various 3D printing strategies have been demonstrated. For example, fused deposition modeling (FDM), stereolithography, selective laser sintering (SLS), microdeposition, and binder jetting are now being frequently adopted to print complex 3D shapes using various precursor materials [58]. All these methods have a feature in common, which is layer-by-layer manufacturing of the structure and binding the layers through either melting, photopolymerization, sintering, or injection of a binder. While AM was once only used for rapid prototyping, it is now becoming a commercial end-product fabrication platform with wide potential applications in automotive, aerospace, bio and particularly, energy-related areas [183]. In particular, AM has the potential to fabricate full energy storage systems such as batteries and supercapacitors using advanced materials such as graphene, carbon nanotubes, various metal oxides, and high performance polymers [185]–[197]. However, the printing of these materials, which are neither polymers nor metals, which are not easily melted or sintered makes 3D printing a much more challenging endeavor.

For example, graphene-based supercapacitor electrodes have been prepared through different methods such as inkjet printing [66], [115], [127], [189], [191], [193], [198]–[206]; however, evaporative drying of the solvent induces stresses in the film which causes film cracking and limits the technique to printing thin films [207]. While such thin films are sufficient for proof-of-concept demonstrations, commercial high energy density supercapacitors (and batteries) require electrodes to be 100-500 μm thick [208] – a regime currently out of reach for solvent-based printing methods. These thicker films are required to maintain a larger fraction of active material than current collector and separator in the cell to obtain the highest possible energy density for a packaged device [209].

There have been several recent reports describing the fabrication of thick graphene-based electrodes [49], [132], [180], [210]–[214]. Graphene foams, for instance, have been prepared using hydrothermal and self-assembly methods; however, these processes commonly require use of toxic reducing agents such as HI or hydrazine monohydrate followed by vacuum or freeze drying [215]–[218] which may lead to cracking [207]. Also, producing complex shapes with high dimensional accuracy is limited using hydrothermal process. Additive manufacturing can be considered as an outstanding solution for the challenges associated with the fabrication of thick graphene-based electrodes. García-Tuñon et al. [187] prepared a GO/BCS (Branched copolymer surfactant) suspension with tailored viscoelastic properties and used a robotic deposition device to produce graphene-based 3D structures of graphene. The structures were freeze dried and thermally reduced in a tube furnace. Wei et al. [195] developed different graphene-polymer based composite dispersions where were extruded using a similar technique reported previously. Kim et al. [185] also printed nanowires from colloidal dispersion of GO sheets using glass micropipettes based on capillary forces with subsequent reduction process through chemical or thermal treatment. However, the capacitance performance of these printed graphene-based structures was not reported.

To by-pass these problems, our group has recently demonstrated a technique called binder-jetting powder-bed AM which eliminates the use of a solvent all-together in order to build large, crack-free 3D structures such as porous bone-implants [59], [61], [62], [165], [167]. The technique relies on the use of precursors in the form of dry, micron-sized, flowable powders which are uniformly distributed as a layer and patterned with a binder which effectively glues adjacent layers together as the structure is build up layer-by-layer. This leads to complex 3D structures with an interconnected pore structure which facilitates material flow and is hypothesized to allow for rapid ion transport in to electrochemical devices such as supercapacitors.

In this paper, we demonstrate the application of binder-jetting powder bed AM to the fabrication of thick graphene-based 3D structures and demonstrate their use as electrodes in high performance supercapacitors. Using this approach we are able to directly use the high specific surface area powder generated during the rapid thermal expansion of graphite oxide. The wrinkles and folds between aggregated sheets of the thermally reduced graphene oxide (TRGO), that make up the powder, generated by the build-up of gases released during the rapid decomposition and reduction of graphite oxide help to prevent the sheets from restacking and help to maintain the high specific surface area. After evaporatively consolidating this material to create a higher bulk density powder, the TRGO was built up layer-by-layer using minimal binder into mm-sized electrodes with effectively any shape or form factor. Using the electrodes directly as supercapacitors resulted in capacitances as high as 260F/g and areal capacitances of 700 mF/cm2. However, to achieve the best results, a small amount of Pd nanoparticles (< 9 wt%) were added to the binder dispersion to improve the contact resistance between powder agglomerates. Thus improvements to the process which improve the bulk density and contact area between powder aggregates will be required in future studies of this promising approach to eliminate the need for such conductive additives.

5.2 Experimental

5.2.1 Synthesis and reduction of graphene oxide

Tour method was used to synthesize Graphene oxide (GO) [157]. Briefly, 9:1 ratio of sulfuric acid and phosphoric acid were mixed and subsequently, graphite (Graphite flake, -10 mesh, Alfa Aesar, MA) and KMnO4 (1:6 ratio) were added to the mixture. The mixture was stirred for 16 hours while heated to 45 °C. Next, the mixture was cooled in air to room temperature and then poured on ice very slowly to avoid overheating of the mixture. After stirring, 10 mL of 30% hydrogen peroxide was poured carefully to the mixture to stop reaction. The dispersion was washed with HCl and Ethanol by centrifuging and eventually stored in ethanol to avoid restacking of the GO sheets.

For thermal reduction, GO dispersed in ethanol was dried and collected. The powder was placed in a silica glass tube, which was next vacuumed and argon filled, repeatedly. Lindberg/Blue M™ Mini-Mite™ Tube Furnace was preheated to 1100 °C and then the glass tube was pushed into the furnace quickly and kept for 1 min. Through reduction, the GO agglomerated sheets converted to a fluffy dark powder, which was collected for further experiments. For further studies, TRGO sheets were characterized using SEM (Zeiss, LEO 1530 Gemini) and X-ray photoelectron spectroscopy (XPS), respectively.

5.2.2 Synthesis of palladium nanoparticle dispersion

5 mM sodium citrate (Sigma-Aldrich) and 0.025 mM tannic acid were dissolve in 100 mL of distilled water. The solution was heated to 70˚C while it was stirred gently by magnetic stirrer. Then, 8 mL of Pd2 (NO3)3 (25 mM) solution was injected into the sodium citrate/tannic acid solution. After injection, the reactor was kept at 70˚C for 15 min to complete the reaction.

5.2.3 Additive manufacturing of electrode disks

A retrofitted binder jetting additive manufacturing machine (3D Systems, Burlington, MA) was used to print the 3D structures of RGO. The system was retrofitted to take smaller amount of powder, inject customized binders and provide an open source code to tune process parameters (e.g., layer thickness, binder volume). In this process, CAD model (STL file) of the electrode disks (diameter: 12 mm, thickness: 300 μm) was prepared and then sliced to be used by the retrofitted machine. As reported elsewhere [61], [165]–[167], a layer-by-layer fashion fabrication process is conducted to build the 3D structure. Briefly, as illustrated in Schematic 1, there are two pistons, namely feed bed and build bed, with adjustable heights in the chamber of machine. The temperature in the chamber is commonly set to 35 °C. The raw powder is first added to the feed bed with an even top layer of powder to provide the material required for the fabrication of the disks. Next, using a micro motion controller, the piston is translated upward according to the pre-adjusted layer thickness (for this study 100 μm) raising one layer of powder on top of the whole substrate. Then, a rotating roller moves pushing the exposed layer of powder forward to cover the build bed. The print head is subsequently directed to the top of the build bed to inject an aqueous-based binder (zb®60 binder clear, 3D Systems, Burlington, MA) to the first layer of powder based on the geometry of the first slice of the CAD model. According to MSDS, the binder consists of >90% water, 8% glycerol and 2% other humectants. The system injects the binder with 8-bit greyscale color-map distribution at 360 dpi, with 7 drop sizes in the range of 6 to 42 pL. The shell to core binder concentration ratio was 100:200% for the manufacturing of RGO disks. This process is iterated until the final structure is fabricated. For SEM characterization, one of the 3D printed disks was cut from the center line and examined from the top and cross section of the structure. Thermally reduced graphene oxide powder (TRGO) was used as-received and no other additive was added before printing. However, the as-received TRGO powder is fluffy with poor flowability. In order to increase flowability, the TRGO powder was dispersed in acetone and dried in air overnight. The collected powder was used in the retrofitted machine.

5.2.4 Post AM processing

After the AM process, the disks were placed on an aluminum mesh and 150 µL of palladium nanoparticle dispersion was subsequently added to the disks. The weight fraction of palladium nanoparticles in the disks was 1 % (TRGO1), 3% (TRGO3), and 9% (TRGO9), respectively. As a control, TRGO disks were also impregnated by 150 µL of DI water free of palladium nanoparticles after printing.

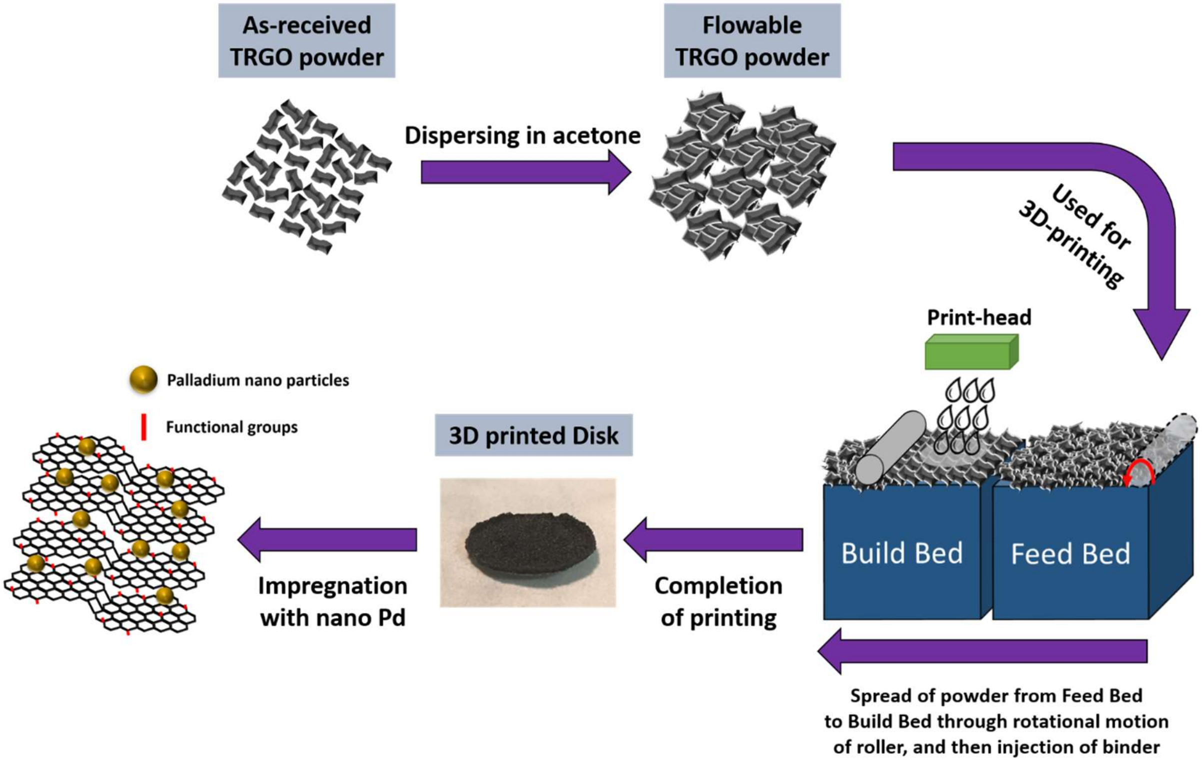

Schematic 1. Schematic presentation of the binder-jetting powder-bed AM technique. The powder is first spread into the feed bed. Through the upward movement of the feed bed piston, a layer of powder is raised and then the rotating roller pushes the powder forward to spread it on the build bed. The print head injects an aqueous-based binder to bond the particles forming the shape of the first slice of the object. The process is iterated until the 3D-structure is fabricated.

5.2.5 Cell assembly and electrochemical measurement

The as-prepared electrodes were assembled into a symmetrical two-electrode configuration using Swagelok cells. To prepare the cell, each electrode was placed onto a stainless steel bar followed by addition of three drops of 1M H2SO4 as the aqueous electrolyte. Nitrocellulose filter paper, which was soaked in the electrolyte overnight was placed between the electrodes before swaging the cells. Additionally, for comparison, the same mass of TRGO material in the 3D-printed disks (1.5 mg) was mechanically compacted on the SS bars and assembled in a cell according the same procedure explained above. The cyclic voltammetry (CV) test was conducted using a computer controlled potentiostat/galvanostat (Invium, Pocketstat) at scan rates between 5 mV/s and 200 mV/s. The specific capacitance is calculated according to equation 1:

$$C = 2\,(i)/(m.\Delta V/\Delta t) \quad (1)$$

where i is the average of the anodic and cathodic current at half of the potential limit, $\Delta V/\Delta t$ scan rate, and m mass of one electrode. For the areal capacitance, the geometric area of one electrode is used in the equation instead of mass. Electrochemical impedance spectroscopy (EIS) was also measured within a frequency range of 100 kHz to 0.1 Hz.

5.3 Results and discussion

Figure 5.1a shows SEM images of the synthesized palladium nanoparticles. The inset of Figure 5.1a confirms that the synthesized palladium nanoparticles are spherical with diameter around 20 nm. The UV/vis spectra of the synthesized solution is also demonstrated in the second inset of Figure 5.1a. It reveals one peak in the absorbance intensity with a maximum at 396.2 nm. This is indicative of surface plasmon resonance (SPR) associated with Pd nanoparticles [219], [220]. The presence of one relatively narrow peak confirms that the nanoparticles have a uniform size distribution. This result is in agreement with SEM image of Figure 5.1a.

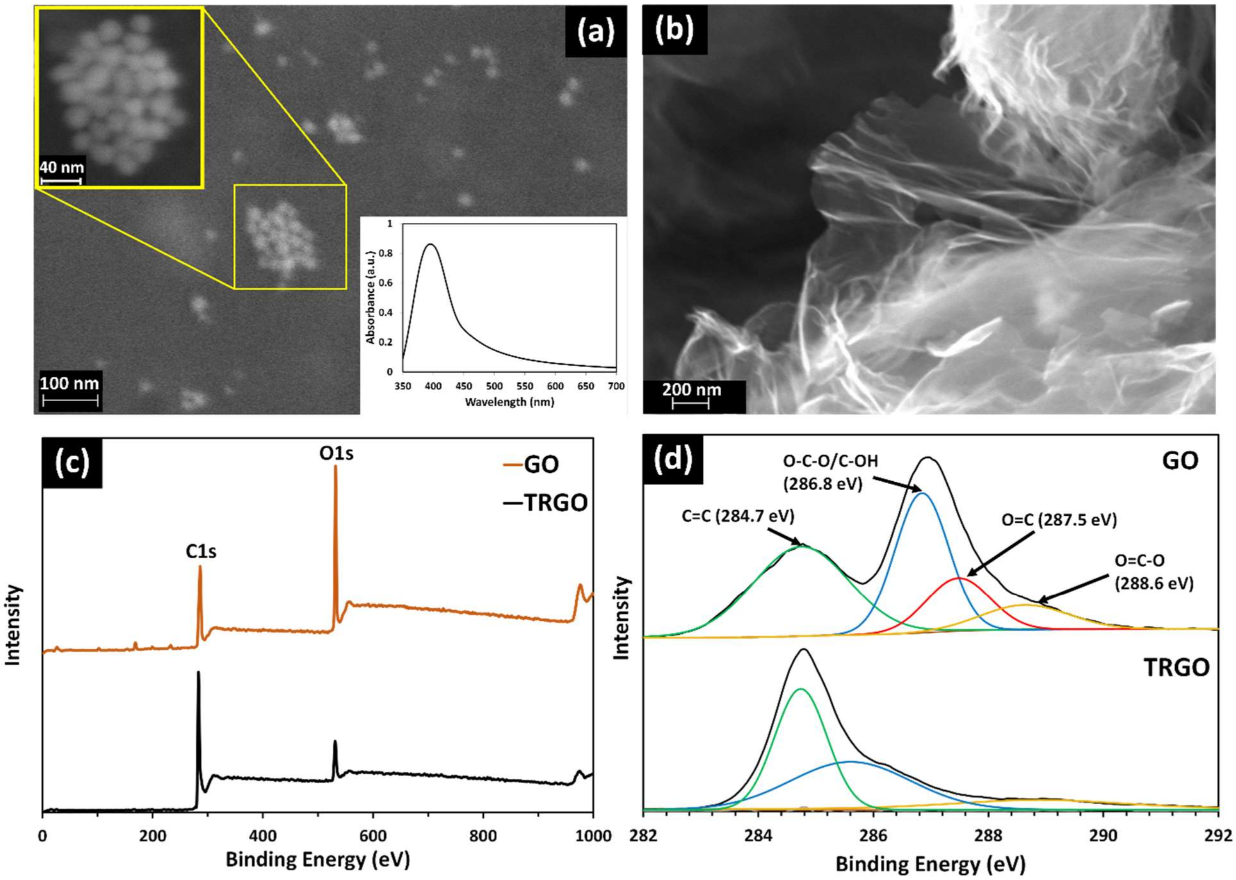

Figure 5.1. a) SEM image of as-synthesized palladium nanoparticles; the inset on the top left corner shows the rounded palladium nanoparticles, the inset on the bottom right corner shows the UV/vis spectra of the palladium nanoparticle dispersion, b) SEM image of as-synthesized TRGO sheets, c) XPS scan survey, and d) C1s spectra of GO and TRGO.

Figure 5.1b shows an SEM image of the synthesized RGO powder. The XPS spectra of GO and TRGO are also compared in Figure 5.1c and d. These confirm that prior to the thermal expansion process, the graphite was sufficiently oxidized to a C/O ~ 1.6 with oxygen functional groups present such as carboxyl, epoxy, carbonyl, and hydroxyl groups as has been shown previously [199], [221]. Upon thermal reduction, the C/O ratio increased from 1.6 to 6.7 in the TRGO as oxygen containing functional groups decompose as H2O, CO and CO2 [222]. The removal of carbon from the lattice is known to introduce a significant fraction of lattice defects in the material. However, these defects and remaining functional groups are known to increase both the double-layer capacitance [48] and pseudocapacitance contributions [177] in graphene-based supercapacitors.

As shown in Figure 5.2, immediately after rapid thermal expansion process, the TRGO powder has an extremely low bulk density (~10^{-2} g/cm^3) [13] and is too fluffy/lightweight to be used directly in the AM process. To densify this material, the powder was mixed with acetone and evaporatively dried. The resulting material with increased bulk density was pulverized and used as the precursor for AM. Figure 5.2 illustrates how the binder-jetting AM technique is able to print complex 3D shapes ("U" an "W") from the resulting TRGO powders. Once the printing is completed, the structures can be collected from the build bed through a depowdering process as shown in the Figure 5.2. Although the dimensional resolution of these structures is limited by the penetration of injected binder to adjacent powders to ~ 500 μm, there is no limitation in the complexity of shapes which can be printed using this technique.

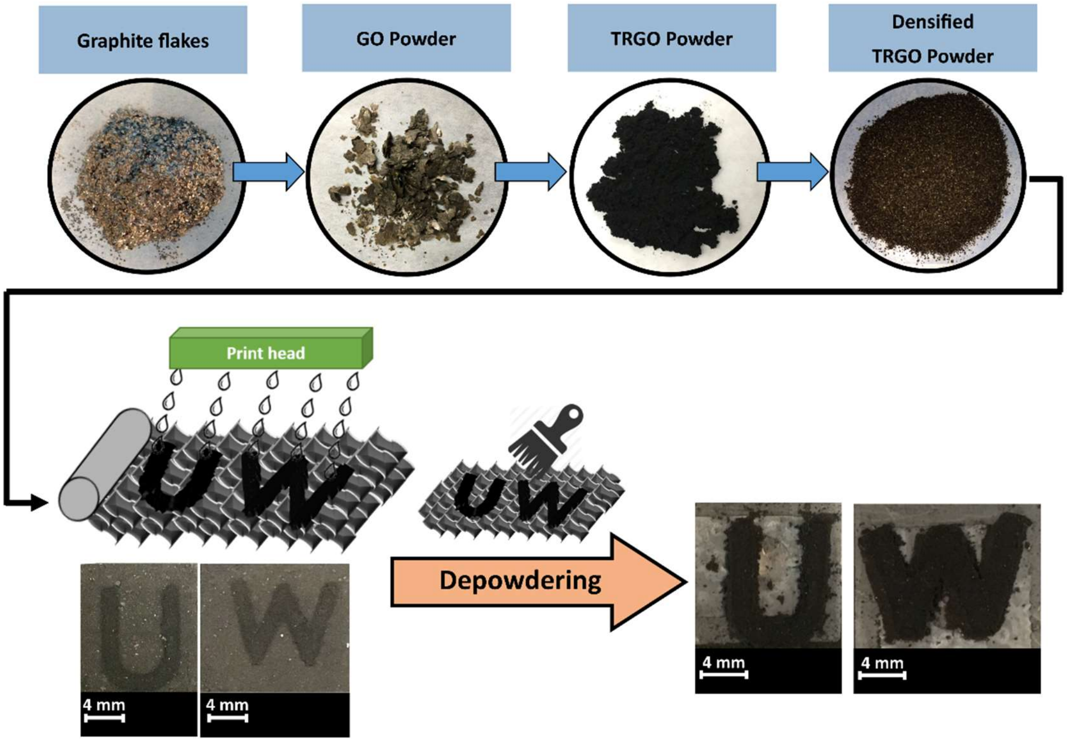

Figure 5.2. Printing of complex shapes using powder-bed AM technique, a) and b) after printing, c) and d) after depowdering.

Figure 5.3 displays the SEM images of the AM-made and electrodes pelletized with the same mass of TRGO using a hydraulic press. SEM images of the top and cross sections of the electrodes are shown in Figure 5.3a and Figure 5.3b and demonstrate the microstructure of TRGO compacted disks compared to 3D printed disks. Compacted disks show agglomerates of TRGO sheets larger than 20 µm whereas TRGO9 disks display a corrugated pattern of TRGO sheets with interconnected pores (see Figure 5.3c) decreases the path length for ion migration/diffusion. Figure 5.3e shows a cross-sectional view of the AM-made TRGO disks with a corrugated pattern similar to the top view of the disks. This pattern was not observed in the electrodes prepared by the conventional pelletizing/molding of TRGO powder.

The resulting printed disks have a low bulk density (0.044 g/cm3) which limits the contact area between the graphene sheets and subsequently, conductivity of the disks. Additionally, the large thickness (> 300 µm) of the 3D-printed structures resulted in a high electrical resistance. Therefore, to improve the performance of the electrodes, we studied the impact of impregnating discs with aqueous dispersions of palladium nanoparticles at different concentrations. Incorporation of noble metals onto graphene-based materials is a common practice to improve the electrical and catalytic properties of the graphene-based [223]–[225]. However, complicated methods including solvothermal and chemical precipitation are commonly used to decorate the graphene sheets. Herein, we simply added 150 µL the colloidal palladium nanoparticle solution to the disks using a micropipette to decorate the RGO layers. Due to the presence of interconnected pores in the microstructure, the drops were immediately adsorbed by the disks through capillary forces. Figure 5.3d and Figure 5.3f display the top and cross-sectional views, respectively of TRGO9 samples that contain the largest amount of palladium (~9 wt%). It is clearly seen that the surface of the TRGO sheets is perfectly decorated with palladium nanoparticles/clusters uniformly distributed between the layers (see the similar decoration of palladium nanoparticles both in top and cross section views in Figure 5.3d and Figure 5.3f). The red arrows in Figure 5.3d and Figure 5.3f show the distribution of nanoparticles on the TRGO sheets which we believe is through physical adsorption and are expected to bridge between RGO sheet aggregates to reduce the contact resistance [226], [227].

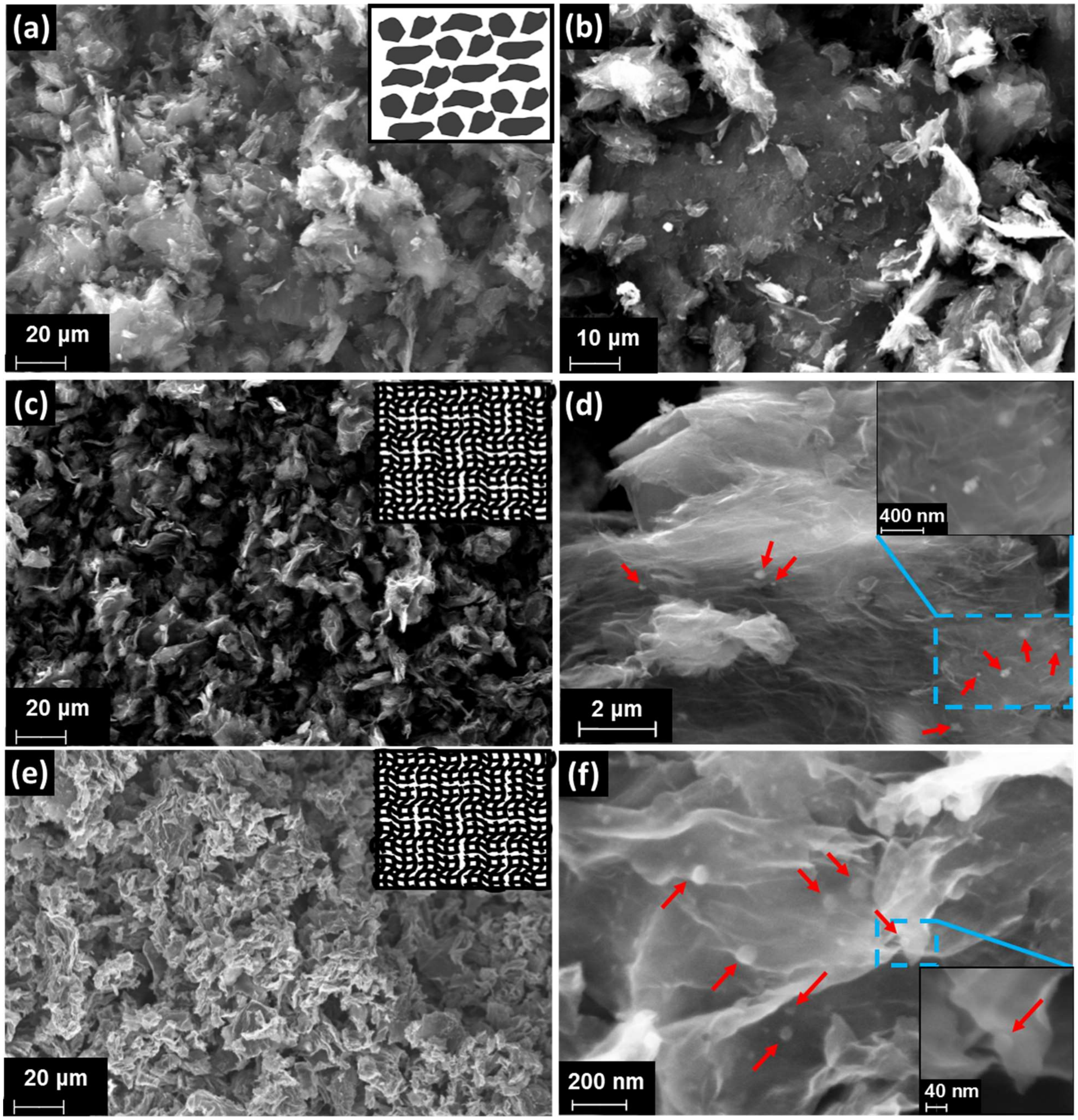

Figure 5.3. Secondary electron SEM images of a) and b) top view of the compacted TRGO disk (inset is the schematic of the microstructure), c) top view of the 3D printed TRGO9 disk (inset is the schematic of the microstructure), d) top view of the 3D printed TRGO9 disk with higher magnification, e) cross section view of the sliced TRGO9 disk, and f) cross section view of the sliced TRGO9 disk with higher magnification, the inset in a), c), and e) is the schematic of the microstructure, respectively, and the red arrows in Figures b), d), and f) point to some of the palladium nanoparticles decorating the surface of the TRGO sheets.

During the AM of the disks, a binder is injected to bond the particles in the build bed. As discussed earlier, more than 90% of binder consist of water, TGA was used to determine the weight of active material and the binder residue after printing. Figure 5.4 shows the TGA curves of the TRGO 3D printed sample, as-received TRGO powder, and the difference in TGA signal between the as-produced TRGO powder and the as-printed TRGO powder with the binder, respectively. It is clear that beyond 150 °C, the weight difference drops to less than 0.5 wt. %, which proves the negligible binder residue in the samples after printing. A significant portion of the weight loss up to 150 °C is attributed to the evaporation of adsorbed water from the binder to printed samples.

The CV profiles of the various electrodes made using the AM approach containing varying amounts of palladium nanoparticles were tested from low to high scan rates (5mV/s-500 mV/s) and are shown in Figure 5.5. All curves exhibit a nearly rectangular shape, with no largely apparent redox peaks associated with pseudocapacitance. However since we are using an aqueous electrolyte, pseudocapacitance distributed over the 1V potential range, arising from residual functional groups and defects could also be contributing to the observed capacitance [48]. The results show that raising the concentration of palladium nanoparticles from 0% to 9% in TRGO to TRGO9 results in increased current density as well as making the CVs more rectangular. This change in shape is associated with less resistance in the electrodes as suggested by Frackowiak and Beguin [109]. In comparison, the capacitive performance of TRGO9 electrodes is superior to their TRGO counterparts, which could be attributed to the reduced contact resistance affected by the palladium nanoparticles. This effect is more pronounced at higher scan rates such as 200 or 500 mV/s.

Figure 5.6 compares the specific capacitance and areal capacitance of all disks produced. The specific capacitance of the neat TRGO electrodes at 5 mV/s is 160 F/g whereas palladium decorated electrodes (TRGO9) show a capacitance of more than 265 F/g.

Although the capacitance drops at higher scan rates, a four-fold increase is observed at the scan rate of 200 mV/s between TRGO (9 F/g) and TRGO9 (34 F/g) electrodes. The areal capacitance obtained from TRGO9 electrodes is above 700 mF/cm2 at 5 mV/s (Figure 5.6), which exceeds most of the reported values for graphene-based electrodes which are typically of the thin film variety [212].

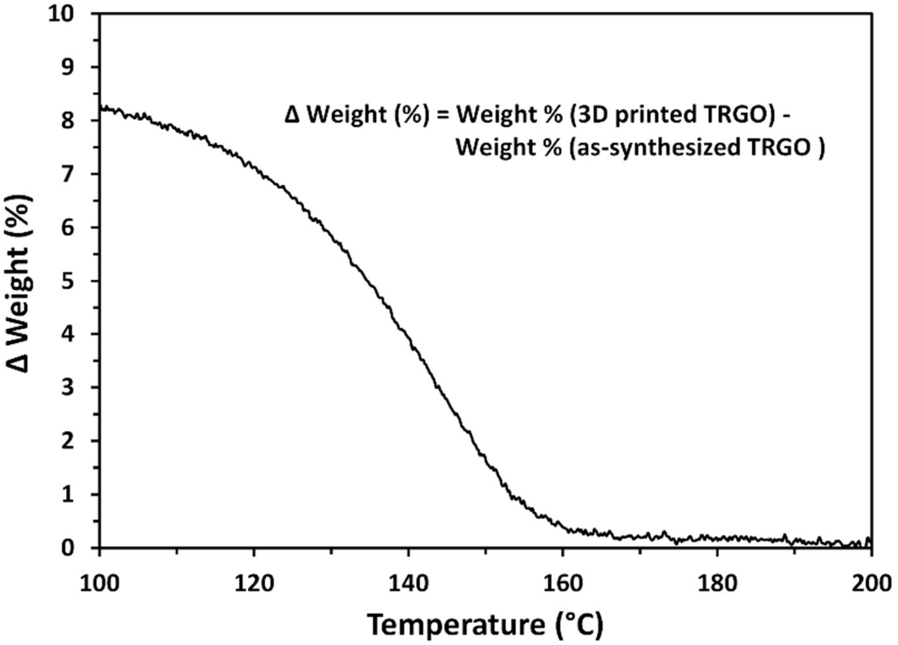

Figure 5.4. TGA curves of a) as-synthesized TRGO powder, b) 3D printed TRGO, and c) weight difference between as-received and as-printed TRGO powder based on TGA test results (heating rate: 10 °C/min).

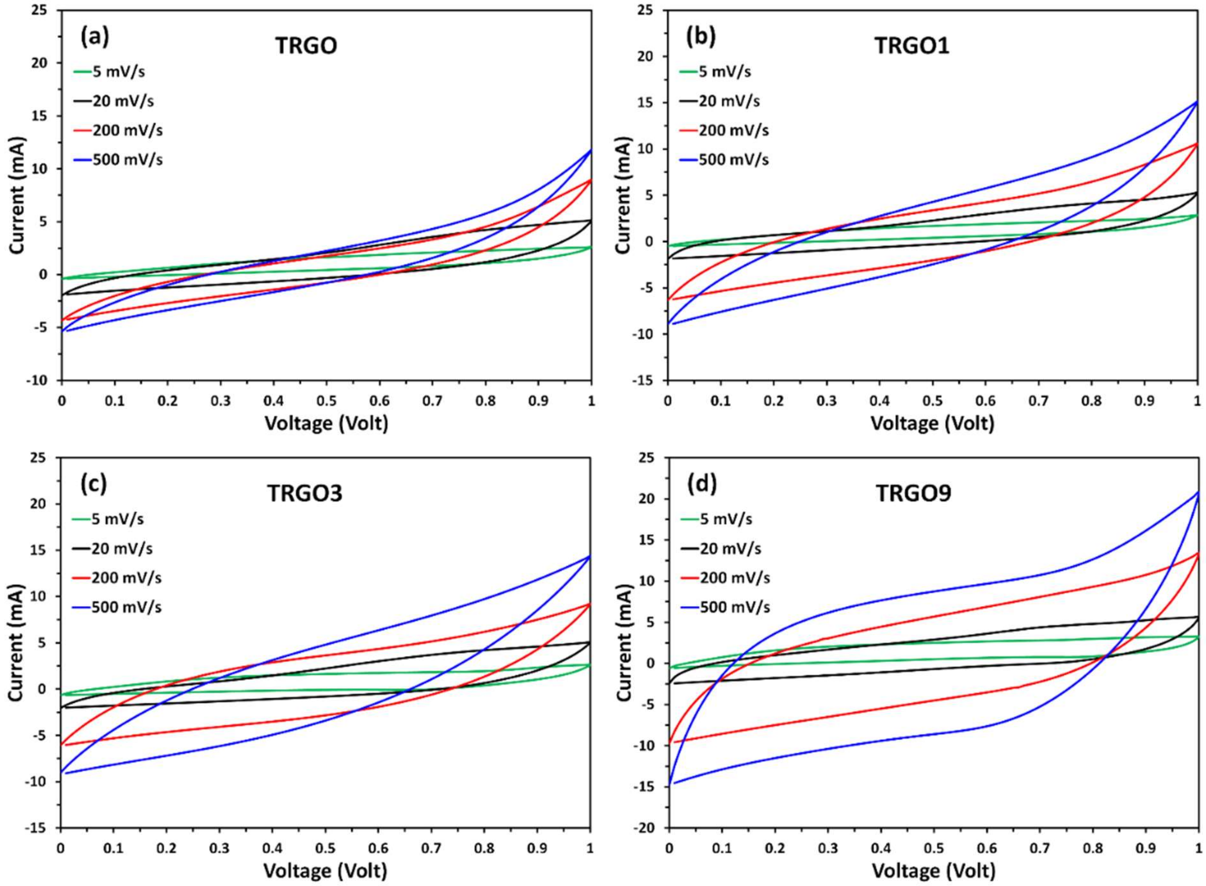

Figure 5.5. Cyclic voltammetry curves of 3D printed a) TRGO, b)TRGO1, c) TRGO3, and d) TRGO9 at the scan rates of 5mV/s, 20 mV/s, 200 mV/s, 500 mV/s.

Nevertheless, the downfall of the current approach is the low density of our powder which results in poor volumetric capacitance. We are currently optimizing our AM process and also producing powder precursors with higher bulk density in order to increase the packing factor of our 3D printed electrodes.

Galvanostatic charge/discharge testing results are also shown in Figure 5.7a. The specific capacitance obtained through the discharge curve is similar to that obtained by CV; however, at voltages close to 1 volt, the curves tend to form a plateau, particularly at the current density of 5 A.g-1 which is indicative of a parasitic reaction occurring.

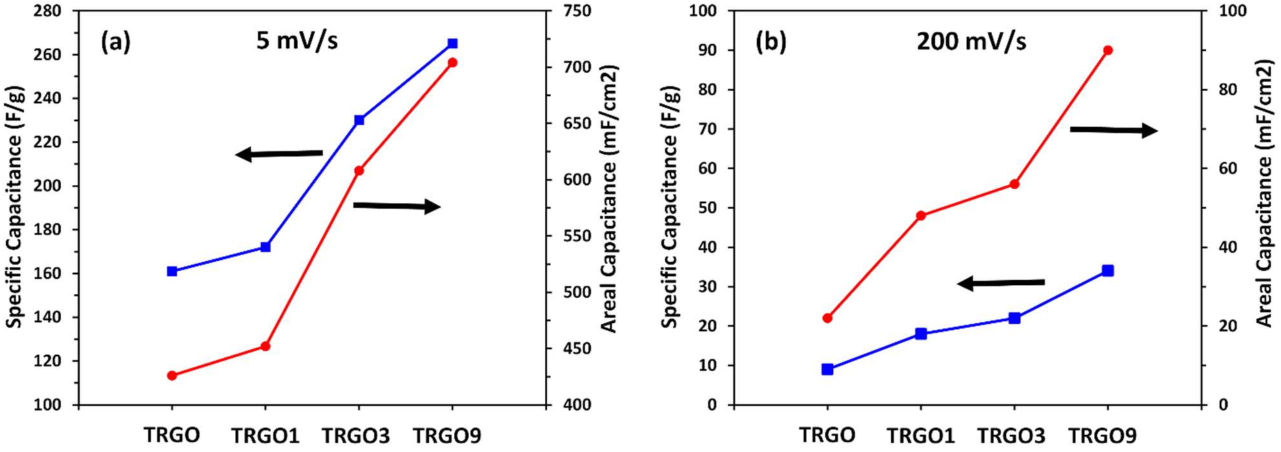

Figure 5.6. Specific capacitance and areal capacitance of TRGO, TRGO1, TRGO3, and TRGO9 at a) 5mV/s, and b) 200 mV/s.

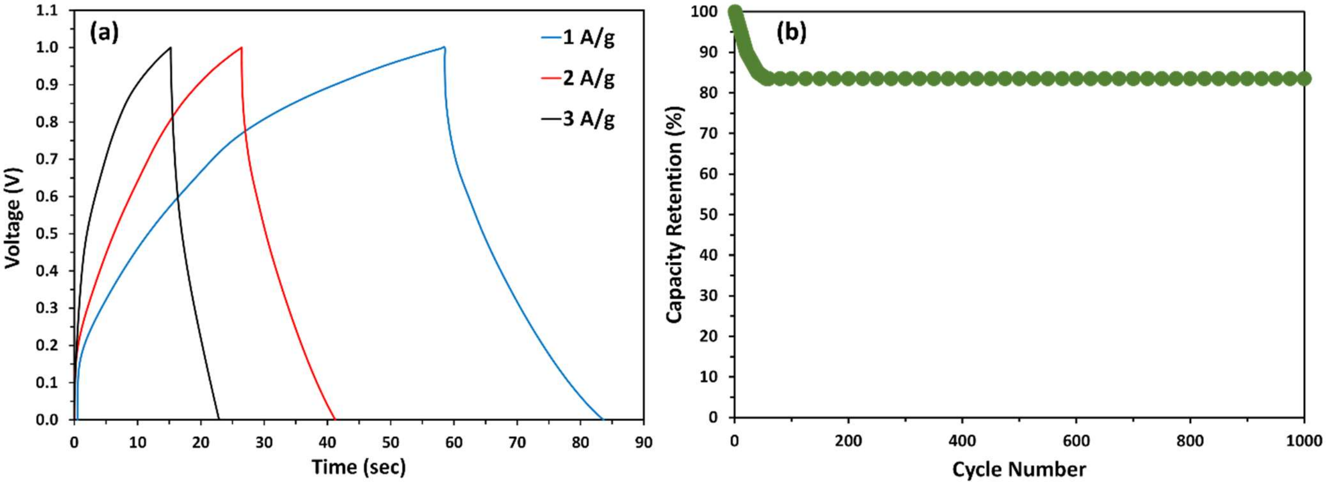

Figure 5.7. Galvanostatic charge/discharge curves of TRGO9 at the current density of 1 A g-1, 2 A.g-1, and 3 A.g-1, respectively, b) cyclic life of TRGO9 electrodes at 3A g-1.

We observed a noticeable corrosion of the aluminum current collector used. To ensure our capacitance was not impacted by this corrosion, we gold coated the aluminum which yielded similar results but was found to significantly improve our cycle-stability. As shown in Figure 5.7(b) our cells retain about 85% at 3 A.g-1 after 1000 cycles with the drop likely being due to current collector corrosion.

The EIS of the cells with TRGO9 electrodes is illustrated in Figure 5.8. The first and second intercept of the semicircle in Nyquist plot with the real axis (x-axis) in Figure 8a represent the resistance of the electrolyte (~ 0.5 Ω) and the internal resistance of the electrode (~ 1.5 Ω), respectively [228]. The diameter of the semicircle also reveals the equivalent series resistance (ESR) of the cell to be ~ 1 Ω. In the mid-frequency region after the semi-circle, the curve shows a 45° angle, representing the response of ion diffusion in the interfacial region of porous carbonaceous electrodes and the electrolyte as a function of frequency, namely a Warburg-like resistance[202].

The relatively short 45° line indicates a low variation in the ion diffusion path from the electrolyte to the electrode, which is expected in the porous electrodes. In addition, the

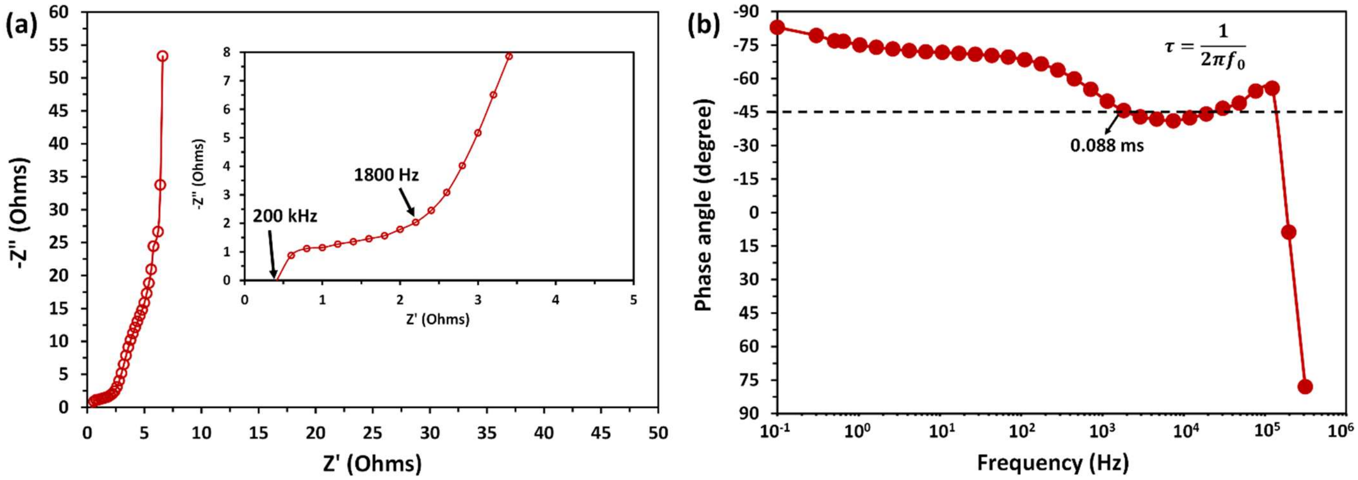

Figure 5.8. a) Nyquist plot of TRGO9 electrodes indicating imaginary part (-Z") versus real part (Z') of the impedance. Inset shows the high frequency region of the plot. b) Impedance phase angle versus frequency of TRGO9 electrodes.

nearly vertical rise observed in the low frequency region suggests are electrodes approach the behavior of ideal capacitors in this region [49], [51], [83], [156].

Figure 5.8b displays the Bode plot as the phase angle of TRGO9 samples versus frequency. At low frequencies up to 100 Hz, the phase angle is very close to -90°, which can be attributed to a nearly ideal capacitive behavior. The relaxation time or time constant ($\tau = RC = \frac{1}{2\pi f_0}$), which is usually calculated at -45° defines the rate of adsorption and diffusion of ions at the electrode interface. For TRGO9 samples, this occurs at a high frequency of almost 1000 Hz, the time constant achieved in this sample is 0.088 ms, which is significantly lower than all other values reported to date [179], [191], [192], [201], [229]. This very low time constant can be attributed to the interconnected pores in the electrodes facilitating the ion transport and efficient formation of EDL at the interface of TRGO sheets.

Table 5.1 compares the capacitance of graphene based electrodes fabricated through various techniques and tested in a two-electrode configuration. It is seen that the gravimetric capacitance of the AM-made electrodes is amongst the highest values reported to date. With future improvements to the bulk density of the powders used in this process, this AM technique provides a relatively simple and scalable method for advanced manufacturing.

Table 5.1. Review of gravimetric capacitance of graphene based supercapacitors tested in two electrode configuration

Fabrication technique	Electrode material	Electrolyte	Capacitance (F g-1)	Ref.
Additive manufacturing	TRGO>90%, Palladium nanoparticles	1 M H_2SO_4	265	Current work
Hydrothermal process	N-doped graphene hydrogel	5 M KOH	190	[230]
In Situ self-assembly	Graphene hydrogel	5 M KOH	156	[215]
Hydrothermal process	Graphene hydrogel	5 M KOH	220	[216]
Hydrothermal process	Graphene hydrogel	5 M KOH	175	[130]
Evaporation-induced drying	Graphene hydrogel	6 M KOH	235	[217]
Hydrothermal and freeze-drying process	Nitrogen and boron co-doped monolithic graphene aerogels	1 M H_2SO_4	239	[56]
Hydrothermal process	Graphene hydrogel	H_2SO_4-PVA gel	196	[180]
Aerosol spray pyrolysis	Crumpled graphene	1 M H_2SO_4	150	[49]

5.4 Conclusion

Thick graphene-based electrodes, which were fabricated using powder-bed additive manufacturing technique (layer thickness: 100 µm, binder saturation ratio: 100/200% for the first time, showed promising results as a full-size device with high gravimetric and areal capacitance values of 260 F/g and 700 mF/cm2, respectively. The microstructure of the electrodes, developed through AM, had a corrugated pattern of TRGO sheets, which should enhance the effective surface area of the electrodes and increase the double layer capacitance of the device. The interconnected pore structure facilitates the decoration of TRGO sheets with palladium nanoparticles to decrease the contact resistance and improve the charge transfer. It was shown that decoration of TRGO sheets with palladium nanoparticles increases the gravimetric and areal capacitance values by a factor of two and seven, respectively. The electrochemical impedance spectroscopy also proved a low contact resistance and high rate of ion transport in the TRGO9 electrodes.

Chapter 6

Additive manufacturing of graphene-based humidity sensor device

6.1 Introduction

Nowadays, smart devices are used widely in everyday lives. Sensors are an inseparable part of these devices, particularly for environmental monitoring. Graphene-based materials are very attractive candidates as chemical/humidity sensors owing to their high specific surface area, remarkable electrical properties, relatively easy chemical tenability, and low temperature catalytic properties [1], [2]. However, the manufacture of accurate graphene-based sensor devices is still an ongoing research. Duy et al. used a chemical approach including etching and self-assembly to develop an RGO/ bromophenol blue dual mode gas/pH sensor as a flexible transparent device [1]. Zhang et al. employed a nano self-assembly method to manufacture an RGO/poly(diallylimethyammonium chloride) (PDDA) based film humidity sensor tested at the range of 11–97% relative humidity (RH) with the normalized response or sensitivity of 8.69–37.43% [3]. Su et al. fabricated a flexible humidity sensor on a PET substrate by dip-coating an Au-based interdigitated pattern into a GO solution with subsequent reduction through a number of chemical processes. The sensitivity obtained at the working range of 30-90% was 0.0423 log Z/%RH [4].

Most of these reports involve multiple chemical steps for fabrication. Herein, we report a facile method for the fabrication of the graphene-based sensors using additive manufacturing technique. In this method, the as-received thermally reduced graphene oxide powder (TRGO) was fed into the binder-jet powder-bed retrofitted additive manufacturing machine to fabricate a graphene-based porous 3D-structure as the sensing part of the sensor. A silicone-based hollow cube was also made using nozzle dispensing additive manufacturing technique as a place holder for the printed graphene-based structure. The fabrication process does not involve any chemical processes, thus offering a high potential for scaling and volume production. The sensor was tested in a wide range of relative humidity at different temperatures with promising results.

6.2 Experimental and fabrication technique

A nozzle dispensing additive manufacturing machine was used to print a hollow cube from silicone as a housing for the graphene-based cube. The part was printed by deposition of polysiloxane from a syringe using a pneumatic micro-syringe deposition system (UltimusTM V high precision dispenser, Nordson Corporation, OH, USA) [6]. Figure 6.1 shows the dispensing system during the printing of polysiloxane. Two copper substrates with two conductive wires were placed inside the cube at two sides to evaluate the performance of the sensor.

Graphene oxide (GO) was synthesized through Tour’s method as reported elsewhere [5]. The GO was dried after washing and thermally reduced in a Lindberg/Blue M™ Mini-Mite™ tube furnace at 1100 °C for 60 seconds. The TRGO powder was then fed to the powder-bed retrofitted additive manufacturing machine for printing. A cube of 20*15*5 mm was 3D printed and placed into the polysiloxane cube on top of the copper substrates at two ends to measure resistance. The schematic of the system is shown in Schematic 6.1. After placing in the polysiloxane cube, TRGO-based 3D structure was

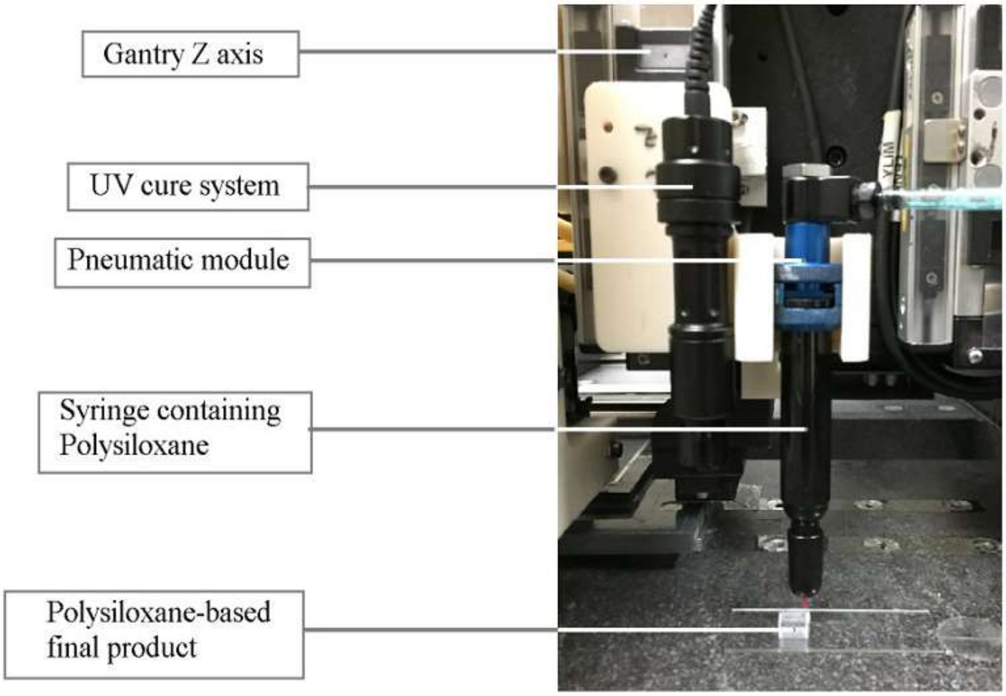

Figure 6.1. Pneumatic micro-syringe deposition system during printing polysiloxane [6].

impregnated with 500 μL of aqueous PVA solution (10 wt.%) to improve the mechanical strength of the porous structure.

The sensor device was placed in a dessicator and multiple reagents including lithium bromide, lithium chloride, potassium acetate, magnesium chloride, potassium carbonate, sodium bromide, potassium iodide, sodium chloride, potassium chloride, and potassium sulfate were used to create relative humidity (RH) of 6.4±0.6%, 11.3±0.3%, 22.5±0.4%, 32.8±0.2%, 43.3±0.4%, 57.6±0.4%, 68.9±0.3%, 75.3±0.2%, 84.2±0.3%, 97.3±0.5, respectively at 25 °C according to ASTM standard E104 − 02 (2012). The reagents were placed in the small chamber for minimum of 5 hours to reach the saturation level.

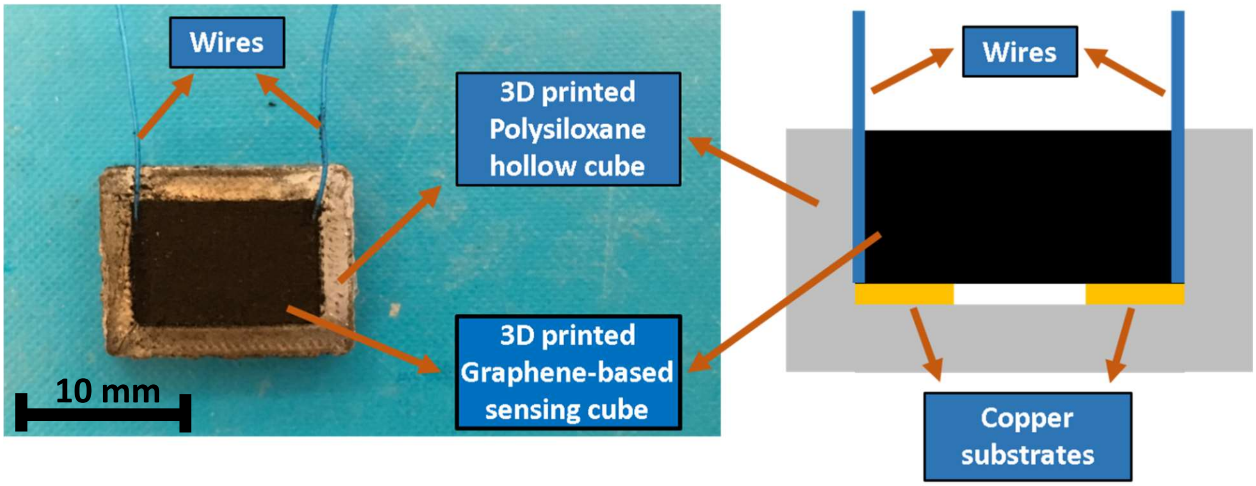

Schematic 6.1. A picture of the 3D printed sensor device with a schematic of a cross section view of the device.

The performance of the sensor was defined as sensitivity, determined by S $= \frac{R_0 - R}{R_0} \times 100$ where R_0 is the resistance of the sensor in dry air at 25 °C and R is the resistance measured in the given RH. Sensitivity was measured and reported as an average of 10 data points at different RH (%). In order to study the stability of the sensor versus temperature, sodium bromide was used as a reference for RH at different temperatures from 25 to 80 °C and the sensitivity values were compared with the reference RH according to ASTM standard E104 – 02 (2012) [231].

6.3 Results and discussion

Figure 6.2 displays the sensitivity of our sensor device to RH at different concentrations in the range of 6.4-97.3% of RH. The curve shows a remarkably linear response to a wide range of RH with a linear regression (R-squared value) of 0.996 of the fitting curve, represented by y = 0.6029x -0.5924 where y and x denote sensitivity and RH, respectively.

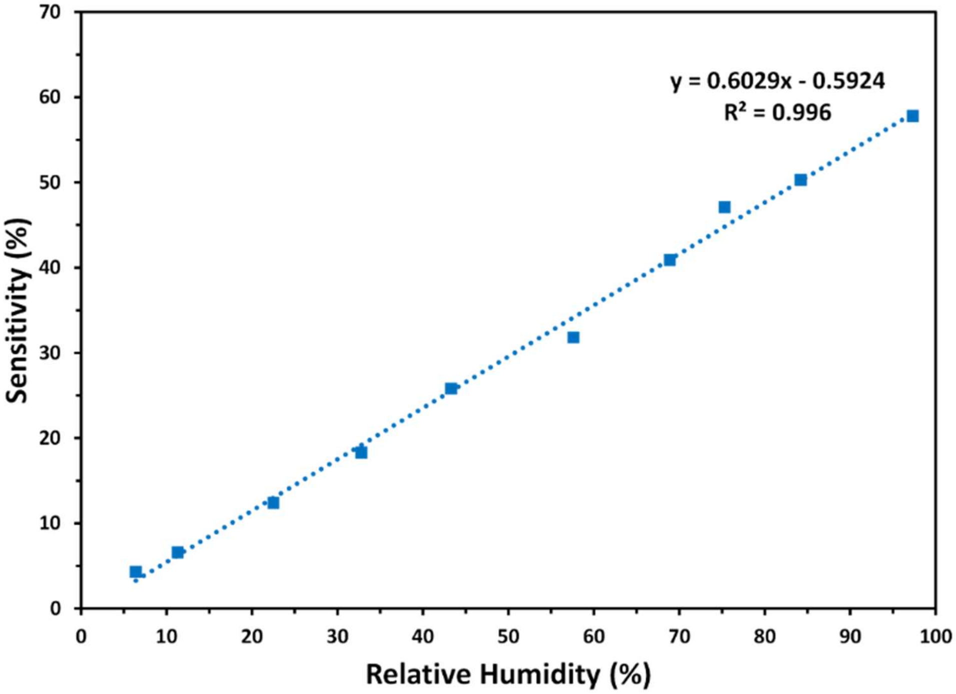

Figure 6.2 Calibration curve of 3D-printed TRGO-based humidity sensor device. Sensitivity (%) is defined as $\frac{R_0-R}{R_0}\times 100$.

Table 6.1. Comparison between graphene-based humidity sensors reported in the literature and the present work

Sensor type	Sensing material	Fabrication method	Working range (% RH)	Sensitivity	Reference
Resistive	TRGO	Additive Manufacturing (3D-printing)	6.4-97.3	4.3-57.8 (0.603 S/%RH)	This work
Resistive	PDDA/RGO	LBL self-assembly	11-97	8.69-37.43	[232]
Capacitive	Graphene oxide	Solution dripping	25-65	-9.5 fF/%RH	[233]
Stress-type	Graphene oxide-silicon bi-layer	Spin-coating	10-98	79.3 µV/%RH	[234]
Conductive	Defect graphene	Solvothermal	3-30	0.27-3.33%	[235]
Impedance	Partially reduced GO	LBL-anchored	30-90	0.0423 log Z/%RH	[66]
Surface acoustic wave	Graphene oxide	atomization	8-18%	1.54 kHz/%RH	[236]
QCM	Graphene oxide	Spin-coating	6.4-93.5	22.1 Hz/%RH	[237]
Impedance	Reduced GO	TBLI	10-90	6.3 Z/%RH	[238]

It is clear that the resistance of the sensor is decreased by raising RH significantly and the sensitivity is increased from 4.3% at RH of 6.4% to 57.8% at RH of 97.3%. As outlined in Table 6.1, the sensor was tested in a wide range of RH with an exceptional linear response compared to other studies. The lower resistance of the 3D printed TRGO based sensor at higher RH can be attributed to the adsorption of water molecules to the hydrophilic functional groups and bridging between the graphene sheets [232], [239]. This phenomenon can reduce the contact resistance between the sheets through formation of hydronium ions (H_3O^+) as charge carriers. Higher RH can trigger Grotthuss chain reaction ($H_2O + H_3O^+ \rightarrow H_3O^+ + H_2O$) [222]. High concentration of functional groups on adjacent graphene sheets can promote proton migration which can potentially contribute to reduced contact resistance at lower RH values. However, more studies are required to verify the proposed mechanism.

The sensitivity of the sensor was also tested at different temperatures to investigate the effect of temperature variations on the humidity sensing performance of the device. Lithium bromide was used as the saturated aqueous salt solutions in our test chamber to create equilibrium relative humidity values of 6.5%-5.2% in the temperature range of 25-80 °C according to ASTM standard E104 − 02 (2012) [231]. Figure 6.3 displays the stability of our 3D-printed TRGO based sensor device in the range of 25-80 °C. The sensitivity of the sensor at different temperatures corresponds to the expected RH values and according to Figure 6.3, it is not affected by temperature variations.

Figure 6.4 displays the response and recovery time of our TRGO-based 3D-printed sensor device at RH of 58%. For this test, sodium bromide was used in the chamber to create RH

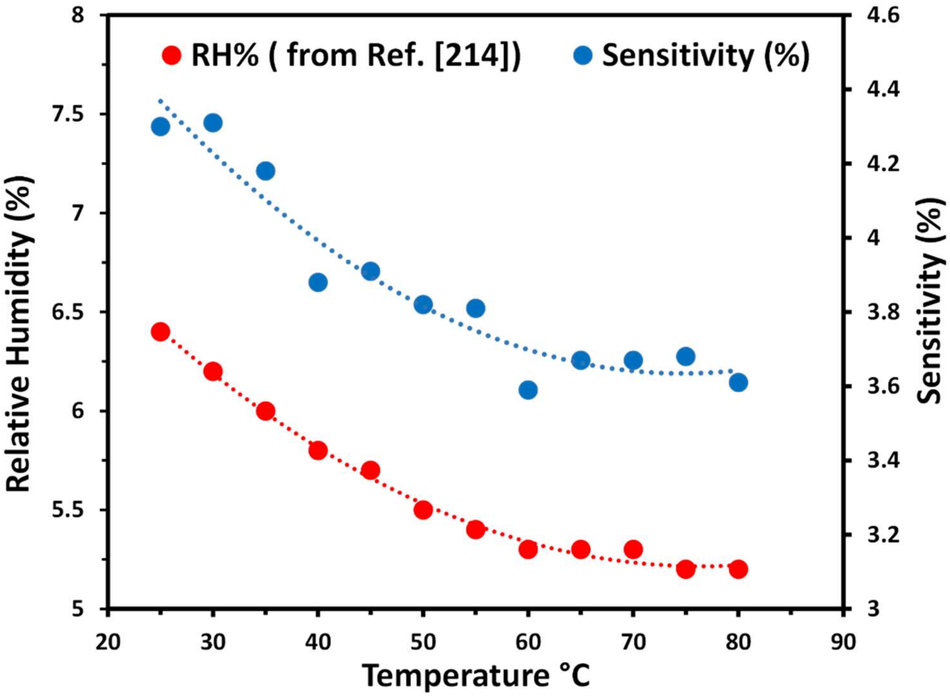

Figure 6.3. Performance of the sensor device at different temperatures.

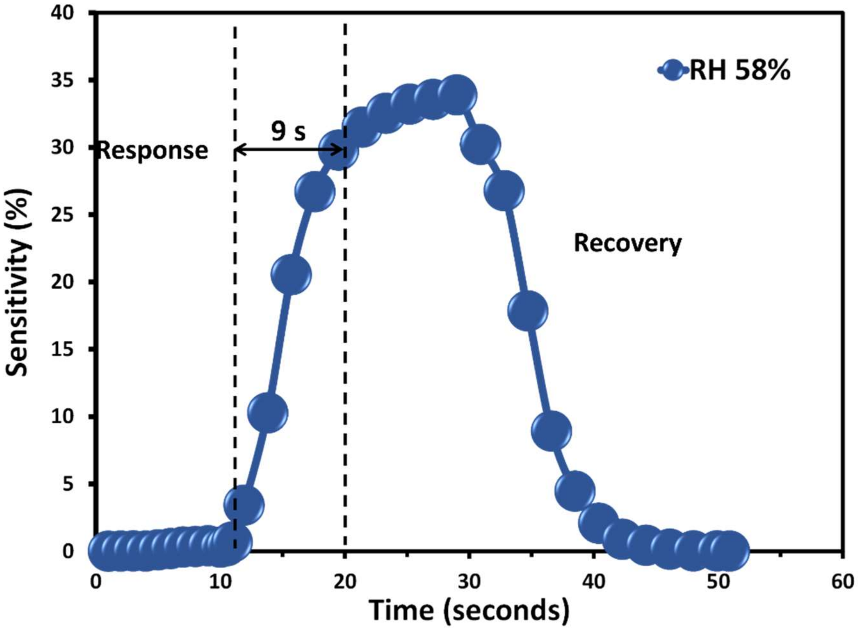

Figure 6.4. Response and recovery curve of the TRGO-based 3D printed sensor device at 58% RH.

of 58% at room temperature. The response time is calculated based on the time period required to reach 90% of the maximum resistance change. The response time recorder for our sensor in Figure 6.4 is 9 seconds which is much shorter than most values reported in the literature [65], [66], [232].

6.4 Conclusion

Additive manufacturing was employed to fabricate a TRGO-based 3D-printed humidity sensor device. The experiments showed a linear response of the sensor versus a wide range of RH (6.4%-97.3%) with slope of 0.603% Sensitivity/%RH. It was also shown that the sensor performance is independent of the temperature variations. The response time of the sensor to humidity was also revealed to be 9 seconds at the RH of 58% which is considerably fast compared to other reported values.

Chapter 7

Conclusions and Future Works

7.1 Summary

For the first time, binder-jet powder-bed additive manufacturing technique is used for the fabrication of graphene-based devices such as supercapacitors and sensors. Graphene-based materials are well-known for their exceptional properties; however, fabrication of full-scale devices from these materials is still under investigation and is yet to be commercialized. In this study, additive manufacturing, which has opened a new horizon towards fabrication, is shown as a simple and promising technique which can produce unique and complex graphene-based porous 3D structures for different application areas. As the first step, hydroxyapatite/graphene oxide nanocomposite powder was prepared and used in the retrofitted additive manufacturing machine for 3D printing of 3D structures which can potentially be used as bone-implants. Next, graphene oxide was synthesized from graphite and reduced through chemical and thermal methods. Both sample powders were 3D printed and used as electrodes in supercapacitor cells. The results revealed that the thermally reduced graphene oxide (TRGO) had better performance than the chemically reduced sample. In addition, nano palladium dispersion was prepared and injected into the TRGO-based electrodes which improved the performance of the 3D printed electrodes significantly. Finally, TRGO powder was 3D printed and assembled into a 3D printed polysiloxane embodiment to fabricate a humidity sensing device. The sensing performance of the device was promising in a wide range of humidity and independent of temperature variations.

7.2 Thesis Conclusions

The conclusions achieved through this study are as following:

1. Hydroxyapatite (Hap)/graphene based 3D structures were fabricated using binder-jet powder-bed additive manufacturing technique. The flowability of Hap/Graphene oxide powder was improved than that of Hap powder which resulted in fabrication of more dimensionally-stable structures. It was realized that 3D printing of the structures at the layer thickness of 125 μm and SBS/CBS ratio of 100/400% yielded higher mechanical strength. Also, addition of 0.4 wt.% of graphene oxide powder increased the mechanical strength significantly compared to the Hap structures.
2. The capacitance performance of chemically and thermally reduced graphene oxide samples were studied. PVA was added to graphene oxide dispersion during chemical reduction to provide spatial hindrance between graphene sheets and avoid agglomeration. It was realized that although thick 3D-printed electrodes based chemically reduced samples loaded with PVA showed higher capacitance, their performance was still inferior to the TRGO-based samples. It could be attributed to inherent higher specific surface area and also electrical conductivity of thermally reduced graphene oxide.
3. In order to improve the performance of the thick 3D-printed TRGO-based electrodes, we impregnated the samples with as-synthesized nano palladium dispersion to reduce the contact resistance between the graphene sheets. The experiments revealed a high gravimetric and areal capacitance values of 260 F/g and 700 mF/cm2 at the scan rate

of 5mV/s, respectively. The EIS also proved a low contact resistance and high rate of ion transport in the TRGO-nano palladium impregnated thick electrodes.

4. TRGO powder was used to 3D print a sensor device for humidity sensing applications. The results showed a linear response from the sensor to a wide range of RH with a very short response time. It was also shown that the 3D-printed sensor device is independent of temperature variations.

7.3 Recommendations and future work

The current work aims to introduce a new technique for fabrication of graphene-based 3D structures which potentially be used in commercial applications. However, further investigation is required to improve the properties of the fabricated devices. Towards this goal, the following studies are recommended as the future work:

7.3.1 Material development

Improving the flowability of the TRGO powder can improve the dimensional accuracy and macrostructure of the 3D printed structures. One of the recommended methods is to spray dry the TRGO dispersion and obtain hollow spherical powder with enhanced flowability. The effect of particle size on the flowability and performance of the 3D printed graphene-based structures can be a very interesting area of investigation.

In addition, the effect of C/O ratio on the performance of the TRGO-based 3D printed structures as electrode for supercapacitors and also a sensing device can be studied. Also, different mixtures of graphene oxide and TRGO can be prepared through spray drying and 3D printed for further analysis.

7.3.2 Additive manufacturing

One of the drawbacks of the 3D printed structures is low packing factor of the graphene-based 3D-printed structures which lowers the electrical conductivity and the therefore, the volume capacitance of the thick electrodes. Although improving the flowability of the TRGO powder can potentially enhance the packing factor of the 3D printed structures, there are a few features in the retrofitted additive manufacturing machine which can also contribute to higher bulk density of the structures. Layer thickness of powder, roller speed and motion, and also the concentration of the injected binder are the recommended parameters to study toward improving the packing factor.

7.3.3 Supplementary studies

7.3.3.1 Supercapacitors

One of the key recommendation to continue this study is to 3D print graphene-based electrodes at different thicknesses and investigate the optimum thickness which can result in higher gravimetric and volume capacitance.

Also, it was realized that the 1M sulfuric acid as the electrolyte can be corrosive to the current collector and other components of the cell leading inaccurate results. Therefore, it is recommended that different types of electrolytes such as ionic liquid be used in the supercapacitor cell for further analysis of the 3D printed graphene-based electrodes.

7.3.3.2 Sensors

The results obtained from the 3D printed TRGO-based device for humidity sensing were promising; however, further studies are required to explore the mechanism of sensing.

Also, in order to investigate the selectivity of this sensor, it is recommended that the response of this sensor to other chemicals such as alcohols and hydrogen peroxide be studied to find out the efficiency of this sensor for commercial applications

Letters of Copyright Permission

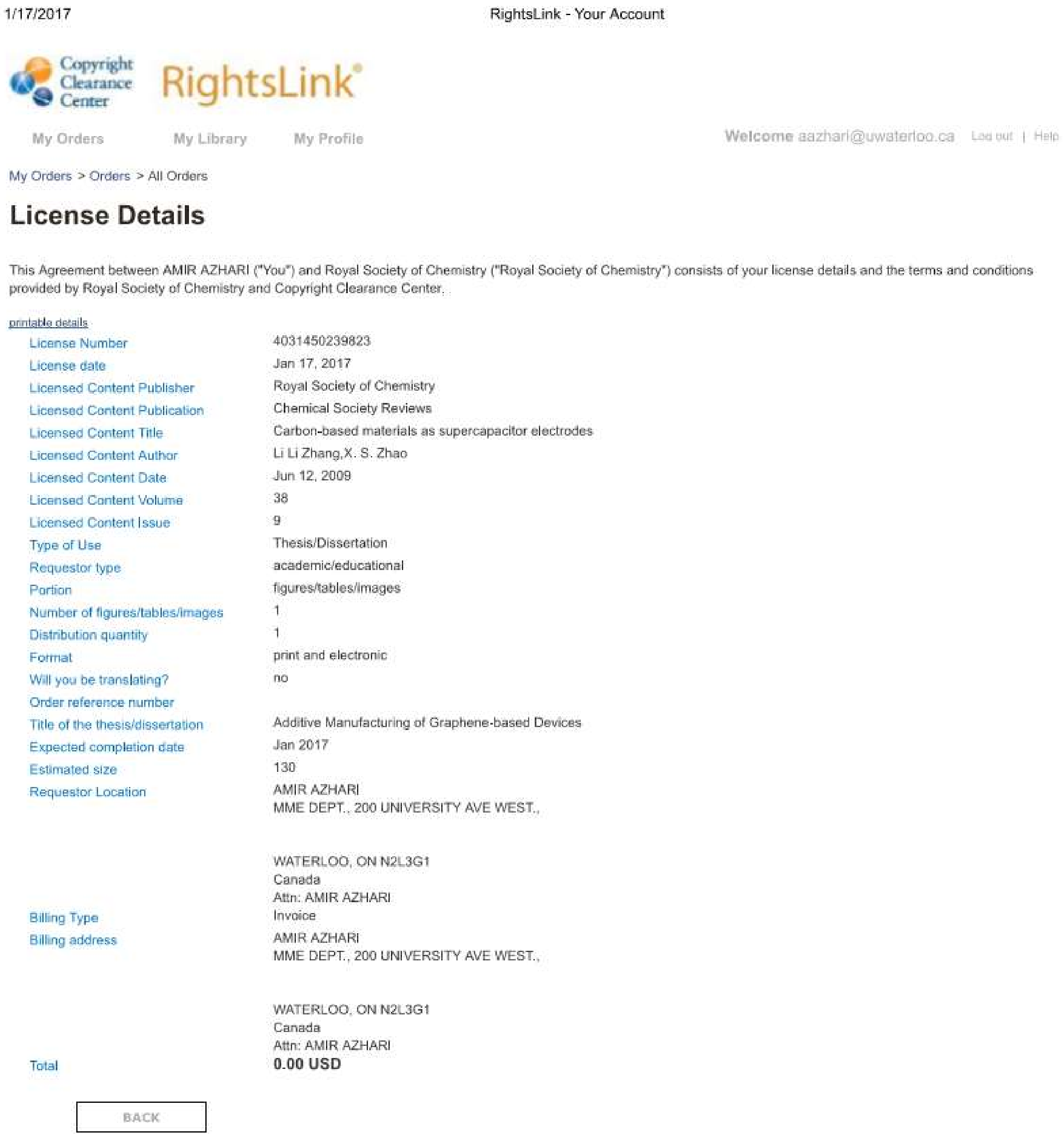

1/17/2017 RightsLink - Your Account

License Details

This Agreement between AMIR AZHARI ("You") and Royal Society of Chemistry ("Royal Society of Chemistry") consists of your license details and the terms and conditions provided by Royal Society of Chemistry and Copyright Clearance Center.

printable details

License Number	4031450239823
License date	Jan 17, 2017
Licensed Content Publisher	Royal Society of Chemistry
Licensed Content Publication	Chemical Society Reviews
Licensed Content Title	Carbon-based materials as supercapacitor electrodes
Licensed Content Author	Li Li Zhang,X. S. Zhao
Licensed Content Date	Jun 12, 2009
Licensed Content Volume	38
Licensed Content Issue	9
Type of Use	Thesis/Dissertation
Requestor type	academic/educational
Portion	figures/tables/images
Number of figures/tables/images	1
Distribution quantity	1
Format	print and electronic
Will you be translating?	no
Order reference number	
Title of the thesis/dissertation	Additive Manufacturing of Graphene-based Devices
Expected completion date	Jan 2017
Estimated size	130
Requestor Location	AMIR AZHARI MME DEPT., 200 UNIVERSITY AVE WEST., WATERLOO, ON N2L3G1 Canada Attn: AMIR AZHARI
Billing Type	Invoice
Billing address	AMIR AZHARI MME DEPT., 200 UNIVERSITY AVE WEST., WATERLOO, ON N2L3G1 Canada Attn: AMIR AZHARI
Total	**0.00 USD**

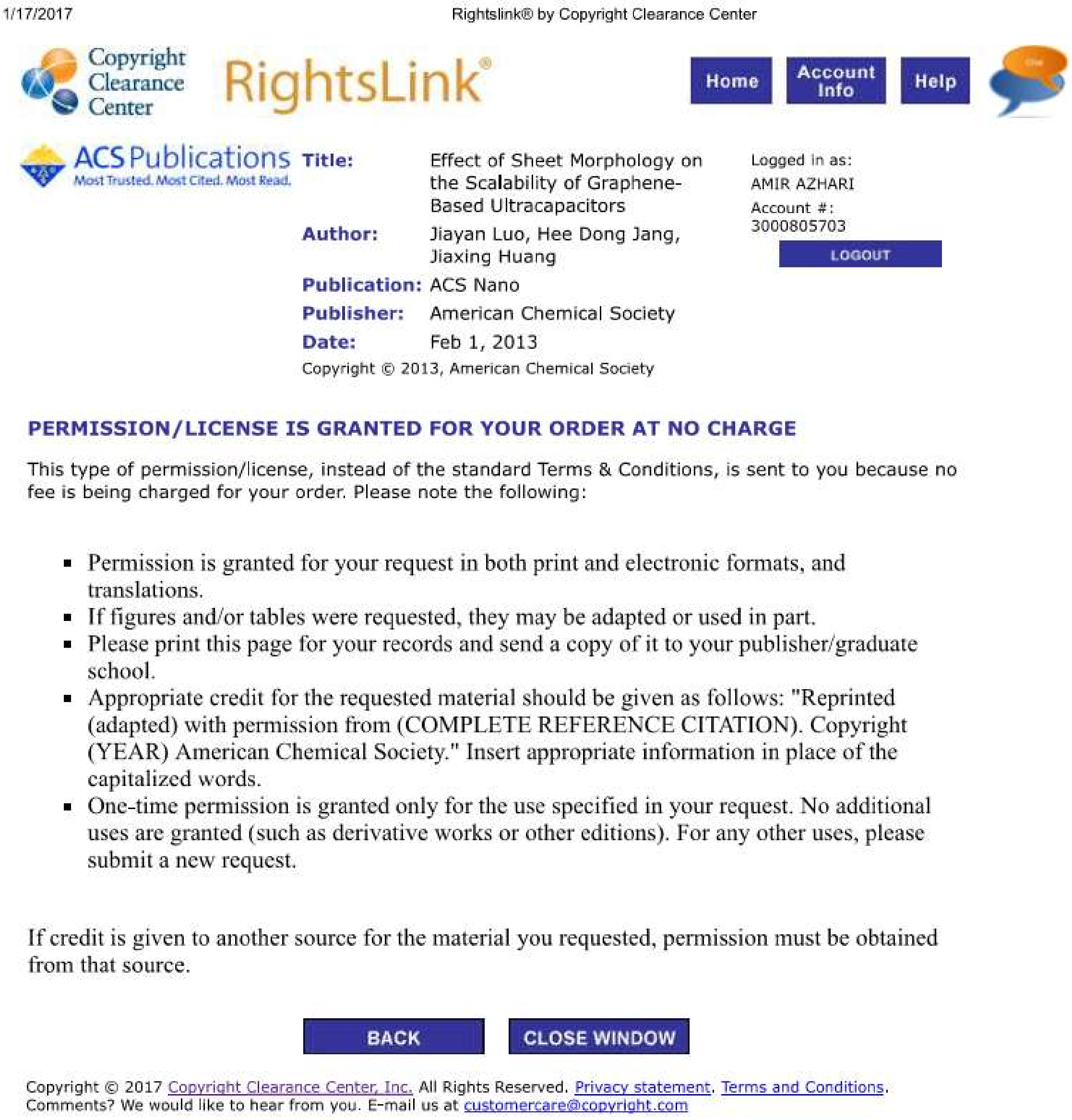

Title: Effect of Sheet Morphology on the Scalability of Graphene-Based Ultracapacitors

Author: Jiayan Luo, Hee Dong Jang, Jiaxing Huang

Publication: ACS Nano

Publisher: American Chemical Society

Date: Feb 1, 2013

Copyright © 2013, American Chemical Society

Logged in as:
AMIR AZHARI
Account #:
3000805703

PERMISSION/LICENSE IS GRANTED FOR YOUR ORDER AT NO CHARGE

This type of permission/license, instead of the standard Terms & Conditions, is sent to you because no fee is being charged for your order. Please note the following:

- Permission is granted for your request in both print and electronic formats, and translations.
- If figures and/or tables were requested, they may be adapted or used in part.
- Please print this page for your records and send a copy of it to your publisher/graduate school.
- Appropriate credit for the requested material should be given as follows: "Reprinted (adapted) with permission from (COMPLETE REFERENCE CITATION). Copyright (YEAR) American Chemical Society." Insert appropriate information in place of the capitalized words.
- One-time permission is granted only for the use specified in your request. No additional uses are granted (such as derivative works or other editions). For any other uses, please submit a new request.

If credit is given to another source for the material you requested, permission must be obtained from that source.

Copyright © 2017 Copyright Clearance Center, Inc. All Rights Reserved. Privacy statement. Terms and Conditions.
Comments? We would like to hear from you. E-mail us at customercare@copyright.com

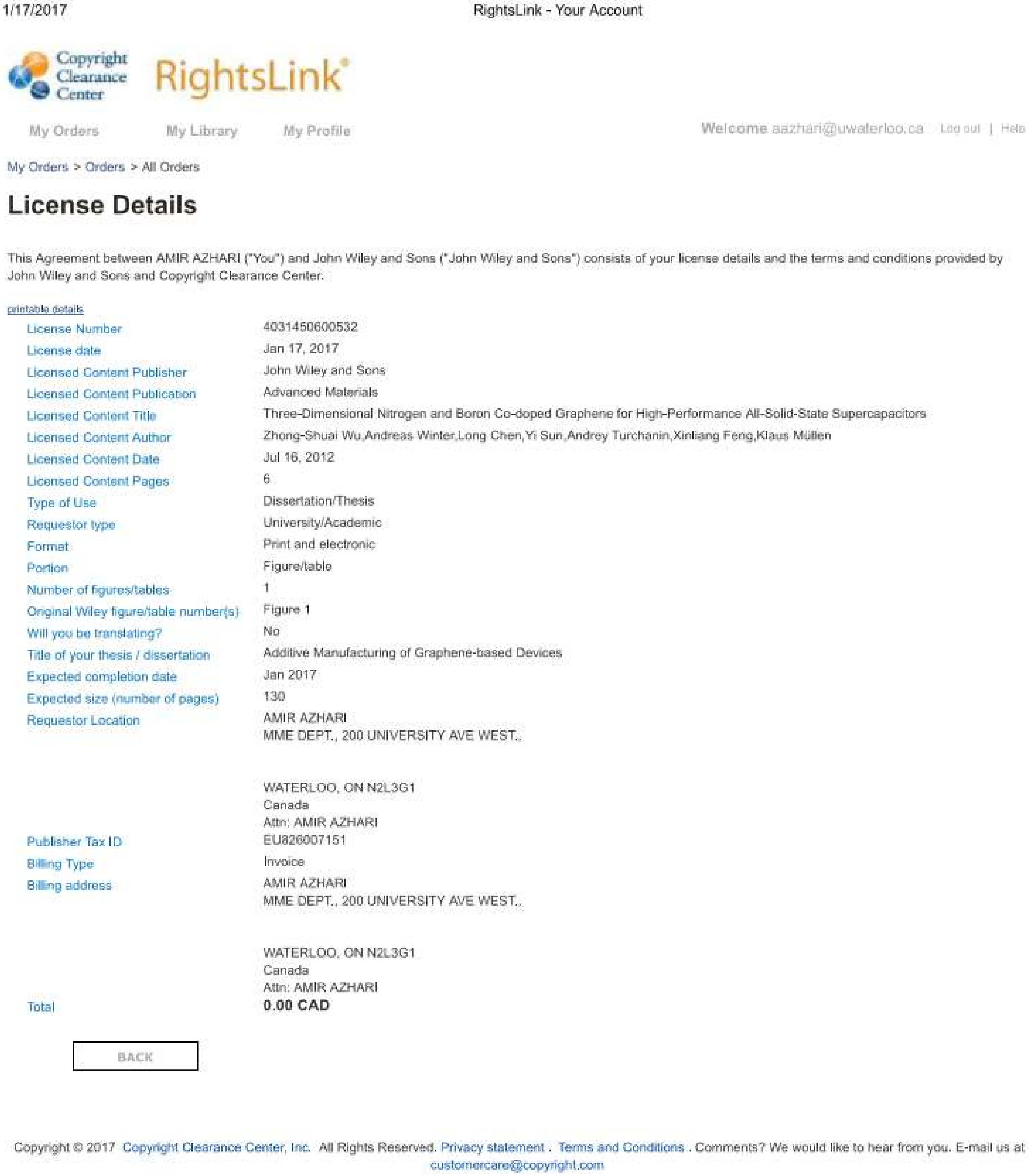

1/17/2017 RightsLink - Your Account

License Details

This Agreement between AMIR AZHARI ("You") and John Wiley and Sons ("John Wiley and Sons") consists of your license details and the terms and conditions provided by John Wiley and Sons and Copyright Clearance Center.

License Number	4031450600532
License date	Jan 17, 2017
Licensed Content Publisher	John Wiley and Sons
Licensed Content Publication	Advanced Materials
Licensed Content Title	Three-Dimensional Nitrogen and Boron Co-doped Graphene for High-Performance All-Solid-State Supercapacitors
Licensed Content Author	Zhong-Shuai Wu,Andreas Winter,Long Chen,Yi Sun,Andrey Turchanin,Xinliang Feng,Klaus Müllen
Licensed Content Date	Jul 16, 2012
Licensed Content Pages	6
Type of Use	Dissertation/Thesis
Requestor type	University/Academic
Format	Print and electronic
Portion	Figure/table
Number of figures/tables	1
Original Wiley figure/table number(s)	Figure 1
Will you be translating?	No
Title of your thesis / dissertation	Additive Manufacturing of Graphene-based Devices
Expected completion date	Jan 2017
Expected size (number of pages)	130
Requestor Location	AMIR AZHARI MME DEPT., 200 UNIVERSITY AVE WEST., WATERLOO, ON N2L3G1 Canada Attn: AMIR AZHARI
Publisher Tax ID	EU826007151
Billing Type	Invoice
Billing address	AMIR AZHARI MME DEPT., 200 UNIVERSITY AVE WEST., WATERLOO, ON N2L3G1 Canada Attn: AMIR AZHARI
Total	**0.00 CAD**

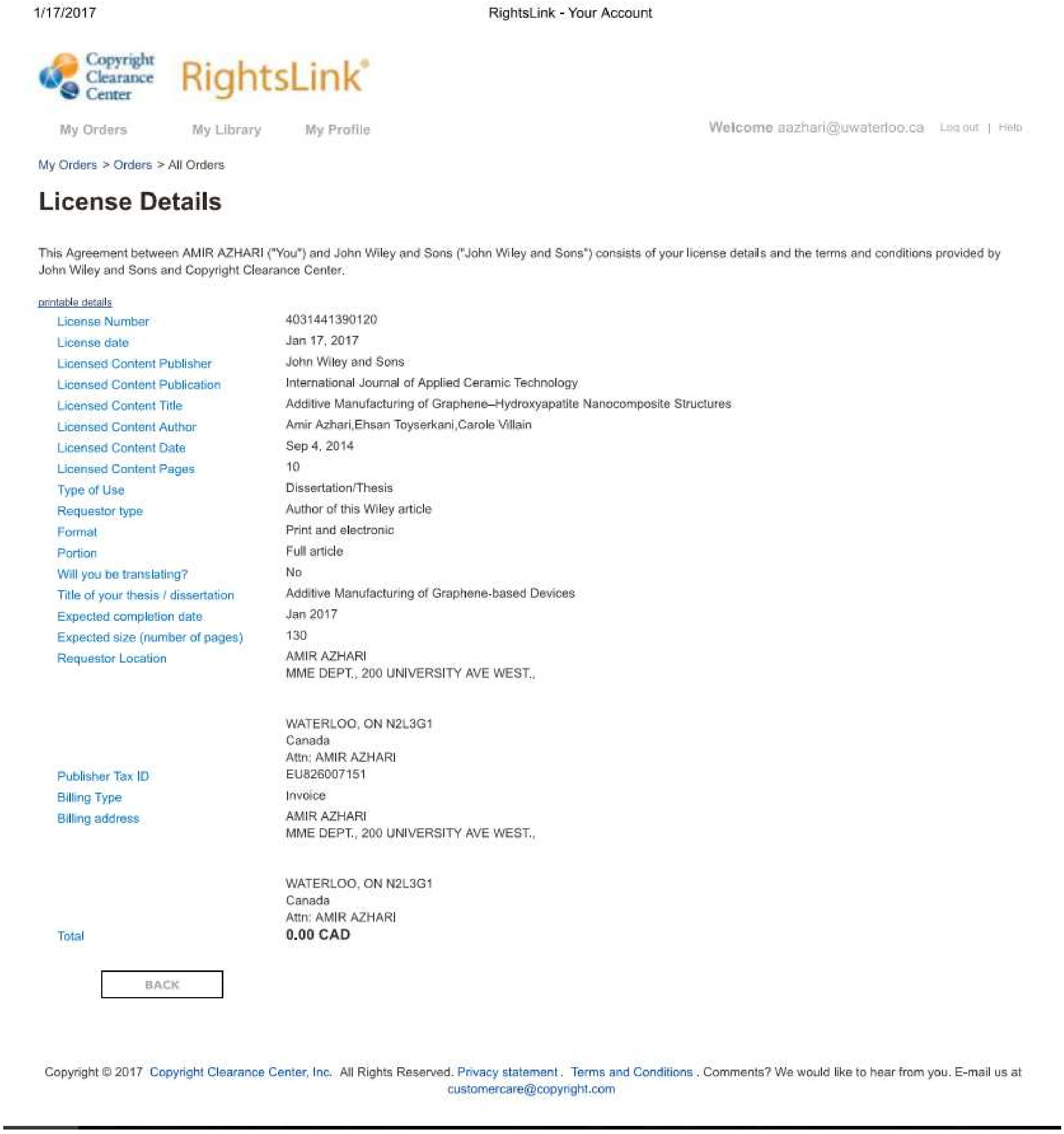

1/17/2017 RightsLink - Your Account

License Details

This Agreement between AMIR AZHARI ("You") and John Wiley and Sons ("John Wiley and Sons") consists of your license details and the terms and conditions provided by John Wiley and Sons and Copyright Clearance Center.

License Number	4031441390120
License date	Jan 17, 2017
Licensed Content Publisher	John Wiley and Sons
Licensed Content Publication	International Journal of Applied Ceramic Technology
Licensed Content Title	Additive Manufacturing of Graphene–Hydroxyapatite Nanocomposite Structures
Licensed Content Author	Amir Azhari,Ehsan Toyserkani,Carole Villain
Licensed Content Date	Sep 4, 2014
Licensed Content Pages	10
Type of Use	Dissertation/Thesis
Requestor type	Author of this Wiley article
Format	Print and electronic
Portion	Full article
Will you be translating?	No
Title of your thesis / dissertation	Additive Manufacturing of Graphene-based Devices
Expected completion date	Jan 2017
Expected size (number of pages)	130
Requestor Location	AMIR AZHARI MME DEPT., 200 UNIVERSITY AVE WEST., WATERLOO, ON N2L3G1 Canada Attn: AMIR AZHARI
Publisher Tax ID	EU826007151
Billing Type	Invoice
Billing address	AMIR AZHARI MME DEPT., 200 UNIVERSITY AVE WEST., WATERLOO, ON N2L3G1 Canada Attn: AMIR AZHARI
Total	**0.00 CAD**

Bibliography

[1] A. K. Geim and K. S. Novoselov, "The rise of graphene.," *Nat. Mater.*, vol. 6, no. 3, pp. 183–191, 2007.

[2] J. Du, X. Lai, N. Yang, J. Zhai, D. Kisailus, and F. Su, "Macro− Mesoporous TiO2− Graphene Composite Films: Improved Mass Transfer, Reduced Charge Recombination, and Their Enhanced Photocatalytic Activities," *ACS …*, vol. 5, no. 1, pp. 590–596, 2010.

[3] J. M. Taboas, R. D. Maddox, P. H. Krebsbach, and S. J. Hollister, "Indirect solid free form fabrication of local and global porous, biomimetic and composite 3D polymer-ceramic scaffolds.," *Biomaterials*, vol. 24, no. 1, pp. 181–94, Jan. 2003.

[4] B. Li and H. Cao, "ZnO@graphene composite with enhanced performance for the removal of dye from water," *J. Mater. Chem.*, vol. 21, no. 10, p. 3346, 2011.

[5] J. Dusza, J. Morgiel, and A. Duszová, "Microstructure and fracture toughness of Si 3 N 4+ graphene platelet composites," *J. Eur. Ceram. Soc.*, vol. 32, pp. 3389–3397, 2012.

[6] H. Zhang, X. Lv, Y. Li, Y. Wang, and J. Li, "P25-graphene composite as a high performance photocatalyst.," *ACS Nano*, vol. 4, no. 1, pp. 380–6, Jan. 2010.

[7] B. Lu, T. Li, H. Zhao, X. Li, C. Gao, S. Zhang, and E. Xie, "Graphene-based composite materials beneficial to wound healing.," *Nanoscale*, vol. 4, no. 9, pp. 2978–82, Apr. 2012.

[8] T. S. Sreeprasad, S. M. Maliyekkal, K. P. Lisha, and T. Pradeep, "Reduced graphene oxide-metal/metal oxide composites: facile synthesis and application in water purification.," *J. Hazard. Mater.*, vol. 186, no. 1, pp. 921–31, Feb. 2011.

[9] H. Fan, L. Wang, K. Zhao, N. Li, Z. Shi, Z. Ge, and Z. Jin, "Fabrication, mechanical properties, and biocompatibility of graphene-reinforced chitosan composites.," *Biomacromolecules*, vol. 11, no. 9, pp. 2345–51, Sep. 2010.

[10] S. Hein, K. Wang, W. F. Stevens, and J. Kjems, "Chitosan composites for biomedical applications: status, challenges and perspectives," *Mater. Sci. Technol.*, vol. 24, no. 9, pp. 1053–1061, Sep. 2008.

[11] C. Petit and T. J. Bandosz, "MOF Graphite Oxide Composites: Combining the Uniqueness of Graphene Layers and Metal Organic Frameworks," *Adv. Mater.*, vol. 21, pp. 4753–4757, Aug. 2009.

[12] N. A. Koratkar, *Graphene in composite materials: synthesis, characterization and applications*. DEStech Publications, 2013.

[13] J. Suwanprateeb, R. Sanngam, W. Suvannapruk, and T. Panyathanmaporn, "Mechanical and in vitro performance of apatite-wollastonite glass ceramic reinforced hydroxyapatite composite fabricated by 3D-printing.," *J. Mater. Sci. Mater. Med.*, vol. 20, no. 6, pp. 1281–9, Jul. 2009.

[14] Y. Qian, S. Lu, and F. Gao, "Preparation of MnO2/graphene composite as electrode material for supercapacitors," *J. Mater. Sci.*, vol. 46, no. 10, pp. 3517–3522, Jan. 2011.

[15] H. Zanin, E. Saito, F. R. Marciano, H. J. Ceragioli, A. E. Campos Granato, M. Porcionatto, and A. O. Lobo, “Fast preparation of nano-hydroxyapatite/superhydrophilic reduced graphene oxide composites for bioactive applications,” *J. Mater. Chem. B*, vol. 1, pp. 4947–4955, 2013.

[16] Y. Yang, W. Rigdon, X. Huang, and X. Li, “Enhancing graphene reinforcing potential in composites by hydrogen passivation induced dispersion.,” *Sci. Rep.*, vol. 3, p. 2086, Jan. 2013.

[17] A. Winkel, R. Meszaros, S. Reinsch, R. Müller, N. Travitzky, T. Fey, P. Greil, and L. Wondraczek, “Sintering of 3D-Printed Glass/HAp Composites,” *J. Am. Ceram. Soc.*, vol. 95, no. 11, pp. 3387–3393, Nov. 2012.

[18] S. Stankovich, D. a Dikin, G. H. B. Dommett, K. M. Kohlhaas, E. J. Zimney, E. a Stach, R. D. Piner, S. T. Nguyen, and R. S. Ruoff, “Graphene-based composite materials,” *Nature*, vol. 442, no. 7100, pp. 282–6, Jul. 2006.

[19] X. Wang, X. Zhou, K. Yao, J. Zhang, and Z. Liu, “A SnO2/graphene composite as a high stability electrode for lithium ion batteries,” *Carbon N. Y.*, vol. 49, no. 1, pp. 133–139, Jan. 2011.

[20] S.-L. Chou, J.-Z. Wang, M. Choucair, H.-K. Liu, J. a. Stride, and S.-X. Dou, “Enhanced reversible lithium storage in a nanosize silicon/graphene composite,” *Electrochem. commun.*, vol. 12, no. 2, pp. 303–306, Feb. 2010.

[21] D. Bitounis, H. Ali-Boucetta, B. H. Hong, D.-H. Min, and K. Kostarelos, “Prospects and challenges of graphene in biomedical applications.,” *Adv. Mater.*,

vol. 25, no. 16, pp. 2258–68, Apr. 2013.

[22] P. Blake, E. Hill, and A. Neto, "Making graphene visible," *Appl. Phys. Lett.*, vol. 91, pp. 2007–2009, 2007.

[23] L. A. Falkovsky, "Optical properties of graphene," *J. Phys. Conf. Ser.*, vol. 129, pp. 1–7, 2008.

[24] S. P. Apell, G. W. Hanson, and C. Hägglund, "High optical absorption in graphene," 2012.

[25] K. P. Loh, Q. Bao, G. Eda, and M. Chhowalla, "Graphene oxide as a chemically tunable platform for optical applications.," *Nat. Chem.*, vol. 2, no. 12, pp. 1015–24, Dec. 2010.

[26] T. Mueller, F. Xia, and P. Avouris, "Graphene photodetectors for high-speed optical communications," *Nat. Photonics*, vol. 4, no. March, pp. 297–301, 2010.

[27] L. Falkovsky and S. Pershoguba, "Optical far-infrared properties of a graphene monolayer and multilayer," *Phys. Rev. B*, vol. 76, pp. 1–4, 2007.

[28] Q. Li, S. Mahendra, D. Y. Lyon, L. Brunet, M. V Liga, D. Li, and P. J. J. Alvarez, "Antimicrobial nanomaterials for water disinfection and microbial control: potential applications and implications.," *Water Res.*, vol. 42, no. 18, pp. 4591–602, Nov. 2008.

[29] C. Liu, Z. Yu, D. Neff, A. Zhamu, and B. Z. Jang, "Graphene-Based Supercapacitor with an Ultrahigh Energy Density.," *Nano Lett.*, pp. 4863–4868,

Nov. 2010.

[30] G. Wang, X. Shen, J. Yao, and J. Park, “Graphene nanosheets for enhanced lithium storage in lithium ion batteries,” *Carbon N. Y.*, vol. 47, no. 8, pp. 2049–2053, Jul. 2009.

[31] E. Yoo, J. Kim, E. Hosono, H. Zhou, T. Kudo, and I. Honma, “Large reversible Li storage of graphene nanosheet families for use in rechargeable lithium ion batteries.,” *Nano Lett.*, vol. 8, no. 8, pp. 2277–82, Aug. 2008.

[32] M. Rafiee, J. Rafiee, Z. Wang, and H. Song, “Enhanced mechanical properties of nanocomposites at low graphene content,” *ACS …*, vol. 3, no. 12, pp. 3884–3890, 2009.

[33] Y. Quan, M. Lu, M. Tian, S. Yan, Z. Yu, and L. Zhang, “Functional and mechanical properties of acrylate elastomer/expanded graphite nanocomposites,” *J. Appl. Polym. Sci.*, vol. 130, no. 1, pp. 680–686, Oct. 2013.

[34] M. Rafiee, J. Rafiee, Z. Wang, and H. Song, “Enhanced mechanical properties of nanocomposites at low graphene content,” *ACS …*, vol. 3, no. 12, pp. 3384–3890, 2009.

[35] L. Chen, S. Chai, K. Liu, N. Ning, J. Gao, Q. Liu, F. Chen, and Q. Fu, “Enhanced epoxy/silica composites mechanical properties by introducing graphene oxide to the interface.,” *ACS Appl. Mater. Interfaces*, vol. 4, no. 8, pp. 4398–404, Aug. 2012.

[36] P. Kun, O. Tapasztó, F. Wéber, and C. Balázsi, “Determination of structural and

mechanical properties of multilayer graphene added silicon nitride-based composites," *Ceram. Int.*, vol. 38, no. 1, pp. 211–216, Jan. 2012.

[37] L. S. Walker, V. R. Marotto, M. a Rafiee, N. Koratkar, and E. L. Corral, "Toughening in graphene ceramic composites.," *ACS Nano*, vol. 5, no. 4, pp. 3182–90, Apr. 2011.

[38] R. a. a. Muzzarelli, "Chitosan composites with inorganics, morphogenetic proteins and stem cells, for bone regeneration," *Carbohydr. Polym.*, vol. 83, no. 4, pp. 1433–1445, Feb. 2011.

[39] Y. Zhang and C. Pan, "TiO2/graphene composite from thermal reaction of graphene oxide and its photocatalytic activity in visible light," *J. Mater. Sci.*, vol. 46, no. 8, pp. 2622–2626, Dec. 2010.

[40] Y. J. Mai, X. L. Wang, J. Y. Xiang, Y. Q. Qiao, D. Zhang, C. D. Gu, and J. P. Tu, "CuO/graphene composite as anode materials for lithium-ion batteries," *Electrochim. Acta*, vol. 56, no. 5, pp. 2306–2311, Feb. 2011.

[41] X. Wang, H. Bai, Z. Yao, A. Liu, and G. Shi, "Electrically conductive and mechanically strong biomimetic chitosan/reduced graphene oxide composite films," *J. Mater. Chem.*, vol. 20, no. 41, p. 9032, 2010.

[42] L. Rodríguez-Lorenzo, "Synthesis and Biocompatibility of Hydroxyapatite in a Graphite Oxide Matrix," *Key Eng. …*, 2009.

[43] M. Li, Y. Wang, Q. Liu, Q. Li, Y. Cheng, Y. Zheng, T. Xi, and S. Wei, "In situ synthesis and biocompatibility of nano hydroxyapatite on pristine and chitosan

functionalized graphene oxide," *J. Mater. Chem. B*, vol. 1, no. 4, p. 475, 2013.

[44] H. Liu, P. Xi, G. Xie, Y. Shi, F. Hou, L. Huang, F. Chen, Z. Zeng, C. Shao, and J. Wang, "Simultaneous Reduction and Surface Functionalization of Graphene Oxide for Hydroxyapatite Mineralization," *J. Phys. Chem. C*, vol. 116, no. 5, pp. 3334–3341, Feb. 2012.

[45] A. R. Biris, M. Mahmood, M. D. Lazar, E. Dervishi, F. Watanabe, T. Mustafa, G. Baciut, M. Baciut, S. Bran, S. Ali, and A. S. Biris, "Novel Multicomponent and Biocompatible Nanocomposite Materials Based on Few-Layer Graphenes Synthesized on a Gold/Hydroxyapatite Catalytic System with Applications in Bone Regeneration," *J. Phys. Chem. C*, vol. 115, no. 39, pp. 18967–18976, Oct. 2011.

[46] L. L. Zhang, R. Zhou, and X. S. Zhao, "Graphene-based materials as supercapacitor electrodes," *J. Mater. Chem.*, vol. 20, no. 29, p. 5983, 2010.

[47] N. Omar, M. Daowd, P. van den Bossche, O. Hegazy, J. Smekens, T. Coosemans, and J. van Mierlo, "Rechargeable energy storage systems for plug-in hybrid electric vehicles-assessment of electrical characteristics," *Energies*, vol. 5, no. 8, pp. 2952–2988, 2012.

[48] M. A. Pope and I. A. Aksay, "Four-Fold Increase in the Intrinsic Capacitance of Graphene through Functionalization and Lattice Disorder," *J. Phys. Chem. C*, vol. 119, no. 35, pp. 20369–20378, 2015.

[49] J. Luo, H. D. Jang, and J. Huang, "Effect of Sheet Morphology on the Scalability

of Graphene-Based Ultracapacitors," *ACS Nano*, vol. 7, no. 2, pp. 1464–1471, 2013.

[50] F. Stoeckli and T. a. Centeno, "Optimization of the characterization of porous carbons for supercapacitors," *J. Mater. Chem. A*, vol. 1, no. 23, p. 6865, 2013.

[51] H. Yang, S. Kannappan, A. S. Pandian, J.-H. Jang, Y. S. Lee, and W. Lu, "Nanoporous graphene materials by low-temperature vacuum-assisted thermal process for electrochemical energy storage," *J. Power Sources*, vol. 284, pp. 146–153, Jun. 2015.

[52] a. G. Pandolfo and a. F. Hollenkamp, "Carbon properties and their role in supercapacitors," *J. Power Sources*, vol. 157, no. 1, pp. 11–27, Jun. 2006.

[53] K. S. Novoselov, V. I. Fal'ko, L. Colombo, P. R. Gellert, M. G. Schwab, and K. Kim, "A roadmap for graphene.," *Nature*, vol. 490, no. 7419, pp. 192–200, Oct. 2012.

[54] W. Chen and L. Yan, "In situ self-assembly of mild chemical reduction graphene for three-dimensional architectures," *Nanoscale*, vol. 3, no. 8, pp. 3132–7, Aug. 2011.

[55] Z. Chen, W. Ren, L. Gao, B. Liu, S. Pei, and H.-M. Cheng, "Three-dimensional flexible and conductive interconnected graphene networks grown by chemical vapour deposition.," *Nat. Mater.*, vol. 10, no. 6, pp. 424–8, Jun. 2011.

[56] Z.-S. Wu, A. Winter, L. Chen, Y. Sun, A. Turchanin, X. Feng, and K. Müllen, "Three-dimensional nitrogen and boron co-doped graphene for high-performance

all-solid-state supercapacitors.," *Adv. Mater.*, vol. 24, no. 37, pp. 5130–5, Sep. 2012.

[57] N. Syafira, A. Manaf, M. Shahril, A. Bistamam, and M. A. Azam, "JSS FOCUS ISSUE ON NANOCARBONS FOR ENERGY HARVESTING AND STORAGE Development of High Performance Electrochemical Capacitor: A Systematic Review of Electrode Fabrication Technique Based on Different Carbon Materials," *ECS J. Solid State Sci. Technol.*, vol. 2, no. 10, pp. 3101–3119, 2013.

[58] "ASTM Standard F42, 2012, 'Standard Terminology for Additive Manufacturing Technologies,' ASTM International, West Conshohocken, PA, 2012, DOI: 10.1520/F2792-12A, www.astm.org." .

[59] M. Vlasea, E. Toyserkani, and R. Pilliar, "Effect of gray scale binder levels on additive manufacturing of porous scaffolds with heterogeneous properties," *Int. J. Appl. Ceram. Technol.*, vol. 12, no. 1, pp. 62–70, 2015.

[60] A. Basalah, Y. Shanjani, S. Esmaeili, and E. Toyserkani, "Characterizations of additive manufactured porous titanium implants," *J. Biomed. Mater. Res. - Part B Appl. Biomater.*, vol. 100 B, no. 7, pp. 1970–1979, 2012.

[61] Y. Shanjani, Y. Hu, R. M. Pilliar, and E. Toyserkani, "Mechanical characteristics of solid-freeform-fabricated porous calcium polyphosphate structures with oriented stacked layers," *Acta Biomater.*, vol. 7, no. 4, pp. 1788–1796, 2011.

[62] Y. Shanjani, J. N. Amritha De Croos, R. M. Pilliar, R. A. Kandel, and E. Toyserkani, "Solid freeform fabrication and characterization of porous calcium

polyphosphate structures for tissue engineering purposes," *J. Biomed. Mater. Res. - Part B Appl. Biomater.*, vol. 93, no. 2, pp. 510–519, 2010.

[63] L. T. Duy, T. Q. Trung, V. Q. Dang, U. Hwang, S. Siddiqui, I. Son, S. K. Yoon, D. J. Chung, and N. Lee, "Flexible Transparent Reduced Graphene Oxide Sensor Coupled with Organic Dye Molecules for Rapid Dual-Mode Ammonia Gas Detection," pp. 4329–4338, 2016.

[64] M. Lim, H. Shin, D. Myung, S. Lee, and J. Lee, "Poly (vinyl alcohol) nanocomposites containing reduced graphene oxide coated with tannic acid for humidity sensor," *Polymer (Guildf).*, vol. 84, no. 2016, pp. 89–98, 2016.

[65] Y. Li, K. Fan, H. Ban, and M. Yang, "Detection of very low humidity using polyelectrolyte/graphene bilayer humidity sensors," *Sensors Actuators, B Chem.*, vol. 222, no. 2016, pp. 151–158, 2016.

[66] P.-G. Su and C.-F. Chiou, "Electrical and humidity-sensing properties of reduced graphene oxide thin film fabricated by layer-by-layer with covalent anchoring on flexible substrate," *Sensors Actuators B Chem.*, vol. 200, no. 2014, pp. 9–18, 2014.

[67] J. V. L. Silva and R. A. Rezende, "Additive Manufacturing and its future impact in logistics."

[68] C. W. Gomes, *Rapid Prototyping: Theory and Practice*. Springer, 2006.

[69] A. E. W. Rennie, C. E. Booking, and D. M. Jacobson, Eds., *Rapid Prototyping, Tooling, and Manufacturing*. 2002.

[70] I. Gibson, D. Rosen, and B. Stucker, *Additive manufacturing technologies: rapid prototyping to direct digital manufacturing*. Springer, 2010.

[71] E. H.-J. Kim, X. D. Chen, and D. Pearce, “Effect of surface composition on the flowability of industrial spray-dried dairy powders.,” *Colloids Surf. B. Biointerfaces*, vol. 46, no. 3, pp. 182–7, Dec. 2005.

[72] C. Shanjani, Y., Toyserkani, E., & Wei, “Modeling and characterization of biomaterials spreading properties in powder-based rapid prototyping techniques,” *ASME 2007 Int. Mech. Eng. Congr. Expo.*, pp. 135–143, 2007.

[73] a Butscher, M. Bohner, N. Doebelin, L. Galea, O. Loeffel, and R. Müller, “Moisture based three-dimensional printing of calcium phosphate structures for scaffold engineering.,” *Acta Biomater.*, vol. 9, no. 2, pp. 5369–78, Feb. 2013.

[74] J. Yang, A. Sliva, A. Banerjee, R. N. Dave, and R. Pfeffer, “Dry particle coating for improving the flowability of cohesive powders,” *Powder Technol.*, vol. 158, no. 1–3, pp. 21–33, Oct. 2005.

[75] M. Katsnelson, “Graphene: carbon in two dimensions,” *Mater. today*, vol. 10, no. 1, pp. 20–27, 2007.

[76] M. I. Katsnelson, *Graphene: Carbon in two dimensions*. Cambridge University Press, 2012.

[77] P. Mukhopadhyay and R. K. Gupta, Eds., *Graphite, Grpahene and their polymer nanocomposites*. Taylor & Francis Group, 2013.

[78] W. Choi and J. Lee, Eds., *Graphene: synthesis and applications*. Taylor & Francis Group, 2012.

[79] J. H. Warner, F. Schaffel, A. Bachmatiuk, and M. H. Rummeli, *Graphene: Fundamentals and emergent applications*, First. Elsevier, 2013.

[80] H. Pang, T. Chen, G. Zhang, B. Zeng, and Z.-M. Li, "An electrically conducting polymer/graphene composite with a very low percolation threshold," *Mater. Lett.*, vol. 64, no. 20, pp. 2226–2229, Oct. 2010.

[81] S. N. Tripathi, P. Saini, D. Gupta, and V. Choudhary, "Electrical and mechanical properties of PMMA/reduced graphene oxide nanocomposites prepared via in situ polymerization," *J. Mater. Sci.*, vol. 48, no. 18, pp. 6223–6232, May 2013.

[82] A. Liu, C. Li, H. Bai, and G. Shi, "Electrochemical Deposition of Polypyrrole/Sulfonated Graphene Composite Films," *J. Phys. Chem. C*, vol. 114, no. 51, pp. 22783–22789, Dec. 2010.

[83] D. Zhang, X. Zhang, Y. Chen, P. Yu, C. Wang, and Y. Ma, "Enhanced capacitance and rate capability of graphene/polypyrrole composite as electrode material for supercapacitors," *J. Power Sources*, vol. 196, no. 14, pp. 5990–5996, Jul. 2011.

[84] J. Wang, X. Wang, C. Xu, M. Zhang, and X. Shang, "Preparation of graphene/poly(vinyl alcohol) nanocomposites with enhanced mechanical properties and water resistance," *Polym. Int.*, vol. 60, no. 5, pp. 816–822, May 2011.

[85] X. Zhao, Q. Zhang, D. Chen, and P. Lu, "Enhanced Mechanical Properties of

Graphene-Based Poly(vinyl alcohol) Composites," *Macromolecules*, vol. 43, no. 5, pp. 2357–2363, Mar. 2010.

[86] T. Huang, Y. Xin, T. Li, S. Nutt, and C. Su, "Modified Graphene/Polyimide Nanocomposites: Reinforcing and Tribological Effects," ... *Appl. Mater. ...*, 2013.

[87] C. Wonbong and J. Lee, Eds., *graphene synthesis and applications*. Taylor & Francis Group, 2012.

[88] H. Kim, S.-W. Kim, Y.-U. Park, H. Gwon, D.-H. Seo, Y. Kim, and K. Kang, "SnO2/graphene composite with high lithium storage capability for lithium rechargeable batteries," *Nano Res.*, vol. 3, no. 11, pp. 813–821, Oct. 2010.

[89] W.-K. Jo, "Coupling of graphene oxide into titania for purification of gaseous toluene under different operational conditions," *Vacuum*, vol. 99, pp. 22–25, Jan. 2014.

[90] S. Chen, J. Zhu, X. Wu, Q. Han, and X. Wang, "Graphene oxide− MnO2 nanocomposites for supercapacitors," *ACS Nano*, vol. 4, no. 5, pp. 2822–2830, 2010.

[91] X. Liu, L. Pan, T. Lv, T. Lu, G. Zhu, Z. Sun, and C. Sun, "Microwave-assisted synthesis of ZnO–graphene composite for photocatalytic reduction of Cr(vi)," *Catal. Sci. Technol.*, vol. 1, no. 7, p. 1189, 2011.

[92] G. Wang, T. Liu, Y. Luo, Y. Zhao, Z. Ren, J. Bai, and H. Wang, "Preparation of Fe2O3/graphene composite and its electrochemical performance as an anode material for lithium ion batteries," *J. Alloys Compd.*, vol. 509, no. 24, pp. L216–

L220, Jun. 2011.

[93] P. a. a. P. Marques, G. Gonçalves, M. K. Singh, and J. Grácio, “Graphene Oxide and Hydroxyapatite as Fillers of Polylactic Acid Nanocomposites: Preparation and Characterization,” *J. Nanosci. Nanotechnol.*, vol. 12, no. 8, pp. 6686–6692, Aug. 2012.

[94] H. Ma, W. Su, Z. Tai, D. Sun, X. Yan, B. Liu, and Q. Xue, “Preparation and cytocompatibility of polylactic acid/hydroxyapatite/graphene oxide nanocomposite fibrous membrane,” *Chinese Sci. Bull.*, vol. 57, no. 23, pp. 3051–3058, Aug. 2012.

[95] P.-P. Zuo, H.-F. Feng, Z.-Z. Xu, L.-F. Zhang, Y.-L. Zhang, W. Xia, and W.-Q. Zhang, “Fabrication of biocompatible and mechanically reinforced graphene oxide-chitosan nanocomposite films.,” *Chem. Cent. J.*, vol. 7, no. 1, p. 39, Jan. 2013.

[96] Y. Pan, T. Wu, H. Bao, and L. Li, “Green fabrication of chitosan films reinforced with parallel aligned graphene oxide,” *Carbohydr. Polym.*, vol. 83, no. 4, pp. 1908–1915, Feb. 2011.

[97] D. Depan, B. Girase, J. S. Shah, and R. D. K. Misra, “Structure-process-property relationship of the polar graphene oxide-mediated cellular response and stimulated growth of osteoblasts on hybrid chitosan network structure nanocomposite scaffolds.,” *Acta Biomater.*, vol. 7, no. 9, pp. 3432–45, Sep. 2011.

[98] X. Yang, Y. Tu, L. Li, S. Shang, and X.-M. Tao, “Well-dispersed chitosan/graphene oxide nanocomposites.,” *ACS Appl. Mater. Interfaces*, vol. 2,

no. 6, pp. 1707–13, Jun. 2010.

[99] R. Chumnanklang, T. Panyathanmaporn, K. Sitthiseripratip, and J. Suwanprateeb, "3D printing of hydroxyapatite: Effect of binder concentration in pre-coated particle on part strength," *Mater. Sci. Eng. C*, vol. 27, no. 4, pp. 914–921, May 2007.

[100] B. Leukers, H. Gülkan, S. H. Irsen, S. Milz, C. Tille, H. Seitz, and M. Schieker, "Biocompatibility of ceramic scaffolds for bone replacement made by 3D printing," *Materwiss. Werksttech.*, vol. 36, no. 12, pp. 781–787, Dec. 2005.

[101] J. Suwanprateeb, R. Sanngam, and T. Panyathanmaporn, "Influence of raw powder preparation routes on properties of hydroxyapatite fabricated by 3D printing technique," *Mater. Sci. Eng. C*, vol. 30, no. 4, pp. 610–617, May 2010.

[102] F. C. Fierz, F. Beckmann, M. Huser, S. H. Irsen, B. Leukers, F. Witte, O. Degistirici, A. Andronache, M. Thie, and B. Müller, "The morphology of anisotropic 3D-printed hydroxyapatite scaffolds.," *Biomaterials*, vol. 29, no. 28, pp. 3799–806, Oct. 2008.

[103] C. Peniche, Y. Solís, N. Davidenko, and R. García, "Chitosan/hydroxyapatite-based composites," *Biotecnol. Apl.*, vol. 27, no. 3, pp. 202–210, 2010.

[104] J. Li, Y. Chen, Y. Yin, F. Yao, and K. Yao, "Modulation of nano-hydroxyapatite size via formation on chitosan-gelatin network film in situ.," *Biomaterials*, vol. 28, no. 5, pp. 781–90, Feb. 2007.

[105] Y. Bin Tan and J.-M. Lee, "Graphene for supercapacitor applications," *J. Mater.*

Chem. A, vol. 1, no. 47, p. 14814, 2013.

[106] L. L. Zhang, R. Zhou, and X. S. Zhao, "Carbon-based materials as supercapacitor electrodes," *J. Mater. Chem.*, vol. 38, no. 29, pp. 2520–2531, 2009.

[107] R. J. B. M. Winter, "What Are Batteries , Fuel Cells , and Supercapacitors ?," *Chem. Rev.*, vol. 104, pp. 42545–4269, 2004.

[108] L. Grande, V. T. Chundi, D. Wei, C. Bower, P. Andrew, and T. Ryhänen, "Graphene for energy harvesting/storage devices and printed electronics," *Particuology*, vol. 10, no. 1, pp. 1–8, 2012.

[109] E. Frackowiak and F. Béguin, "Carbon materials for the electrochemical storage of energy in capacitors," *Carbon N. Y.*, vol. 39, no. 6, pp. 937–950, 2001.

[110] G. Wang, L. Zhang, and J. Zhang, "A review of electrode materials for electrochemical supercapacitors," *Chem. Soc. Rev.*, vol. 41, no. 2, pp. 797–828, Jan. 2012.

[111] C. Punckt, M. A. Pope, and I. A. Aksay, "High Selectivity of Porous Graphene Electrodes Solely Due to Transport and Pore Depletion E ff ects," 2014.

[112] D. Wang, R. Kou, D. Choi, Z. Yang, Z. Nie, J. Li, L. V Saraf, D. Hu, J. Zhang, G. L. Graff, J. Liu, M. a Pope, and I. a Aksay, "Ternary self-assembly of ordered metal oxide-graphene nanocomposites for electrochemical energy storage.," *ACS Nano*, vol. 4, no. 3, pp. 1587–95, Mar. 2010.

[113] C. Punckt, M. a. Pope, J. Liu, Y. Lin, and I. a. Aksay, "Electrochemical

Performance of Graphene as Effected by Electrode Porosity and Graphene Functionalization," *Electroanalysis*, vol. 22, no. 23, pp. 2834–2841, Dec. 2010.

[114] C. Punckt, M. A. Pope, J. Liu, Y. Lin, and I. A. Aksay, "Electrochemical performance of graphene as effected by electrode porosity and graphene functionalization," *Electroanalysis*, vol. 22, no. 23, pp. 2834–2841, 2010.

[115] J. Bai, X. Zhong, S. Jiang, Y. Huang, and X. Duan, "Graphene nanomesh.," *Nat. Nanotechnol.*, vol. 5, no. 3, pp. 190–4, 2010.

[116] O. Akhavan, "Graphene nanomesh by ZnO nanorod photocatalysts," *ACS Nano*, vol. 4, no. 7, pp. 4174–4180, 2010.

[117] M. D. Fischbein and M. Drndić, "Electron beam nanosculpting of suspended graphene sheets," *Appl. Phys. Lett.*, vol. 93, no. 11, pp. 2006–2009, 2008.

[118] G. Ning, Z. Fan, G. Wang, J. Gao, W. Qian, and F. Wei, "Gram-scale synthesis of nanomesh graphene with high surface area and its application in supercapacitor electrodes," *Chem Commun*, vol. 47, no. 21, pp. 5976–5978, 2011.

[119] J. Yan, Z. Fan, W. Sun, G. Ning, T. Wei, Q. Zhang, R. Zhang, L. Zhi, and F. Wei, "Advanced asymmetric supercapacitors based on Ni(OH) \n
2/graphene and porous graphene electrodes with high energy density," *Adv. Funct. Mater.*, vol. 22, no. 12, pp. 2632–2641, 2012.

[120] Z. Fan, J. Yan, G. Ning, T. Wei, L. Zhi, and F. Wei, "Porous graphene networks as high performance anode materials for lithium ion batteries," *Carbon N. Y.*, vol. 60, pp. 558–561, 2013.

[121] Y. Zhu, S. Murali, M. D. Stoller, K. J. Ganesh, W. Cai, P. J. Ferreira, A. Pirkle, R. M. Wallace, K. a Cychosz, M. Thommes, D. Su, E. a Stach, and R. S. Ruoff, "Carbon-Based Supercapacitors," *Science (80-.).*, vol. 332, no. June, pp. 1537–1542, 2011.

[122] L. Zhang, F. Zhang, X. Yang, G. Long, Y. Wu, T. Zhang, K. Leng, Y. Huang, Y. Ma, A. Yu, and Y. Chen, "Porous 3D graphene-based bulk materials with exceptional high surface area and excellent conductivity for supercapacitors," *Sci Rep*, vol. 3, p. 1408, 2013.

[123] X. Wang, L. Jiao, K. Sheng, C. Li, L. Dai, and G. Shi, "Solution-processable graphene nanomeshes with controlled pore structures.," *Sci. Rep.*, vol. 3, p. 1996, 2013.

[124] X. Zhao, C. M. Hayner, M. C. Kung, and H. H. Kung, "Flexible holey graphene paper electrodes with enhanced rate capability for energy storage applications," *ACS Nano*, vol. 5, no. 11, pp. 8739–8749, 2011.

[125] Z. Fan, Q. Zhao, T. Li, J. Yan, Y. Ren, J. Feng, and T. Wei, "Easy synthesis of porous graphene nanosheets and their use in supercapacitors," *Carbon N. Y.*, vol. 50, no. 4, pp. 1699–1703, 2012.

[126] Y. Lin, K. a Watson, J.-W. Kim, D. W. Baggett, D. C. Working, and J. W. Connell, "Bulk preparation of holey graphene via controlled catalytic oxidation," *Nanoscale*, vol. 5, no. 17, p. 7814, 2013.

[127] Q. Xi, X. Chen, D. G. Evans, and W. Yang, "Gold nanoparticle-embedded porous

graphene thin films fabricated via layer-by-layer self-assembly and subsequent thermal annealing for electrochemical sensing," *Langmuir*, vol. 28, no. 25, pp. 9885–9892, 2012.

[128] J. Yi, D. H. Lee, W. W. Lee, and W. Il Park, "Direct synthesis of graphene meshes and semipermanent electrical doping," *J. Phys. Chem. Lett.*, vol. 4, no. 13, pp. 2099–2104, 2013.

[129] M. J. Mcallister, J. Li, D. H. Adamson, H. C. Schniepp, A. a Abdala, J. Liu, O. M. Herrera-alonso, D. L. Milius, R. Car, R. K. Prud, and I. a Aksay, "Expansion of Graphite," *Society*, vol. 19, no. 4, pp. 4396–4404, 2007.

[130] Y. Xu, K. Sheng, C. Li, and G. Shi, "Self-assembled graphene hydrogel via a one-step hydrothermal process," *ACS Nano*, vol. 4, no. 7, pp. 4324–4330, 2010.

[131] Z. Han, Z. Tang, P. Li, G. Yang, Q. Zheng, and J. Yang, "Ammonia solution strengthened three-dimensional macro-porous graphene aerogel.," *Nanoscale*, vol. 5, no. 12, pp. 5462–7, 2013.

[132] L. Jiang and Z. Fan, "Design of advanced porous graphene materials: from graphene nanomesh to 3D architectures.," *Nanoscale*, vol. 6, no. 4, pp. 1922–45, 2014.

[133] Y. Si and E. Samulski, "Synthesis of water soluble graphene," *Nano Lett.*, vol. 8, no. 6, pp. 1679–1682, 2008.

[134] K. Ishikawa, P. Ducheyne, and S. Radin, "Determination of the Ca/P ratio in calcium-deficient hydroxyapatite using X-ray diffraction analysis," *J. Mater. Sci.*

Mater. Med., vol. 4, pp. 165–168, 1993.

[135] J. S. Earl, D. J. Wood, and S. J. Milne, “Hydrothermal synthesis of hydroxyapatite,” *J. Phys. Conf. Ser.*, vol. 26, pp. 268–271, Feb. 2006.

[136] J. Zhou, X. Zhang, and J. Chen, “High temperature characteristics of synthetic hydroxyapatite,” *J. Mater. Sci. Mater. Med.*, vol. 4, pp. 83–85, 1993.

[137] T. I. Ivanova, O. V. Frank-Kamenetskaya, a. B. Kol’tsov, and V. L. Ugolkov, “Crystal Structure of Calcium-Deficient Carbonated Hydroxyapatite. Thermal Decomposition,” *J. Solid State Chem.*, vol. 160, no. 2, pp. 340–349, Sep. 2001.

[138] T. Leventouri, “Synthetic and biological hydroxyapatites: crystal structure questions.,” *Biomaterials*, vol. 27, no. 18, pp. 3339–42, Jun. 2006.

[139] I. Mobasherpour, M. S. Heshajin, a. Kazemzadeh, and M. Zakeri, “Synthesis of nanocrystalline hydroxyapatite by using precipitation method,” *J. Alloys Compd.*, vol. 430, no. 1–2, pp. 330–333, Mar. 2007.

[140] I. Zhitomirsky and L. Gal-Or, “Electrophoretic deposition of hydroxyapatite,” *J. Mater. Sci. Mater. Med.*, vol. 8, pp. 213–219, 1997.

[141] a J. Ruys, M. Wei, C. C. Sorrell, M. R. Dickson, a Brandwood, and B. K. Milthorpe, “Sintering effects on the strength of hydroxyapatite.,” *Biomaterials*, vol. 16, no. 5, pp. 409–15, Mar. 1995.

[142] a. J. Ruys, a. Brandwood, B. K. Milthorpe, M. R. Dickson, K. a. Zeigler, and C. C. Sorrell, “The effects of sintering atmosphere on the chemical compatibility of

hydroxyapatite and particulate additives at 1200�C," *J. Mater. Sci. Mater. Med.*, vol. 6, no. 5, pp. 297–301, 1995.

[143] A. Bonanni, A. Ambrosi, and M. Pumera, "Nucleic acid functionalized graphene for biosensing.," *Chemistry*, vol. 18, no. 6, pp. 1668–73, Feb. 2012.

[144] H. Dong, Z. Zhao, H. Wen, Y. Y. E. C. Li, F. Guo, A. Shen, F. Pilger, C. Lin, and D. Shi, "Poly(ethylene glycol) conjugated nano-graphene oxide for photodynamic therapy," *Sci. China Chem.*, vol. 53, no. 11, pp. 2265–2271, Nov. 2010.

[145] H. Kim, R. Namgung, K. Singha, I.-K. Oh, and W. J. Kim, "Graphene oxide-polyethylenimine nanoconstruct as a gene delivery vector and bioimaging tool.," *Bioconjug. Chem.*, vol. 22, no. 12, pp. 2558–67, Dec. 2011.

[146] F. Liu, J. Y. Choi, and T. S. Seo, "Graphene oxide arrays for detecting specific DNA hybridization by fluorescence resonance energy transfer.," *Biosens. Bioelectron.*, vol. 25, no. 10, pp. 2361–5, Jun. 2010.

[147] S. Roy, N. Soin, R. Bajpai, D. S. Misra, J. a. McLaughlin, and S. S. Roy, "Graphene oxide for electrochemical sensing applications," *J. Mater. Chem.*, vol. 21, no. 38, p. 14725, 2011.

[148] X. Sun, Z. Liu, K. Welsher, J. T. Robinson, A. Goodwin, S. Zaric, and H. Dai, "Nano-Graphene Oxide for Cellular Imaging and Drug Delivery.," *Nano Res.*, vol. 1, no. 3, pp. 203–212, Jan. 2008.

[149] L. Zhang, J. Xia, Q. Zhao, L. Liu, and Z. Zhang, "Functional graphene oxide as a nanocarrier for controlled loading and targeted delivery of mixed anticancer

drugs.," *Small*, vol. 6, no. 4, pp. 537–44, Feb. 2010.

[150] W. Zhang, Z. Guo, D. Huang, Z. Liu, X. Guo, and H. Zhong, "Synergistic effect of chemo-photothermal therapy using PEGylated graphene oxide.," *Biomaterials*, vol. 32, no. 33, pp. 8555–61, Nov. 2011.

[151] K. Jiang, L. S. Schadler, R. W. Siegel, X. Zhang, H. Zhang, and M. Terrones, "Protein immobilization on carbon nanotubes via a two-step process of diimide-activated amidation," *J. Mater. Chem.*, vol. 14, no. 1, p. 37, 2004.

[152] a Butscher, M. Bohner, S. Hofmann, L. Gauckler, and R. Müller, "Structural and material approaches to bone tissue engineering in powder-based three-dimensional printing.," *Acta Biomater.*, vol. 7, no. 3, pp. 907–20, Mar. 2011.

[153] L. Kvetková, A. Duszová, P. Hvizdoš, J. Dusza, P. Kun, and C. Balázsi, "Fracture toughness and toughening mechanisms in graphene platelet reinforced Si3N4 composites," *Scr. Mater.*, vol. 66, no. 10, pp. 793–796, May 2012.

[154] Y. Wang, Z. Shi, Y. Huang, Y. Ma, C. Wang, M. Chen, and Y. Chen, "Supercapacitor Devices Based on Graphene Materials," *J. Phys. Chem. C*, vol. 113, no. 30, pp. 13103–13107, Jul. 2009.

[155] S. De Liberato, C. Ciuti, D. Auston, M. Nuss, S. Keiding, M. Van Exter, C. Fattinger, A. J. Taylor, C. Highstrete, M. Lee, R. D. Averitt, E. Smirnova, A. Azad, H. Chen, G. Scalari, M. I. Amanti, M. Beck, and J. Faist, "Laser Scribing of High-Performance and Flexible Graphene-Based Electrochemical Capacitors," *Science*, vol. 335, no. March, pp. 1326–1330, 2012.

[156] T. Rath and P. P. Kundu, "Reduced graphene oxide paper based nanocomposite materials for flexible supercapacitors," *RSC Adv.*, vol. 5, no. 34, pp. 26666–26674, 2015.

[157] D. C. Marcano, D. V. Kosynkin, J. M. Berlin, A. Sinitskii, Z. Sun, A. Slesarev, L. B. Alemany, W. Lu, and J. M. Tour, "Improved synthesis of graphene oxide," *ACS Nano*, vol. 4, no. 8, pp. 4806–4814, 2010.

[158] T. Bourgeteau, S. Le Vot, M. Bertucchi, V. Derycke, B. Jousselme, S. Campidelli, and R. Cornut, "New Insights into the Electronic Transport of Reduced Graphene Oxide Using Scanning Electrochemical Microscopy," *J. Phys. Chem. Lett.*, vol. 5, no. 23, pp. 4162–4166, 2014.

[159] H. Akbi, L. Yu, B. Wang, Q. Liu, J. Wang, J. Liu, D. Song, Y. Sun, and L. Liu, "Effect of reducing system on capacitive behavior of reduced graphene oxide film: Application for supercapacitor," *J. Solid State Chem.*, vol. 221, no. 2015, pp. 338–344, 2015.

[160] C. K. Chua and M. Pumera, "Chemical reduction of graphene oxide: a synthetic chemistry viewpoint.," *Chem. Soc. Rev.*, vol. 43, no. 1, pp. 291–312, 2014.

[161] I. K. Moon, J. Lee, R. S. Ruoff, and H. Lee, "Reduced graphene oxide by chemical graphitization," *Nat. Commun.*, vol. 1, no. 6, p. 73, 2010.

[162] S. Pei, J. Zhao, J. Du, W. Ren, and H. M. Cheng, "Direct reduction of graphene oxide films into highly conductive and flexible graphene films by hydrohalic acids," *Carbon N. Y.*, vol. 48, no. 15, pp. 4466–4474, 2010.

[163] Y. Zhu, M. D. Stoller, W. Cai, A. Velamakanni, R. D. Piner, D. Chen, and R. S. Ruoff, “Exfoliation of graphite oxide in propylene carbonate and thermal reduction of the resulting graphene oxide platelets,” *ACS Nano*, vol. 4, no. 2, pp. 1227–1233, 2010.

[164] X. Li, G. Zhang, X. Bai, X. Sun, X. Wang, E. Wang, and H. Dai, “Highly conducting graphene sheets and Langmuir-Blodgett films.,” *Nat. Nanotechnol.*, vol. 3, no. 9, pp. 538–42, Sep. 2008.

[165] M. Vlasea, R. Pilliar, and E. Toyserkani, “Control of structural and mechanical properties in bioceramic bone substitutes via additive manufacturing layer stacking orientation,” *Addit. Manuf.*, vol. 6, pp. 30–38, 2015.

[166] A. Azhari, E. Toyserkani, and C. Villain, “Additive manufacturing of graphene-hydroxyapatite nanocomposite structures,” *Int. J. Appl. Ceram. Technol.*, vol. 12, no. 1, pp. 8–17, 2015.

[167] A. Basalah, S. Esmaeili, and E. Toyserkani, “A novel additive manufacturing-based technique for developing bio-structures with conformal channels and encapsulated voids,” *Biomed. Phys. Eng. Express*, vol. 1, no. 4, p. 45007, 2015.

[168] “The reduction of graphene oxide.” [Online]. Available: http://ac.els-cdn.com/S0008622311008967/1-s2.0-S0008622311008967-main.pdf?_tid=c048cca8-39d0-11e4-99a8-00000aacb360&acdnat=1410453127_fcd035e5e4ee88c3282df8bcec87d405. [Accessed: 11-Sep-2014].

[169] H. J. Salavagione, M. A. G??mez, and G. Mart??nez, “Polymeric modification of graphene through esterification of graphite oxide and poly(vinyl alcohol),” *Macromolecules*, vol. 42, no. 17, pp. 6331–6334, 2009.

[170] M. a. Pope, S. Korkut, C. Punckt, and I. a. Aksay, “Supercapacitor Electrodes Produced through Evaporative Consolidation of Graphene Oxide-Water-Ionic Liquid Gels,” *J. Electrochem. Soc.*, vol. 160, no. 10, pp. A1653–A1660, 2013.

[171] S. Park, J. An, I. Jung, R. D. Piner, S. J. An, X. Li, A. Velamakanni, and R. S. Ruoff, “Colloidal suspensions of highly reduced graphene oxide in a wide variety of organic solvents,” *Nano Lett.*, vol. 9, no. 4, pp. 1593–1597, 2009.

[172] S. Das, F. Irin, H. S. Tanvir Ahmed, A. B. Cortinas, A. S. Wajid, D. Parviz, A. F. Jankowski, M. Kato, and M. J. Green, “Non-covalent functionalization of pristine few-layer graphene using triphenylene derivatives for conductive poly (vinyl alcohol) composites,” *Polymer (Guildf).*, vol. 53, no. 12, pp. 2485–2494, 2012.

[173] Z. Niu, J. Chen, H. H. Hng, J. Ma, and X. Chen, “A leavening strategy to prepare reduced graphene oxide foams,” *Adv. Mater.*, vol. 24, no. 30, pp. 4144–4150, 2012.

[174] M. D. Stoller and R. S. Ruoff, “Best practice methods for determining an electrode material’s performance for ultracapacitors,” *Energy Environ. Sci.*, vol. 3, no. 9, p. 1294, 2010.

[175] L. Hu, J. W. Choi, Y. Yang, S. Jeong, F. La Mantia, L.-F. Cui, and Y. Cui, “Highly conductive paper for energy-storage devices.,” *Proc. Natl. Acad. Sci. U. S.*

A., vol. 106, no. 51, pp. 21490–21494, 2009.

[176] S. Pei and H. M. Cheng, “The reduction of graphene oxide,” *Carbon N. Y.*, vol. 50, no. 9, pp. 3210–3228, 2012.

[177] M. A. Pope, C. Punckt, and I. A. Aksay, “Intrinsic capacitance and redox activity of functionalized graphene sheets,” *J. Phys. Chem. C*, vol. 115, no. 41, pp. 20326–20334, 2011.

[178] D. R. Dreyer, S. Park, C. W. Bielawski, and R. S. Ruoff, “The chemistry of graphene oxide.,” *Chem. Soc. Rev.*, vol. 39, no. 1, pp. 228–40, Jan. 2009.

[179] M. F. El-Kady and R. B. Kaner, “Scalable fabrication of high-power graphene micro-supercapacitors for flexible and on-chip energy storage,” *Nat. Commun.*, vol. 4, p. 1475, 2013.

[180] Y. Xu, Z. Lin, X. Huang, Y. Liu, Y. Huang, and X. Duan, “Flexible Solid-State Supercapacitors Based on Three-Dimensional Graphene Hydrogel Films,” *ACS Nano*, vol. 7, no. 5, pp. 4042–4049, 2013.

[181] M. Vaezi, H. Seitz, and S. Yang, “A review on 3D micro-additive manufacturing technologies,” *Int. J. Adv. Manuf. Technol.*, vol. 67, no. 5–8, pp. 1721–1754, 2013.

[182] K. V. Wong and A. Hernandez, “A Review of Additive Manufacturing,” *ISRN Mech. Eng.*, vol. 2012, pp. 1–10, 2012.

[183] B. Berman, “3-D printing: The new industrial revolution,” *Bus. Horiz.*, vol. 55, no. 2, pp. 155–162, 2012.

[184] A. C. de Leon, Q. Chen, N. B. Palaganas, J. O. Palaganas, J. Manapat, and R. C. Advincula, “High performance polymer nanocomposites for additive manufacturing applications,” *React. Funct. Polym.*, vol. 103, pp. 141–155, 2016.

[185] J. H. Kim, W. S. Chang, D. Kim, J. R. Yang, J. T. Han, G. W. Lee, J. T. Kim, and S. K. Seol, “3D printing of reduced graphene oxide nanowires,” *Adv. Mater.*, vol. 27, no. 1, pp. 157–161, 2015.

[186] K. Arapov, R. Abbel, G. de With, and H. Friedrich, “Inkjet printing of graphene,” *Faraday Discuss.*, vol. 173, pp. 323–336, 2014.

[187] E. García-Tuñon, S. Barg, J. Franco, R. Bell, S. Eslava, E. D’Elia, R. C. Maher, F. Guitian, and E. Saiz, “Printing in Three Dimensions with Graphene,” *Adv. Mater.*, pp. 1–6, 2015.

[188] X. Han, Y. Chen, H. Zhu, C. Preston, J. Wan, Z. Fang, and L. Hu, “Scalable, printable, surfactant-free graphene ink directly from graphite.,” *Nanotechnology*, vol. 24, no. 20, p. 205304, 2013.

[189] D. Kong, L. T. Le, Y. Li, J. L. Zunino, and W. Lee, “Temperature-dependent electrical properties of graphene inkjet-printed on flexible materials,” *Langmuir*, vol. 28, no. 37, pp. 13467–13472, 2012.

[190] L. T. Le, M. H. Ervin, H. Qiu, B. E. Fuchs, and W. Y. Lee, “Graphene supercapacitor electrodes fabricated by inkjet printing and thermal reduction of graphene oxide,” *Electrochem. commun.*, vol. 13, no. 4, pp. 355–358, 2011.

[191] J. Li, F. Ye, S. Vaziri, M. Muhammed, M. C. Lemme, and M. Östling, “Efficient

Inkjet Printing of Graphene," *Adv. Mater.*, vol. 25, no. 29, pp. 3985–3992, 2013.

[192] T. Nathan-Walleser, I. M. Lazar, M. Fabritius, F. J. T??lle, Q. Xia, B. Bruchmann, S. S. Venkataraman, M. G. Schwab, and R. M??lhaupt, "3D micro-extrusion of graphene-based active electrodes: Towards high-rate AC line filtering performance electrochemical capacitors," *Adv. Funct. Mater.*, vol. 24, no. 29, pp. 4706–4716, 2014.

[193] E. B. Secor, P. L. Prabhumirashi, K. Puntambekar, M. L. Geier, and M. C. Hersam, "Inkjet printing of high conductivity, flexible graphene patterns," *J. Phys. Chem. Lett.*, vol. 4, no. 8, pp. 1347–1351, 2013.

[194] K. Sun, T. S. Wei, B. Y. Ahn, J. Y. Seo, S. J. Dillon, and J. A. Lewis, "3D printing of interdigitated Li-ion microbattery architectures," *Adv. Mater.*, vol. 25, no. 33, pp. 4539–4543, 2013.

[195] X. Wei, D. Li, W. Jiang, Z. Gu, X. Wang, Z. Zhang, and Z. Sun, "3D Printable Graphene Composite.," *Sci. Rep.*, vol. 5, pp. 1–7, 2015.

[196] C. Zhao, C. Wang, R. Gorkin, S. Beirne, K. Shu, and G. G. Wallace, "Three dimensional (3D) printed electrodes for interdigitated supercapacitors," *Electrochem. commun.*, vol. 41, no. 2014, pp. 20–23, 2014.

[197] K. Chen, L. Chen, Y. Chen, H. Bai, and L. Li, "Three-dimensional porous graphene-based composite materials: electrochemical synthesis and application," *J. Mater. Chem.*, vol. 22, no. 39, p. 20968, 2012.

[198] Q. Wu, Y. Xu, Z. Yao, A. Liu, and G. Shi, "Supercapacitors based on flexible

graphene/polyaniline nanofiber composite films," *ACS Nano*, vol. 4, no. 4, pp. 1963–70, Apr. 2010.

[199] O. Akhavan, "The effect of heat treatment on formation of graphene thin films from graphene oxide nanosheets," *Carbon N. Y.*, vol. 48, no. 2, pp. 509–519, 2010.

[200] C. Xu and X. Wang, "Fabrication of flexible metal-nanoparticle films using graphene oxide sheets as substrates.," *Small*, vol. 5, no. 19, pp. 2212–7, Oct. 2009.

[201] Z.-S. Wu, K. Parvez, X. Feng, and K. Müllen, "Graphene-based in-plane micro-supercapacitors with high power and energy densities.," *Nat. Commun.*, vol. 4, p. 2487, 2013.

[202] L. L. Zhang, X. Zhao, M. D. Stoller, Y. Zhu, H. Ji, S. Murali, Y. Wu, S. Perales, B. Clevenger, and R. S. Ruoff, "Highly conductive and porous activated reduced graphene oxide films for high-power supercapacitors," *Nano Lett.*, vol. 12, no. 4, pp. 1806–1812, 2012.

[203] A. Yu, H. W. Park, A. Davies, D. C. Higgins, Z. Chen, and X. Xiao, "Free-Standing Layer-By-Layer Hybrid Thin Film of Graphene-MnO 2 Nanotube as Anode for Lithium Ion Batteries," pp. 1855–1860, 2011.

[204] A. Nekahi, P. H. Marashi, and D. Haghshenas, "Transparent conductive thin film of ultra large reduced graphene oxide monolayers," *Appl. Surf. Sci.*, vol. 295, no. 2014, pp. 59–65, 2014.

[205] F. Torrisi, T. Hasan, W. Wu, Z. Sun, A. Lombardo, T. S. Kulmala, G. W. Hsieh, S. Jung, F. Bonaccorso, P. J. Paul, D. Chu, and A. C. Ferrari, "Inkjet-printed

graphene electronics," *ACS Nano*, vol. 6, no. 4, pp. 2992–3006, 2012.

[206] M. Singh, H. M. Haverinen, P. Dhagat, and G. E. Jabbour, "Inkjet Printing-Process and Its Applications," *Adv. Mater.*, vol. 22, no. 6, pp. 673–685, 2010.

[207] G. W. Scherer, "Theory of Drying," *J. Am. Ceram. Soc.*, vol. 73, no. 1, pp. 3–14, 1990.

[208] B. E. Conway, *Electrochemical Supercapacitors*. .

[209] F. Bonaccorso, L. Colombo, G. Yu, M. Stoller, V. Tozzini, a C. Ferrari, R. S. Ruoff, and V. Pellegrini, "2D materials. Graphene, related two-dimensional crystals, and hybrid systems for energy conversion and storage," *Science (80-.).*, vol. 347, no. 6217, p. 1246501, 2015.

[210] Y. Zhu, S. Murali, M. D. Stoller, K. J. Ganesh, W. Cai, P. J. Ferreira, A. Pirkle, R. M. Wallace, K. a Cychosz, M. Thommes, D. Su, E. a Stach, and R. S. Ruoff, "Carbon-based supercapacitors produced by activation of graphene.," *Science*, vol. 332, no. 6037, pp. 1537–41, Jun. 2011.

[211] TaeYoung Kim, Gyujin Jung, Seonmi Yoo, Kwang S. Suh, and Rodney S. Ruoff, "Activated Graphene-Based Carbons as Supercapacitor Electrodes with Macro- and Mesopores," *ACS Nano*, vol. 7, no. 8, pp. 6899–6905, 2013.

[212] Y. Shao, M. F. El-Kady, L. J. Wang, Q. Zhang, Y. Li, H. Wang, M. F. Mousavi, and R. B. Kaner, "Graphene-based materials for flexible supercapacitors," *Chem. Soc. Rev.*, vol. 44, no. 11, pp. 3639–3665, 2015.

[213] B. G. Choi, M. Yang, W. H. Hong, J. W. Choi, and Y. S. Huh, “3D macroporous graphene frameworks for supercapacitors with high energy and power densities,” *ACS Nano*, vol. 6, no. 5, pp. 4020–4028, 2012.

[214] S. Yin, Z. Niu, and X. Chen, “Assembly of graphene sheets into 3D macroscopic structures,” *Small*, vol. 8, no. 16, pp. 2458–2463, 2012.

[215] W. Chen and L. Yan, “In situ self-assembly of mild chemical reduction graphene for three-dimensional architectures.,” *Nanoscale*, vol. 3, pp. 3132–3137, 2011.

[216] L. Zhang and G. Shi, “Preparation of highly conductive graphene hydrogels for fabricating supercapacitors with high rate capability,” *J. Phys. Chem. C*, vol. 115, no. 34, pp. 17206–17212, 2011.

[217] Y. Tao, X. Xie, W. Lv, D.-M. Tang, D. Kong, Z. Huang, H. Nishihara, T. Ishii, B. Li, D. Golberg, F. Kang, T. Kyotani, and Q.-H. Yang, “Towards ultrahigh volumetric capacitance: graphene derived highly dense but porous carbons for supercapacitors.,” *Sci. Rep.*, vol. 3, p. 2975, 2013.

[218] X. Jiang, Y. Ma, J. Li, Q. Fan, and W. Huang, “Self-Assembly of Reduced Graphene Oxide into Three-Dimensional Architecture by Divalent Ion Linkage,” *J. Phys. Chem. C*, vol. 114, no. 51, pp. 22462–22465, Dec. 2010.

[219] W. Yang, Y. Xiong, L. Zou, Z. Zou, D. Li, Q. Mi, Y. Wang, and H. Yang, “Plasmonic Pd Nanoparticle- and Plasmonic Pd Nanorod-Decorated BiVO4 Electrodes with Enhanced Photoelectrochemical Water Splitting Efficiency Across Visible-NIR Region,” *Nanoscale Res. Lett.*, vol. 11, no. 1, p. 283, 2016.

[220] C. Langhammer, Z. Yuan, I. Zorić, and B. Kasemo, “Plasmonic properties of supported Pt and Pd nanostructures,” *Nano Lett.*, vol. 6, no. 4, pp. 833–838, 2006.

[221] J. Yan, J. Liu, Z. Fan, T. Wei, and L. Zhang, “High-performance supercapacitor electrodes based on highly corrugated graphene sheets,” *Carbon N. Y.*, vol. 50, no. 6, pp. 2179–2188, May 2012.

[222] H. C. Schniepp, J.-L. Li, M. J. McAllister, H. Sai, M. Herrera-Alonso, D. H. Adamson, R. K. Prud’homme, R. Car, D. a Saville, and I. a Aksay, “Functionalized single graphene sheets derived from splitting graphite oxide.,” *J. Phys. Chem. B*, vol. 110, no. 17, pp. 8535–9, May 2006.

[223] C. Tan, X. Huang, and H. Zhang, “Synthesis and applications of graphene-based noble metal nanostructures,” *Mater. Today*, vol. 16, no. 1–2, pp. 29–36, 2013.

[224] T. T. Baby, S. S. J. Aravind, T. Arockiadoss, R. B. Rakhi, and S. Ramaprabhu, “Metal decorated graphene nanosheets as immobilization matrix for amperometric glucose biosensor,” *Sensors Actuators, B Chem.*, vol. 145, no. 1, pp. 71–77, 2010.

[225] Z. Jin, D. Nackashi, W. Lu, C. Kittrell, and J. M. Tour, “Decoration, migration, and aggregation of palladium nanoparticles on graphene sheets,” *Chem. Mater.*, vol. 22, no. 20, pp. 5695–5699, 2010.

[226] K. S. Subrahmanyam, A. K. Manna, S. K. Pati, and C. N. R. Rao, “A study of graphene decorated with metal nanoparticles,” *Chem. Phys. Lett.*, vol. 497, no. 1–3, pp. 70–75, 2010.

[227] W. Li, Y. He, L. Wang, G. Ding, Z. Q. Zhang, R. W. Lortz, P. Sheng, and N.

Wang, “Electron localization in metal-decorated graphene,” *Phys. Rev. B - Condens. Matter Mater. Phys.*, vol. 84, no. 4, pp. 1–8, 2011.

[228] M. Deraman, I. A. Talib, R. Farma, R. Omar, M. M. Ishak, E. Taer, B. N. M. Dolah, N. H. Basri, N. S. M. Nor, M. Deraman, I. A. Talib, R. Omar, J. G. Manjunatha, and M. M. Ishak, “Physical and electrochemical properties of supercapacitor composite electrodes prepared from biomass carbon and carbon from green petroleum coke,” *5Th Asian Phys. Symp. (Aps 2012)*, vol. 8, no. 1, pp. 257–273, 2013.

[229] D. K. Kampouris, X. Ji, E. P. Randviir, and C. E. Banks, “A new approach for the improved interpretation of capacitance measurements for materials utilised in energy storage,” *RSC Adv.*, vol. 5, no. 17, pp. 12782–12791, Jan. 2015.

[230] P. Chen, J. J. Yang, S. S. Li, Z. Wang, T. Y. Xiao, Y. H. Qian, and S. H. Yu, “Hydrothermal synthesis of macroscopic nitrogen-doped graphene hydrogels for ultrafast supercapacitor,” *Nano Energy*, vol. 2, no. 2, pp. 249–256, 2013.

[231] “ASTM Designation No. E104-02 Standard Practice for Maintaining Constant Relative Humidity by Means of Aqueous Solutions,” vol. 2, no. Reapproved 2012, pp. 1–5, 2012.

[232] D. Zhang, J. Tong, and B. Xia, “Humidity-sensing properties of chemically reduced graphene oxide/polymer nanocomposite film sensor based on layer-by-layer nano self-assembly,” *Sensors Actuators, B Chem.*, vol. 197, no. 2014, pp. 66–72, 2014.

[233] “ENHANCED PERFORMANCE OF A CMOS INTERDIGITAL CAPACITIVE HUMIDITY SENSOR BY GRAPHENE OXIDE Key Laboratory of MEMS of the Ministry of Education , Southeast University , Nanjing 210096 , China,” *Response*, pp. 1954–1957, 2011.

[234] Y. Yao, X. Chen, H. Guo, Z. Wu, and X. Li, “Humidity sensing behaviors of graphene oxide-silicon bi-layer flexible structure,” *Sensors Actuators, B Chem.*, vol. 161, no. 1, pp. 1053–1058, 2012.

[235] Q. Huang, D. Zeng, S. Tian, and C. Xie, “Synthesis of defect graphene and its application for room temperature humidity sensing,” *Mater. Lett.*, vol. 83, no. 2012, pp. 76–79, 2012.

[236] S. M. Balashov, O. V. Balachova, A. P. Filho, M. C. Q. Bazetto, and M. G. de Almeida, “Surface Acoustic Wave Humidity Sensors Based on Graphene Oxide Thin Films Deposited with the Surface Acoustic Wave Atomizer,” *ECS Trans.*, vol. 49, no. 1, pp. 445–450, 2012.

[237] Y. Yao, X. Chen, H. Guo, and Z. Wu, “Graphene oxide thin film coated quartz crystal microbalance for humidity detection,” *Appl. Surf. Sci.*, vol. 257, no. 17, pp. 7778–7782, 2011.

[238] L. Guo, H. B. Jiang, R. Q. Shao, Y. L. Zhang, S. Y. Xie, J. N. Wang, X. Bin Li, F. Jiang, Q. D. Chen, T. Zhang, and H. B. Sun, “Two-beam-laser interference mediated reduction, patterning and nanostructuring of graphene oxide for the production of a flexible humidity sensing device,” *Carbon N. Y.*, vol. 50, no. 4, pp.

1667–1673, 2012.

[239] H. Bi, K. Yin, X. Xie, J. Ji, S. Wan, L. Sun, M. Terrones, and M. S. Dresselhaus, "Ultrahigh humidity sensitivity of graphene oxide.," *Sci. Rep.*, vol. 3, no. 5 V, p. 2714, 2013.